Aerodynamic Interaction in a Three-Rotor "Tandem" Configuration

Jaime Joaquín González Pérez

Thesis to obtain the Master of Science Degree in

Aerospace Engineering

Supervisors: Prof. Filipe Szolnoky Ramos Pinto Cunha
Prof. José Raul Carreira Azinheira

Examination Committee

Chairperson: Prof. Fernando José Parracho Lau
Supervisor: Prof. Filipe Szolnoky Ramos Pinto Cunha
Member of the Committee: Prof. José Maria Campos da Silva André

October 2022

Dedicado a Camille, por un tiempo precioso y por hacer de Lisboa un lugar mejor

Declaration

I declare that this document is an original work of my own authorship and that it fulfills all the requirements of the Code of Conduct and Good Practices of the Universidade de Lisboa.

Acknowledgments

I must thank my supervisors Filipe Cunha and José Raul Azinheira for granting me the opportunity to work on this thesis and for their advice, concern and help throughout it. I must also thank professors José Manuel Pereira and Pedro Martí for their advice in the computational fluid dynamics field, my laboratory mate Carlos Vasconcelos for his cooperation during these months and Henrique Santos for his help in the test bench matters. I do not forget about my family and friends, specially my mother, Jaime, Schahde, Josep and Teresa, whose support made this easier. Thank you all.

Resumo

O objetivo desta tese é avaliar o impacto de vários parâmetros (diâmetro do rotor, separações interplanar e interaxial e velocidade de rotação) no desempenho de configurações parcialmente sobrepostas no rotor tandem. Pretende-se contribuir para o desenvolvimento de configurações alternativas de drones com os resultados alcançados, em particular para as configurações tandem presentes em drones com dois planos rotores. Um esboço da Teoria do Momento Linear é apresentado como uma análise de primeira aproximação de rotores isolados, juntamente com uma adaptação existente da teoria para configurações de rotores tandem representando a interação do rotor. Propõe-se uma modificação deste modelo para que também tenha em consideração a separação interplanar à parte da distância interaxial. Um banco de ensaio originalmente desenvolvido para o estudo de configurações coaxiais para dois pequenos rotores foi adaptado para o estudo de configurações tandem até três rotores. Os instrumentos são capazes de medir o impulso e torque produzidos por eles, e a calibração do setup foi verificada com dados de desempenho fornecidos pelo fabricante e com dados de simulações CFD. Várias simulações CFD foram realizadas com modelos CAD que se assemelham muito às hélices originais. A interação do rotor foi capturada com sucesso em relação à perda de impulso. O desempenho do rotor a jusante mostrou ser muito sensível à separação interaxial e à velocidade angular do rotor a montante, enquanto a variação do diâmetro do rotor a montante teve um impacto intermediário e o efeito da separação interplanar foi leve.

Palavras-chave: Drone, Configuraçoes Tandem, Análise Experimental, CFD, Sistema de Propulsão Aérea, Interação Aerodinâmica

Abstract

The aim of this thesis is to evaluate the impact of several parameters (rotor diameter, interaxial and interplanar separations and rotation speed) on the performance of partially overlapping tandem rotor configurations. It is pretended to contribute to the development of alternative drone configurations with the attained results, in particular to tandem configurations present in drones with two rotor planes. An outline of Momentum Theory is presented as a first-approximation analysis of isolated rotors, along with an existing adaptation of the theory for tandem-rotor configurations accounting for the rotor interaction. A modification of this model is proposed so that it also takes in regard the interplanar separation other than the interaxial distance. A testing bench originally developed for the study of coaxial configurations for two small rotors has been adapted for the study of tandem configurations of up to three rotors. The instruments are capable of measuring the thrust and torque produced by them, and the calibration of the setup was verified with performance data provided by the manufacturer and with CFD simulations data. Several CFD simulations were carried out with CAD models which highly resemble the original propellers. The rotor interaction was successfully captured in regard to thrust loss. The downstream rotor performance was found to be very sensitive to the interaxial separation and to the upstream rotor angular velocity, while the upstream rotor diameter variation had an intermediate impact and the effect of the interplanar separation was slight.

Contents

List of Tables

List of Figures

Nomenclature

Greek symbols

δ Overlap distance ratio

Δ_t Time step

Δ_x Spatial discretization length

ε Error during the calibration procedure)

θ Circle intersection angle for equal areas

κ Induced power correction factor

κ_{ov} Overlap coefficient of two rotors in tandem

ρ Air density

σ Rotor solidity

φ Second circle intersection angle for unequal areas

χ Upstream wake velocity weight factor

Ω Angular velocity

Roman symbols

A Rotor area

A_{ov} Overlap area

C Courant number

c Propeller blade chord

C_{d_0} Zero-lift drag coefficient

C_D Drag Coefficient

C_L Lift Coefficient

C_M Moment Coefficient

C_{P_0} Coefficient of profile power

$C_{P_{\mathrm{ind}}}$ Coefficient of induced power

C_P Power Coefficient

$\mathbf{C}^1_{\mathrm{neg}}$ Calibration matrix of IT1 for the negative torque direction

$\mathbf{C}^2_{\mathrm{neg}}$ Calibration matrix of IT2 for the negative torque direction

$\mathbf{C}^1_{\mathrm{pos}}$ Calibration matrix of IT1 for the positive torque direction

$\mathbf{C}^2_{\mathrm{pos}}$ Calibration matrix of IT2 for the positive torque direction

D Rotor diameter

d Interaxial distance

$\mathbf{D}$ Sensitivity coefficients matrix (calibration)

DL Disk Loading

$\vec{F}$ Total force exerted on the fluid in a control volume

FM Figure of Merit

F_x Axial force produced by the a rotor (thrust)

F_y Lateral force produced by a rotor

h Interplanar or rotor-plane distance

$\mathbf{I}_{[\mathrm{N}]}$ Identity matrix of dimensions N

K_{v} Electric motor velocity constant $[\mathrm{RPM/V}]$

K_{P1} Proportional gain of the IT1 motor rotation speed control loop

K_{P2} Proportional gain of the IT2 motor rotation speed control loop

$\dot{m}$ Mass flow rate

Ma Mach number

M_x Axial moment produced by a rotor (torque)

N_b Number of rotor blades

P_0 Profile power

P_{d} Mechanical power on the downstream rotor

P_{ind} Induced power

P_{mech} Mechanical power

P_{total} Total mechanical power of the tandem system

P_{u} Mechanical power on the upstream rotor

R Rotor radius

r Bridge outputs

Re Reynolds number

r_w Wake radius

$\vec{S}$ Orthogonal vector to the control volume surface

T Thrust produced by a rotor (MTA)

T_x Torque produced by a rotor

u Velocity in Navier-Stokes equations

u, v, w Velocity Cartesian components

$\vec{V}$ Fluid velocity

v_i Induced velocity at the rotor plane

$\mathbf{V}_{\text{R}}$ Covariance matrix for the bridge outputs

$\mathbf{V}_{\text{neg}}^{1}$ Error computation matrix of IT1 for the negative torque direction

$\mathbf{V}_{\text{neg}}^{2}$ Error computation matrix of IT2 for the positive torque direction

$\mathbf{V}_{\text{pos}}^{1}$ Error computation matrix of IT1 for the positive torque direction

$\mathbf{V}_{\text{pos}}^{2}$ Error computation matrix of IT2 for the negative torque direction

$\mathbf{V}_{\text{w}}$ External errors statistical estimation matrix

W Total fluid energy in the control volume

w Slipstream velocity or fully developed wake velocity

$\mathbf{W}$ Weighting matrix (calibration)

X, Y, Z Cartesian coordinate axes

$\mathbf{Y}$ Matrix of static loads applied on the calibration process

$\hat{y}$ Estimated loads obtained with the calibration matrix

y_0 Set of values used as reference

Subscripts

d Referring to downstream

dw Fully developed wake

i, j, k Computational indexes

ind   Induced

iso   Referring to isolated rotor performance

mech   Mechanical

ov   Related to overlap

u   Referring to upstream

uw   Referring to the upstream rotor wake

w Relative to the wake

x, y, z Cartesian components

∞ Far-wake condition

Superscripts

T   Transpose

Acronyms

BLDC   Brushless direct current (engine)

CAD   Computer aided design

CCW   Counterclockwise

CFD   Computational fluid dynamics

CFL   Courant–Friedrichs–Lewy

CV   Control volume

CW   Clockwise

DAQ   Data acquisition

DNS   Direct numerical simulation

ESC   Electronic speed control

IT   Instrumented tube

LE   Leading edge

LES   Large eddie simulation

MRE   Mean relative error

MTA   Momentum theory analysis

NI   National Instruments

PWM   Pulse width modulation

RANS   Reynolds-averaged Navier-Stokes (equations)

RE   Relative error

RPM   Revolutions per minute

SDR   Specific dissipation rate

SG   Strain gage

SST   Shear stress transport

STEP   Standard for the Exchange of Product Data

TE   Trailing edge

TKE   Turbulent kinetic energy

USB   Universal serial bus

UT   Uninstrumented tube

WLS   Weighted Least-Squares

Chapter 1

Introduction

1.1 Motivation

The use of drones or unmanned aerial vehicles (UAVs) is becoming increasingly popular in a lot of areas of application. Aerial imaging, surveillance, weather forecasting or the delivery of goods are just some of the fields which benefit from the use of drones, due to either profitability, effectiveness or safety over human labor.

Although there are several types of drones (divided in single rotor, multi-rotor, flapping wings, and fixed-wing [1]), multi-rotor UAVs are the ones arousing the most interest due to their capability to hover. Within this category the most extended design is the quadrotor, given that four rotors of variable speed in pairs of opposite rotation directions bear the simplest solution for the attitude control. However, the quadrotor performance is awfully vulnerable to the malfunction of a motor, losing the capability to balance the moments in all of the three axes simultaneously. Since drones are progressively becoming a part of everyday life, the safety issue raises concern specially when civilian areas are involved. Moreover, for applications in which heavier loads are to be transported, the thrust produced by only four rotors is limited if the overall UAV dimensions and the noise emissions are contemplated.

The answer to both of the latter complications is the addition of extra rotors. Hexarotor or octorotor configurations are not only able to provide for more thrust without necessarily increasing the rotor size and arm length or the rotation speed (which affect the overall drone dimensions and its noise emission respectively), but also they can bear with a rotor fail while maintaining the controllability of the system by rearranging the power distribution on the rest of motors. These configurations can be presented in several forms, in some of which the rotors are distributed in two rotor planes (either coaxial or tandem-like configurations). As long as rotors are in proximity there will be an interaction between them that has an impact on their performance, and this area is very understudied in UAVs in comparison to the existing research on their helicopter counterpart.

1.2 Topic Overview

Multi-rotor vehicles present several advantages over traditional helicopter designs, where a single rotor provides all the thrust. Multi-rotors are more efficient in the use of power since all of the rotors are meant to provide lift and they can be controlled by increasing or decreasing the power on them independently, whereas in a traditional helicopter configuration the tail rotor does not produce lift and the mechanisms to drive maneuvers are far more complex and lead to increased maintenance.

Multi-rotors with a large number of rotors increase their reliability and the overall thrust produced by the vehicle, although the number of rotors and their size are limited when they are laid out on a single rotor plane. Alternative configurations with two rotor planes separated by a vertical distance have been explored by some researchers, such as Zhu et al. [2], who carried out a study on the performance of several octorotor configurations with rotors divided in two rotor planes. It is pointed out that when a rotor plane is rotated 45° with respect to the other, the resulting tandem-like configuration (in which there is also a horizontal distance between rotors) yields a better performance than that of pure coaxial rotors, while allowing for grater rotor diameters without having to extend the drone arms to the degree that a single rotor plane configuration would require. These configurations are shown in Figure 1.1:

(a) Single rotor plane, tandem-like and pure coaxial configurations for small propellers

(b) Tandem-like and pure coaxial configurations for big propellers
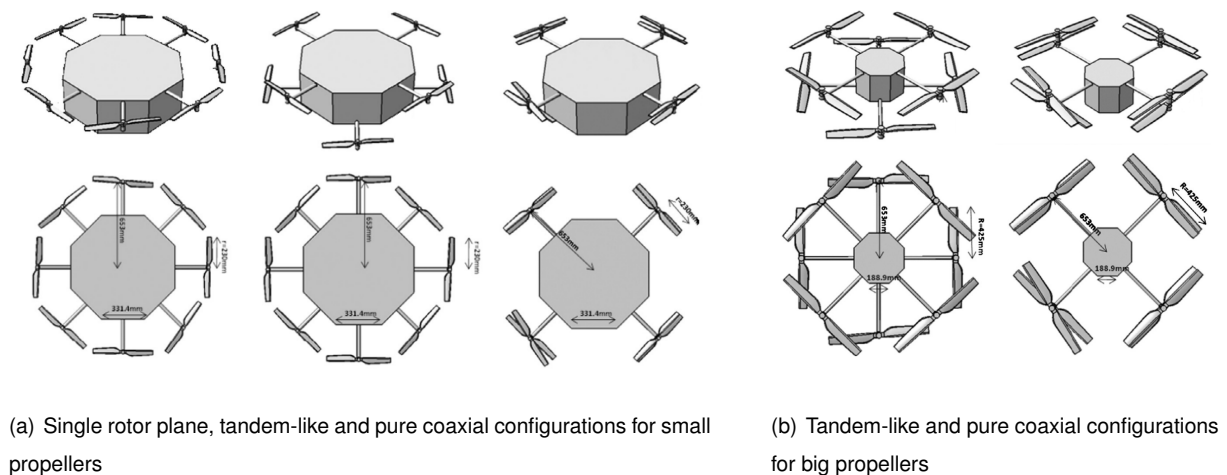
Figure 1.1: Octorotor configurations studied by Zhu et al. [2]

However, tandem configurations have their drawbacks. Although the effect is less remarkable than for coaxial configurations, there will still appear an aerodynamic interaction between the rotors that will specially affect the downstream rotors under a wake, reducing the developed thrust of the overall system and increasing the power needed. It is important to study this phenomenon and find design lines that make the most out of tandem configurations.

1.3 Objectives

The aim of this study is to identify and characterize the parameters that are relevant for the performance of tandem rotor systems. The specific objectives proposed to accomplish that task are:

- Define which parameters are relevant for tandem configuration

- Approach the problem from a theoretical perspective

- Perform modifications on the available test bench to allow for the experimental study of tandem configurations with three rotors

- Create and execute a testing plan to study the variables of interest

- Create accurate CAD models of the propellers to perform a CFD study and find the mesh and simulation related parameters that yield accurate CFD results

- Analyse the experimental and CFD results to assess the effect of the study parameters on the downstream rotor performance

1.4 Thesis Outline

A summary of the Momentum Theory is presented in chapter 2 to serve as a theoretical analysis tool for rotatory wing systems. Two approaches based on Momentum Theory to assess the interaction issue in tandem configurations are also included (for rotors in close proximity and in far wake), along with a modification of the far wake model that allows it to account for interplanar separation besides of interaxial separation.

In chapter 3 the experimental approach and methodology is presented. The parameters of study and the tests to evaluate their impact on the back rotor thrust and torque are stated. The tests are carried out on a bench test originally designed for the study of coaxial configuration [3], which was modified to allow for the study of tandem configuration with two rotors [4] and ultimately was granted a third rotor capability during this work (to resemble more the configurations presented in section 1.2). The calibration procedure for the instruments is presented in detail, along with its verification by comparing the obtained thrust and torque for isolated propellers with the manufacturer data and with CFD simulations.

The study also includes a CFD approach, presented in chapter 4. Accurate CAD models for the propellers used in the experimental tests are designed and the parameters that lead to reliable simulations are established. CFD fundamentals and the followed methodology are introduced.

The experimental and CFD results are presented and analysed in chapter 5. The conclusions, featuring the achievements of this thesis and the future work proposed appear in chapter 6.

Chapter 2

Theoretical Background

There are several theoretical tools and analytical methods in the helicopter and UAV design. A first-order approximation very commonly used is the Momentum Theory Analysis (MTA). In this section it will be presented, as explained by Leishman [5].

2.1 Momentum Theory applied to an Isolated Hovering Rotor

The Momentum Theory has its foundations in the the conservation of fluid mass throughout the control volume (Equation 2.1), the conservation of fluid momentum (Equation 2.2) and the conservation of energy (Equation 2.3), where $\vec{V}$ is the fluid velocity, $\vec{S}$ is the orthogonal vector to the control volume surface, p is the total pressure on the surface, W is the fluid total energy in the control volume and $\vec{F}$ is the force to which the fluid is subjected.

$$\iint_S \rho \vec{V} \cdot d\vec{S} = 0 \tag{2.1}$$

$$\vec{F} = \iint_S p d\vec{S} + \iint_S \vec{V}(\rho \vec{V} \cdot d\vec{S}) \tag{2.2}$$

$$W = \iint_S \frac{1}{2} |\vec{V}|^2 (\rho \vec{V} \cdot d\vec{S}) \tag{2.3}$$

The momentum Theory models the rotor as a rotor-disk: a flat circular area which adds energy to the flow and accelerates it downstream. The flow in momentum theory is assumed to be ideal, one-dimensional, incompressible, inviscid and quasi-steady. Moreover, the fluid is considered to flow only in the wake and to remain still in the rest of the domain, with a well-defined boundary (since no viscosity is regarded). The flow tube starts above the rotor disk, where the velocity increases from 0 to the value at the rotor disk, referred to as induced velocity v_i (induced by the rotor-disk action), as shown in Figure 2.1.
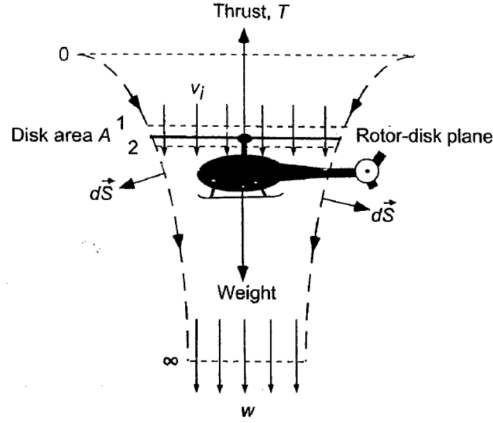
Figure 2.1: Flow model across a rotor-disk [5]. 0 and ∞ subscripts refer to the upstream and downstream far sections and A is the rotor disk area

Due to the hypotheses considered, the flow tube shrinks downstream and develops until it reaches the maximum velocity (the wake or slipstream velocity w). With these considerations (ideal and non-viscous flow) the rotor-disk action is the only cause for the change in kinetic energy of the slipstream, and the power needed for it is called induced power P_i. This is the only ideal and unavoidable loss, and the rest of non-ideal effects and losses can be taken into account in the model as non-ideal factors. If the velocity through the rotor-disk is assumed to be v_i, Equation 2.1 reduces to:

$$\dot{m} = \rho A_\infty w = \rho A_2 v_i = \rho A v_i \tag{2.4}$$

Where $\dot{m}$ is the mass flow rate and ρ is the air density. By the conservation of momentum (Equation 2.2), the thrust produced by the rotor must be equal and opposite to the force applied on the fluid ($\vec{T} = -\vec{F}$). The conservation of momentum can be expressed as

$$\vec{T} = \iint_\infty \rho(\vec{V} \cdot d\vec{S})\vec{V} - \iint_0 \rho(\vec{V} \cdot d\vec{S})\vec{V} \tag{2.5}$$

and can be reduced to the scalar Equation 2.6 if the upstream flow far from the rotor is assumed to be static:

$$T = \iint_\infty \rho(\vec{V} \cdot d\vec{S})\vec{V} = \dot{m}w \tag{2.6}$$

The energy conservation equation (Equation 2.3) can be simplified by acknowledging that the work per unit time is equal to the power consumed by the rotor ($W = T v_i$) and writing it in terms of mass flow and Equation 2.6:

$$T v_i = \underbrace{\iint_\infty \frac{1}{2}(\rho\vec{V} \cdot d\vec{S})\vec{V}^2}_{=\frac{1}{2}\dot{m}w^2} - \underbrace{\iint_0 \frac{1}{2}(\rho\vec{V} \cdot d\vec{S})\vec{V}^2}_{=0} = \frac{1}{2}\dot{m}w^2 \tag{2.7}$$

From Equation 2.6 and Equation 2.7 it can be derived that:

$$v_i = \frac{1}{2}w \iff w = 2v_i \tag{2.8}$$

5

Since the wake or slipstream velocity is two times the induced velocity, due to mass conservation the wake area must be reduced through the flow tube that is the wake. This is, $\rho A v_i = \rho A_\infty w = 2\rho A_\infty v_i$, which leads to the area ratio: $\frac{A_\infty}{A} = \frac{1}{2}$. The power necessary to hover can be obtained by using Equation 2.4 and Equation 2.8 on Equation 2.6:

$$T = \dot{m}w = 2\left(\rho A v_i\right)v_i = 2\rho A v_i^2 \implies v_i = \sqrt{\frac{T}{2\rho A}} \tag{2.9}$$

And the induced power can expressed as $P_i = T v_i$:

$$P_i = T\sqrt{\frac{T}{2\rho A}} = \frac{T^{3/2}}{\sqrt{2\rho A}} \tag{2.10}$$

$$P_i = \left(2\dot{m}v_i\right)v_i = 2\rho A v_i{}^3 \tag{2.11}$$

Equation 2.11 suggests that the required induced power P_i is minimized by reducing the induced velocity w_i (and increasing the mass flow, equivalently to the area, for a given thrust to be maintained). The thrust, torque and ideal power coefficients (C_T, C_Q and C_{P_ideal} respectively) can be defined noting that Ω is the angular velocity of the rotor, R its radius, and that the dynamic pressure ($\frac{1}{2}\rho A v^2$) is used for the nondimensionalization:

$$C_T = \frac{T}{\frac{1}{2}\rho A(\Omega R)^2} \qquad C_Q = \frac{Q}{\frac{1}{2}\rho A(\Omega R)^2 R} \qquad C_{P_\text{ideal}} = \frac{P_\text{ideal}}{\frac{1}{2}\rho A(\Omega R)^3} = \frac{C_T^{3/2}}{\sqrt{2}} \tag{2.12}$$

The nonideal effects are accounted in the power coefficient by the induced power correction factor κ (to be obtained experimentally). Thus, the induced power coefficient is:

$$C_{P_\text{ind}} = \frac{\kappa C_T^{3/2}}{\sqrt{2}} = \kappa C_{P_\text{ideal}} \tag{2.13}$$

To have an estimation of the actual power consumed by the hovering rotor, the contribution of the drag needs to be accounted. The profile power P_0 is defined as the integration of the drag force D multiplied by the angular velocity Ω along the span of the blades. In reality, drag is a function of the Reynolds number Re, the Mach number Ma and other physical features of the rotor blades such as the pitch, the diameter or the sweep. Since this is a difficult parameter to estimate precisely, P_0 is usually calculated using a constant zero-lift coefficient C_{d_0}. This coefficient corresponds to the drag for the zero-lift angle of attack and is assumed constant and independent of Ma and Re. Assuming a constant chord c over the span for a given number of blades N_b, rotor radius R and rotation speed Ω, the P_0 can be expressed as follows:

$$P_0 = \frac{1}{8}\rho N_b \Omega^3 c C_{d_0} R^4 \tag{2.14}$$

Nondimensionalized as a power coefficient, it can be simplified to:

$$C_{P_0} = \frac{P_0}{\rho A (\Omega R)^3} = \frac{1}{8} \underbrace{\left(\frac{N_b c}{\pi R} \right)}_{=\sigma} C_{d_0} = \frac{1}{8} \sigma C_{d_0} \tag{2.15}$$

Where σ is the solidity of the rotor (a parameter that encompasses the geometric properties of the rotor). With Equation 2.13 and Equation 2.15 the total actual power coefficient C_P required by the rotor can be computed:

$$C_P = C_{P_{\text{ind}}} + C_{P_0} = \frac{\kappa C_T^{3/2}}{\sqrt{2}} + \frac{\sigma C_{d_0}}{8} \tag{2.16}$$

Lastly, another parameter known as Figure of Merit (FM) is usually used as an nondimensional efficiency measure for rotors with the same Disk Loading ($DL = T/A$). It is defined as:

$$FM = \frac{\text{Ideal Power}}{\text{Actual Power}} = \frac{P_{\text{ideal}}}{P_{\text{ind}} + P_0} \tag{2.17}$$

2.2 Momentum Theory Analysis (MTA) for Rotors in Tandem Configuration

Leishman [5] adapted the standard momentum theory for tandem rotor configurations (which is the main issue that concerns this study) in two particular cases. The first approach (subsection 2.2.1) is suitable for rotors in close proximity, where there is little vertical separation since the main hypothesis is that the two rotor-disks are on the same plane. The overlapping effect appears as the interaxial distance (horizontal separation) between the rotors reduces and the rotor-disk areas overlap. Leishman also proposed an approach for the case in which the downstream rotor is located under the fully developed wake of the upstream rotor (subsection 2.2.3). The approach assumes that the upstream rotor is unaffected by the downstream rotor due to the significant separation, and that only the latter experiences the effect of the upstream wake (the overlap is produced between the fully developed upstream rotor wake area and the downstream rotor area).

The latter model has been modified to further assess the purpose of this study, allowing it to account for interplanar distance (vertical separation) besides the interaxial distance or horizontal separation. The vertical separation ranges from zero (theoretical overlap of the rotor planes) to the fully developed wake vertical distance, which was the only one regarded by the original model (theoretically, $h_{\text{dw}} \to \infty$). Consequently, it can be anticipated that the assumption of the upstream rotor remaining undisturbed by the downstream rotor loses validity as the vertical distance between the rotor planes is reduced. However, this is a simple theoretical model which also accounts for other simplifications, so this can be acknowledged.

2.2.1 MTA for Rotors in Close Proximity

According to Leishman [5], for rotors in close proximity it is assumed that the rotor-disks are on the same plane (interplanar distance $h = 0$). It is defined the ratio between the overlap area A_{ov} and the total A for twin rotors (same diameter D). The ratio m' can be computed as a function of the interaxial separation d (specifically the ratio $\delta = d/D$) as:

$$m' = \frac{A_{\mathrm{ov}}}{A} = \frac{2}{\pi}[\theta - \delta \sin \theta], \text{ where } \theta = \cos^{-1} \delta \tag{2.18}$$

T_1 and T_2 are the thrusts of the tandem rotors (which could be different). The overlap region experiences the contribution of both rotors, so its thrust is equal to $m'(T_1 + T_2)$. The induced powers for the undisturbed regions (P_1 and P_2) and for the overlap region (P_{ov}) are:

$$P_1 = \frac{(1 - m')\, T_1^{3/2}}{\sqrt{2\rho A}} \quad P_2 = \frac{(1 - m')\, T_2^{3/2}}{\sqrt{2\rho A}} \quad P_{\mathrm{ov}} = \frac{m'\,(T_1 + T_2)^{3/2}}{\sqrt{2\rho A}} \tag{2.19}$$

The overlap induced power factor can be expressed as the ratio between the required total induced power for the overlapped rotors and that for the two isolated rotors. This is $\kappa_{\mathrm{ov}} = (P_{\mathrm{ind}})_{\mathrm{ov}} / P_{\mathrm{ind}}$, and can be expanded as:

$$\kappa_{\mathrm{ov}} = \frac{P_1 + P_2 + P_{\mathrm{ov}}}{2 P_{\mathrm{iso}}} = \frac{(1 - m')\, T_1^{3/2} + (1 - m')\, T_2^{3/2} + m'\,(T_1 + T_2)^{3/2}}{T_1^{3/2} + T_2^{3/2}} \tag{2.20}$$

If it is now assumed that both rotors produce the same thrust ($T_1 = T_2 = T$), Equation 2.20 can be reduced to:

$$\kappa_{\mathrm{ov}} = 1 + (\sqrt{2} - 1)m' \approx 1 + 0.4142 m' \tag{2.21}$$

2.2.2 Wake Modelling

Streamtube modelling

Momentum theory predicts that the wake or slipstream velocity w for the fully developed wake is two times the induced velocity v (Equation 2.8). Similarly, the area of the fully developed wake is theoretically half of rotor area. However, momentum theory does not regard the vertical distance at which the wake is considered to be fully developed, nor a particular geometry for the wake. If the overlap area between the downstream rotor area and the upstream rotor wake area is to be found for any vertical distance (that is not necessarily that of the fully developed wake), the streamtube or wake needs to be modelled so that the original approach proposed by Leishman accounts also for the vertical separation, as presented in subsection 2.2.3.

According to [6], the streamtube boundary could be modelled as a hyperbolic tangent. The hyperbolic tangent function can be tuned by the constants a and b in Equation 2.22:

$$y(z) = a \cdot tanh(b \cdot z) \tag{2.22}$$

The hyperbolic tangent has asymptotes in the Y axis that tend to the a value. The rate at which the a value is approached by the asymptotes depends on b (the greater b is, the faster the a value is approached as shown in Figure 2.2 (a)). The parameter $K = R - r_{dw}$ is defined, where r_{dw} is the radius of the fully developed wake. Also, h_{dw} is defined as the downstream distance at which the wake fully develops. Equation 2.22 can be tuned so that a and b produce an asymptote that reaches the 99% of the desired ordinate value K for the abscissa h_{dw}. If Equation 2.22 is solved for b and setting $a = K$, $z = h_{dw}$ and $y(z) = 0.99K$ the resulting constant is $b = \left(\frac{1}{h_{dw}} \right) atanh(0.99)$. The resulting expression is then displaced on the abscissa axis by an offset equal to $-R$ so that it describes the radius of the wake as it develops downstream ($y(z) = a \cdot tanh(b \cdot z) - R$). In Figure 2.2 (b) the expression has been tuned for $r_{dw} = \sqrt{\frac{1}{2}} R$ (equivalent to half of the rotor area) and $h_{dw} = 2R$ (the axes have been swapped to resemble the typical rotor view). Ultimately, the expression of the wake radius along the streamwise coordinate $r_w(z)$ and the corresponding wake area $A_w(z)$:

$$r_w(z) = (R - r_{wd}) \cdot tanh \left(\frac{atanh\,(0.99)}{h_{dw}} \cdot z \right) - R$$

$$A_w(z) = \pi r_w^2(z)$$

(2.23)
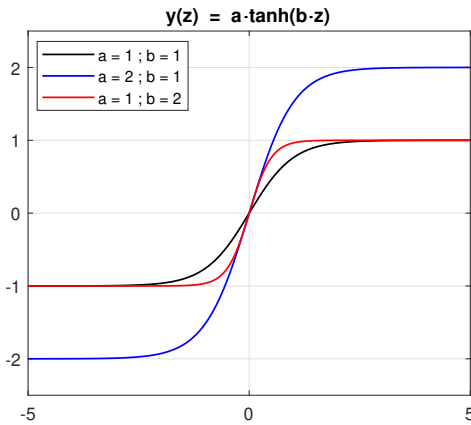
(a) Hyperbolic tangent function plots for different a and b constants
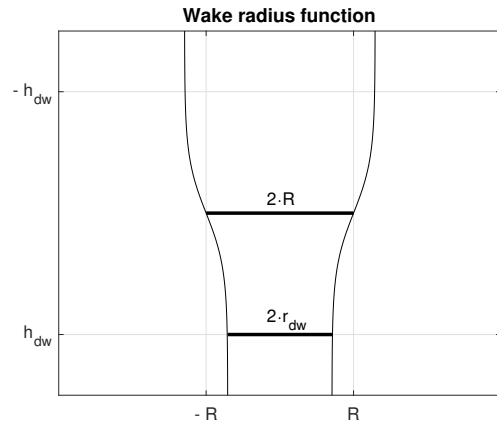
(b) Mirrored wake radius r_w function with swapped axes for $h_{dw} = 2R$ and $r_{dw} = \sqrt{\frac{1}{2}} R$

Figure 2.2: Use of the hyperbolic tangent function to model the wake boundary

Wake velocity modelling

To be consistent with momentum theory (specifically with conservation of mass), the one-dimensional velocity along the wake can be modelled as:

$$\rho v_i A = \rho v_w(z) A_w(z) \quad \Longleftrightarrow \quad v_w(z) = \frac{R}{r_w(z)} v_i$$

(2.24)

Where $v_w(z)$ is the one-dimensional velocity along the wake. According to momentum theory, the range of values for $v_w(z)$ will be $[v_i, 2v_i]$ for the vertical separation range of $[0, h_{dw}]$. For practical

purposes regarding the mathematical derivation when adapting the original Leishman model, the velocity along the wake will be expressed as:

$$v_w = \chi v_i \tag{2.25}$$

Where χ is equal to the ratio or the rotor radius and the wake radius (which varies with the vertical distance), and its range is $[1, 2]$.

Overlap of unequal diameter circular areas

Since the wake area reduces as the streamtube contracts, the overlap area factor m' definition presented in subsection 2.2.1 is no longer valid as the overlapping areas are not identical. The overlap scheme for circles of different diameter is shown in Figure 2.3 and the expression for the overlap area is indicated in Equation 2.26, as presented by Santos [4]:
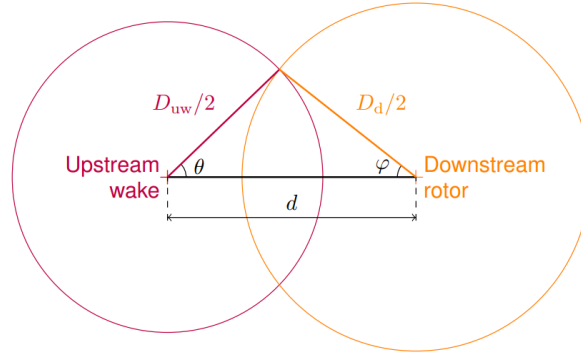
Figure 2.3: Overlap scheme for circles with different diameters [4]

$$\begin{cases} \cos\theta = \frac{D_{uw}^2 - D_d^2 + 4d^2}{4dD_{uw}} \\ \cos\varphi = \frac{D_d^2 - D_{uw}^2 + 4d^2}{4dD_d} \end{cases} \qquad A_{ov} = \frac{1}{2}\left[D_{uw}^2\theta + D_d^2\varphi - d \cdot D_{uw}\sin\theta\right] \tag{2.26}$$

The new m' is presented in Equation 2.27. The diameter D can be either D_{uw} or D_d since m' could be referred both to the upstream rotor wake area (of diameter D_{uw}) or to the downstream rotor area (of diameter D_d):

$$m' = \frac{2}{\pi}\left[\left(\frac{D_{uw}}{D}\right)^2\theta + \left(\frac{D_d}{D}\right)^2\varphi - \frac{d}{D}\frac{D_{uw}}{D}\sin\theta\right] \tag{2.27}$$

Since the upstream rotor wake diameter D_{uw} reduces along the streamwise direction, it is worth mentioning that the overlap area factor m' is also function of the vertical separation besides the horizontal separation if it is used along with the streamtube boundary model presented before.

2.2.3 MTA for a Rotor in the Wake of Another

With expressions for the area overlap with the horizontal separation and for the streamtube boundaries and wake velocity along the streamwise direction obtained in subsection 2.2.2, the effect of the upstream rotor wake overlapping with the downstream rotor can be assessed (with sensitivity for both

horizontal and vertical separations). Throughout this analysis, it is considered that both rotors have the same area A, and the subscripts u and d refer to upstream and downstream rotors. Recalling that the upstream rotor is assumed to be unaffected by the downstream rotor, the thrust produced by each of them according to momentum theory (Equation 2.6) is:

$$T_u = (\rho A v_u)(2v_u) \qquad T_d = (\dot{m}w)_d - (\dot{m}w)_u \tag{2.28}$$

The mass flow through each rotor can be expressed as:

$$\dot{m}_u = m'\rho A(\chi v_u) \qquad \dot{m}_d = (1-m')\rho A v_d + m'\rho A(v_d + \chi v_u)$$
$$w_u = v_w = \chi v_u \qquad w_d = w_d \tag{2.29}$$

Noting that the term w_d remains as the downstream rotor fully developed wake velocity, while the term w_u (which in the original theoretical model referred to the upstream rotor fully developed wake velocity $w_u = 2v_u$) has been modified to be equal to the wake velocity for any given vertical separation v_w from subsection 2.2.2. It is now assumed that both rotors produce the same thrust. As an approximation it is not completely valid but reasonable results can be obtained. With that, the thrust equality $T_u = T_d$:

$$[(1-m')\rho A v_d + m'\rho A(v_d + \chi v_u)]w_d - [m'\rho A(\chi v_u)](\chi v_u) = (\rho A v_u)(2v_u) \tag{2.30}$$

Which can be reduced to:

$$\frac{v_u^2(\chi^2 m' + 2)}{w_d} = (v_d + \chi m' v_u) \tag{2.31}$$

The application of conservation of energy (Equation 2.7) to the lower rotor yields:

$$P_d = T[(1-m')v_d + m'(v_d + \chi v_u)] = \left(\frac{1}{2}\dot{m}w^2\right)_d - \left(\frac{1}{2}\dot{m}w^2\right)_u$$
$$\implies T(v_d + \chi m' v_u) = \frac{1}{2}\rho A(v_d + \chi m' v_u)w_d^2 - \frac{1}{2}\rho A m'\chi^3 v_u^3 \tag{2.32}$$

Which can be simplified if it is noted that $T/(\rho A) = 2v_u^2$ (thrust produced by the upstream rotor in Equation 2.28, which is posteriorly assumed to be equal to the thrust of the downstream rotor):

$$2v_u^2(v_d + \chi m' v_u) = \left(\frac{w_d^2}{2}\right)\underbrace{\left(\frac{v_u^2(\chi^2 m' + 2)}{w_d}\right)}_{\text{from (2.31)}} - \frac{1}{2}m'\chi^3 v_u^3 \tag{2.33}$$

By solving Equation 2.33 for w_d, the fully developed wake velocity for the downstream rotor is:

$$w_d = \frac{2v_d + v_u m'(2\chi + \chi^3/2)}{1 + (m'\chi^2)/2} \tag{2.34}$$

The substitution of the obtained w_d into Equation 2.31 yields:

$$v_u^2(\chi^2 m' + 2) = \left(\frac{2v_d + v_u m'(2\chi + \chi^3/2)}{1 + (m'\chi^2)/2}\right)(v_d + \chi m' v_u) \tag{2.35}$$

11

Which can finally be expanded into a quadratic equation solved for v_{d} as a function of v_{u} (and also m' and χ):

$$\left(\frac{-4 - 4m'\chi^2 + 4m'^2\chi^2}{2 + m'\chi^2}\right) v_{\mathrm{u}}^2 + \left(\frac{8m'\chi + m'\chi^3}{2 + m'\chi^2}\right) v_{\mathrm{u}} v_{\mathrm{d}} + \left(\frac{4}{2 + m'\chi^2}\right) v_{\mathrm{d}}^2 = 0 \tag{2.36}$$

The solution for the induced velocity on the downstream rotor can be expressed as a function of the induced velocity on the upstream rotor and a function of the parameters m' and χ as $v_{\mathrm{d}} = G(m', \chi) \, v_{\mathrm{d}}$:

$$v_{\mathrm{d}} = \underbrace{\left(-m'\chi - \frac{m'\chi^3}{8} + \frac{\sqrt{64 + 64m'\chi^2 + 16m'^2\chi^4 + m'^2\chi^6}}{8}\right)}_{G(m', \chi)} v_{\mathrm{u}} \tag{2.37}$$

The total power P_{total} for both rotors is:

$$P_{\mathrm{total}} = \underbrace{T_{\mathrm{u}} v_{\mathrm{u}}}_{=P_{\mathrm{u}}} + \underbrace{T_{\mathrm{d}} \left(v_{\mathrm{d}} + \chi m' v_{\mathrm{u}}\right)}_{=P_{\mathrm{d}}} \tag{2.38}$$

By applying Equation 2.28 and noting that it was assumed that $T_{\mathrm{u}} = T_{\mathrm{d}} = T$, the total power P_{total} becomes:

$$P_{\mathrm{total}} = T \left(G\left(m', \chi\right) + 1 + \chi m'\right) v_{\mathrm{u}} \tag{2.39}$$

Which is simplified to Equation 2.40 by substituting v_{u} by the expression of the induced velocity on Equation 2.9:

$$P_{\mathrm{total}} = \frac{\left(G\left(m', \chi\right) + 1 + \chi m'\right) T^{3/2}}{\sqrt{2\rho A}} \tag{2.40}$$

And the overlap coefficient κ_{ov}, defined as the ratio between the total power consumed and the total powered consumed for isolated rotors, results:

$$\kappa_{\mathrm{ov}} = \frac{\left(G\left(m', \chi\right) + 1 + \chi m'\right)}{2} \tag{2.41}$$

2.2.4 Comparison of Theoretical Results

The k_{ov} values are compared in Figure 2.4. In solid lines the Leishman models for rotors in close proximity (subsection 2.2.1) and for a rotor in the fully developed wake of another (note that the modified Leishman model described in subsection 2.2.3 becomes the original Leishman approach when the maximum vertical separation considered is set, since $\chi = 2$ and m' is computed for the fully developed wake area). It can be noticed that, independently of the horizontal separation between rotors, κ_{ov} is always greater as the rotors are closer. On the other hand, the results for the modified Leishman model for a rotor in the wake of another, allowing it to account for intermediate vertical distances, are represented in dashed lines being consistent with the color code (black means fully developed wake vertical separation, blue means no vertical separation).

12
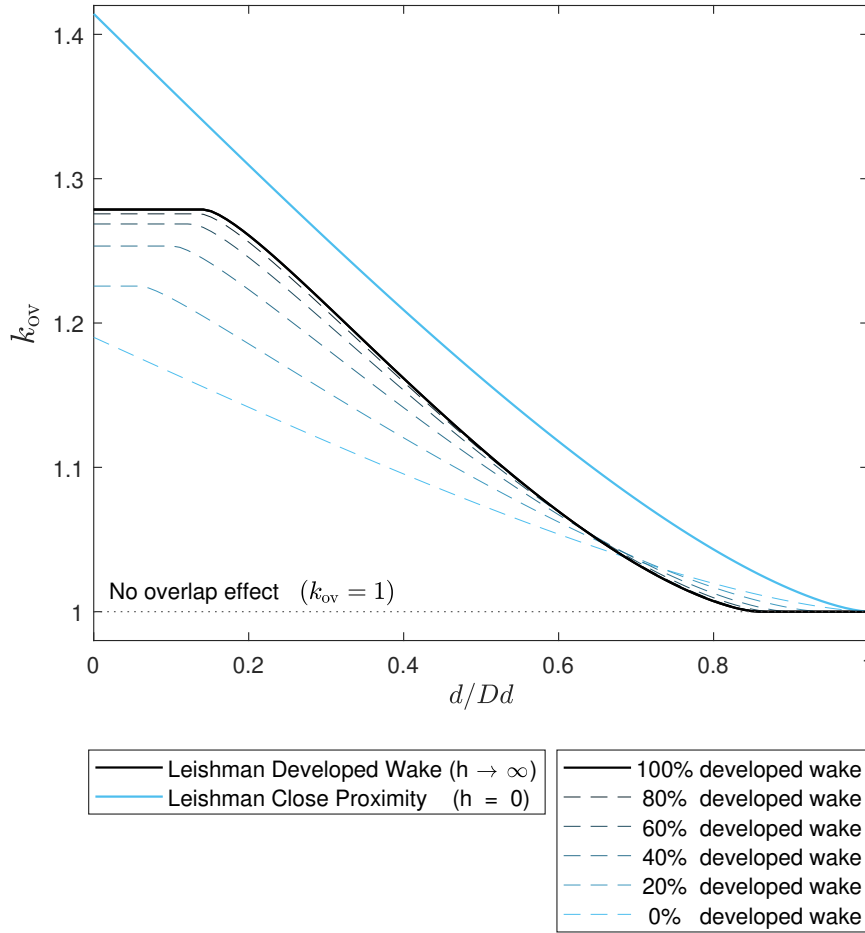
Figure 2.4: Graphical comparison of κ_{ov}. Solid lines for the Leishman theoretical approaches and dashed lines for the modified Leishman approach (accounting for intermediate vertical distances)

For the specific shape of the streamtube, it is considered in Figure 2.4 that the vertical distance at which the wake is fully developed is $h_{dw} = D_d$ (or two radii as values in literature suggest). It was anticipated that as the vertical separation approached zero, the adaptation for the Leishman rotor in wake model would become less accurate since the upper rotor was considered to be unafected and this assumption becomes less valid. However, as the the model predicts the expected behavior for values of d/D_d greater than 0.67 approximately (lower κ_{ov} values compared to the Leishman model for rotors in close proximity, although above the values for the original Leishman model for a rotor under a fully developed wake), the tendency is inverted for values under $d/D_d = 0.67$. In other words, the modified model predicts that for horizontal separations below $d/D_d = 0.67$, the effect of the overlap will be higher for greater vertical separations instead of for smaller vertical separations. There are two reasons for this to happen:

- The upstream rotor is considered to be undisturbed. The reduction in its induced power (P_u) as the vertical separation decreases is not modelled.

- The reduction of the induced power in the downstream rotor (P_d) is a weighing of two opposite effects, as clearly stated in Equation 2.38 (m' and χ, both acting on the induced upstream rotor

13

induced velocity v_{u}). The coefficient χ increases with the vertical separation since it accounts for the velocity along the wake, meanwhile the m' coefficient decreases with the vertical separation since the streamtube area (at which the overlap is produced) shrinks as the wake develops. It is possible that due to the simplifying hypothesis and assumptions dragged throughout the process to obtain a κ_{ov} expression, the weighing of each parameter needed some kind of adjustment.

2.2.5 Limitations of MTA

The Momentum Theory Analysis (MTA) is very helpful to obtain information about the trends that the parameters of importance follow with little computational effort, specially for extreme cases which would not be feasible in reality or not often put into practice (such as null separation between rotor planes or one of the rotors being in the fully developed wake of another).

However, the theoretical approaches for tandem configurations carried out along this chapter have several limitations. To start with, these approaches restrict the thrust and the area to be the equal on both rotors, as they were originally developed for tandem helicopters in hover (in which the torque balance is mandatory, so thrust equality is often achieved due to the coupling of the twin rotor shafts). This is a huge limitation for the study of tandem configurations, since those conditions would not always be the case for small UAVs with a tandem configuration (in which most applications implement several pairs of rotors of opposing rotation to achieve the torque balance, and their speed can be regulated independently).

Chapter 3

Experimental Setup and Methodology

With the experimental approach it is intended to carry out several tests involving the aerodynamic interactions present in tandem rotor configurations with three rotors (specific tests defined in section 3.2). The quantification of thrust loss on the back rotor due to the aerodynamic interaction between rotors is of special interest, and along with the torque produced by the rotor, some additional parameters of interest for rotorcrafts as the Figure of Merit (FM) can be obtained. In order to perform the experiments, an instrumented test bench which allows to measure the thrust and torque produced by the mounted propellers is used (presented in section 3.1). Before its use, the experimental setup needs to be calibrated (as presented in subsection 3.1.4) and verificated (subsection 3.1.8).

3.1 Experimental Test Bench

3.1.1 Original Test Bench

The experimental set-up is an adaptation from the original test bench designed by Amado [3], which allowed for the study of coaxial configuration (capable of rotor-plane separation, referred to as h distance). The original test bench (Figure 3.1) had two Instrumented Tubes (IT) on top of which two brushless direct current (BLDC) electric motors where placed along the propellers to test. IT1 had 3 strain gage bridges allowing it to measure the forces (F_x and F_y) and the torque (M_x) produced by the propeller. IT2 only measures torque. Additionally, they were provided angular velocity Ω sensors located above the BLDC motors, and Current and Voltage sensors connected to the motors.
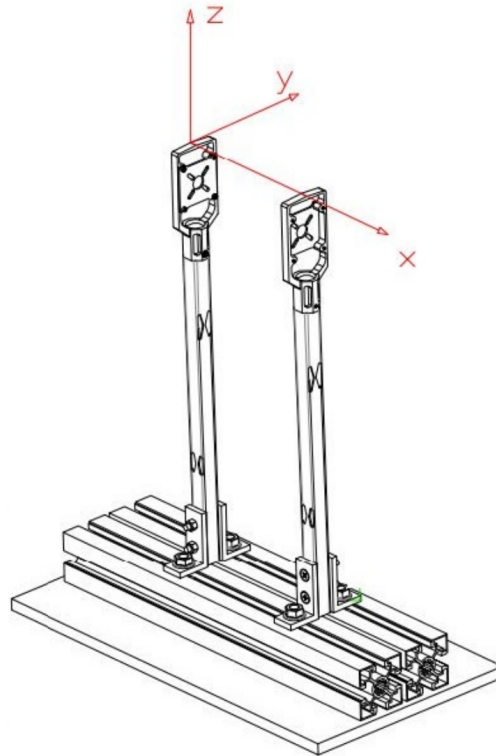
Figure 3.1: Original experimental setup scheme by Amado [3]

3.1.2 Modified Test Bench

The test bench was later modified by Santos [4] to allow for interaxial separation (referred to as d distance) through additional sets of rail beams. In this way, the IT can slide and be attached to the sliding rail beam along the X axis, and these moving rail beams can also be moved in the Y axis along the fixed rail beams on the bottom. Santos carried out his studies maintaining the two IT setup, although he intended to add a third tube (uninstrumented, referred to as UT) for a symmetric layout. In this work, the third tube was added. The final test bench scheme along with the frame of reference that will be used is shown in Figure 3.2, whereas the the actual setup in pictured in Figure 3.3.
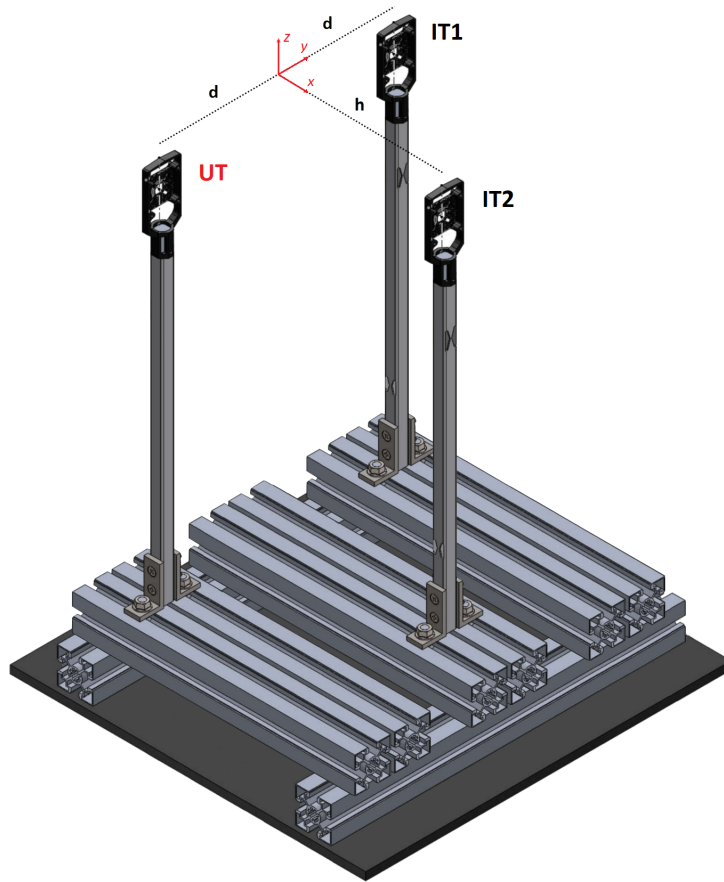
Figure 3.2: Experimental setup scheme with the frame of reference that will be used along the work
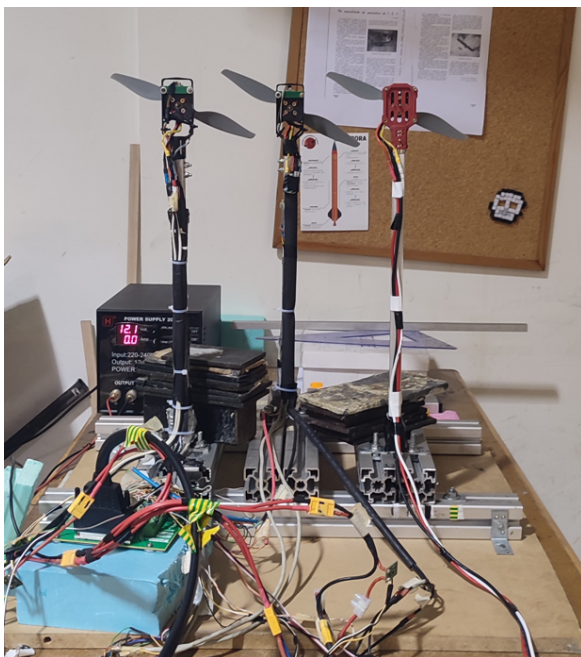
(a) Back view of the experimental setup
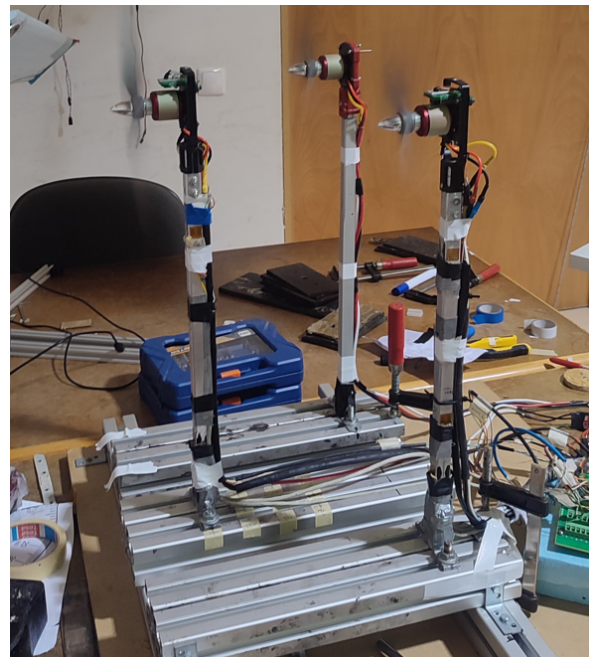
(b) Experimental setup in use

Figure 3.3: Experimental setup

3.1.3 Control/Acquisition Software and Experimental Methodology

The Labview [7] software is capable of handling the data acquisition for all the sensors outputs and the control of the angular speed of the motors simultaneously in real time. The sensors that are not strain gages (current, voltage and angular velocity Ω) are physically connected to an auxiliary connection board from National Instruments (NI CB-68LP), and the sensor outputs ultimately reach the terminal through a data acquisition board (NI PCIe-6323). The pulse width modulation (PWM) signals for the motor speed control also use this support to carry and convert them to analog signals. On the other hand, the strain gage (SG) output readings are converted to digital signals and carried to the terminal with the universal serial bus (USB) data acquisition (DAQ) board, the NI USB DAQ 9237. Labview allows to create custom programs with a block diagram design approach.

The formerly mentioned students [3] [4] developed a utility which allows to select the target RPM of the motors on IT1 and IT2. The desired speeds are achieved by means of a very simple proportional control loop that has constant gains K_{P1} and K_{P2} respectively for IT1 and IT2 and uses the Ω sensors as feedback for the PWM signals adjustment. During the experiments, the data will not start being recorded until the angular velocity readings have been on an acceptable range (desired $\mathrm{RPM} \pm 75$ RPM) for a period of 5 seconds. It is important to note that the motors mounted on the uninstrumented tube (UT) does not have any Ω sensor, and consequently has no control loop. It uses the same PWM signal as the motor on IT1 (resulting from a closed loop control) since both motors and their ESC are exactly the same (a new set of 3 motors EMP [8] N2830/11 was acquired for this study) and they are intended to carry the same propeller since they are in the same rotor plane (section 3.2). The validity of this approach was checked by mounting the UT motor (that uses the duplicated signal of the IT1 motor) on IT2, so that its speed can be measured. The RPM of the motors would not differ more than $50\ \mathrm{RPM}$ when setting the IT1 motor to a wide range of target speeds. A block diagram representation of the experimental setup, including the the control loops for the angular speeds of the motors along with the rest of variables measured is presented in Figure 3.4.
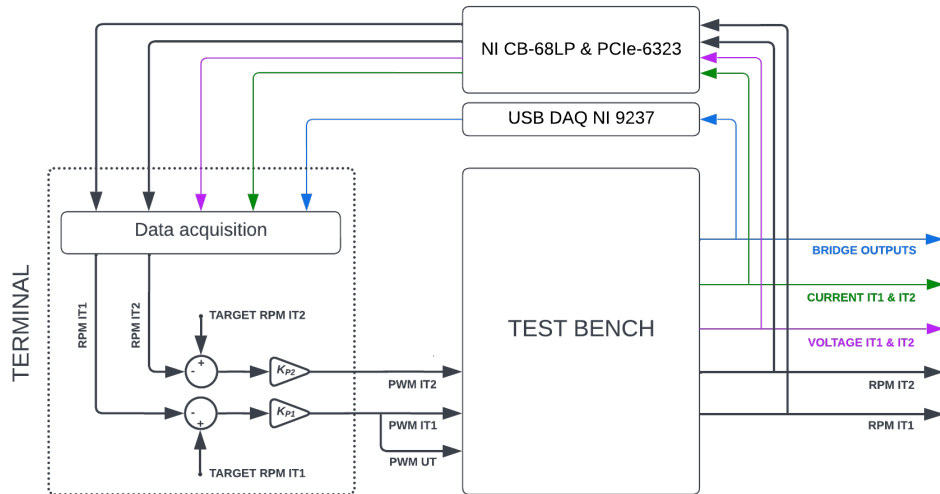
Figure 3.4: Block diagram showing the proportional control loops for the angular speeds of the engines along with the rest of variables measured

For each combination of propellers to test, several configurations regarding d and h distances are to be set. The systematic methodology followed during the measurements starts by attaching and securing the chosen propellers on the motors. The interaxial separation d is applied by displacing and clamping the lateral rail beams (on which IT1 and UT are clamped permanently at the same X position respectively, that is the same rotor plane) on the Y axis along the fixed base rail beams. The rotor plane (or interplanar) separation h is applied by sliding and clamping the IT2 on the X axis along the central rail beams (which remain clamped themselves to the fixed base rail beams, always at the same Y position). Once the position is secured, the rotation speeds for the motors are selected in the Labview user interface and the program is run. As described before, the motors will eventually reach the desired RPM and the data recording for the sensors will last for 18 seconds with an acquisition frequency of $10000\ \mathrm{Hz}$. This is carried out for every rotation speed and h and d combination desired to test, and this process is repeated for every propeller combination planned to test. The output files are in *.TDMS format, which can be imported into Matlab [9] for postprocess analysis.

3.1.4 Calibration Procedure

The followed procedure is that of the static calibration originally carried out by Amado [3], but applying a load-unload test plan. The mathematical structure is the same (a weighted variation of the Least-Squares method, described in subsection 3.1.5). The output linearity of the bridges was verified by Amado [3]. For IT1, since the force values will be expected to be under 10 N, the calibration ranges from [-25, 25] N in the F_x and F_y directions with increments of 1 N from 0 to 10 N, and with increments of 5 N subsequently. The positive and negative ranges of the calibration are carried out separately, with forces applied on opposite direction by turning 180° the IT1 as Figure 3.5 suggests.
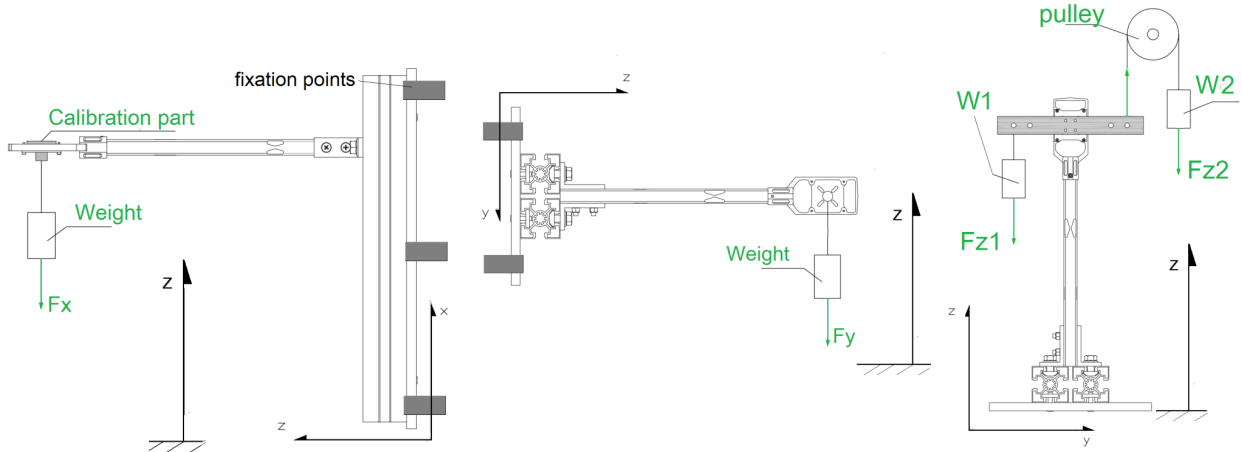
Figure 3.5: Calibration configurations for $-F_x$, F_y and M_x directions respectively [3]

For the momentum M_x direction in both IT1 and IT2 an analogue procedure was followed by using a pulley and 2 threads, with the torque range being [-0.85, 0.85] Nm. The specific loading plans for the force and moment calibration are shown in Table 3.1 and Table 3.2 respectively.

Table 3.1: Loading plan for F_x and F_y forces for IT1

Index	Applied Weight [N]	Index	Applied Weight [N]	Index	Applied Weight [N]
0	0.000	9	8.911	18	7.921
1	0.971	10	9.906	19	6.928
2	1.964	11	14.941	20	5.935
3	2.954	12	19.977	21	4.943
4	3.946	13	25.014	22	3.946
5	4.943	14	19.977	23	2.954
6	5.935	15	14.941	24	1.964
7	6.928	16	9.906	25	0.971
8	7.921	17	8.911	26	0.000

Table 3.2: Loading plan for M_x toque for both IT1 and IT2

Index	Applied Torque [Nm]	Index	Applied Torque [Nm]	Index	Applied Torque [Nm]
0	0.000	7	0.646	14	0.060
1	0.030	8	0.886	15	0.030
2	0.060	9	0.646	16	0.000
3	0.118	10	0.411		
4	0.176	11	0.293		
5	0.293	12	0.176		
6	0.411	13	0.118		

3.1.5 Weighted Least-Squares Method

The Weighted Least-Squares (WLS) approach has been implemented in Matlab. The method requires the calibration data to be arranged in two matrices: the set of static loads applied as an $N \times k$

matrix ($\mathbf{Y}$) and the bridge response data as a $N \times k$ matrix ($\mathbf{R}$), where N is the total number of measures among all the tests and k is the number of degrees of freedom or load types ($k = 3$ for IT1 and $k = 1$ for IT2).
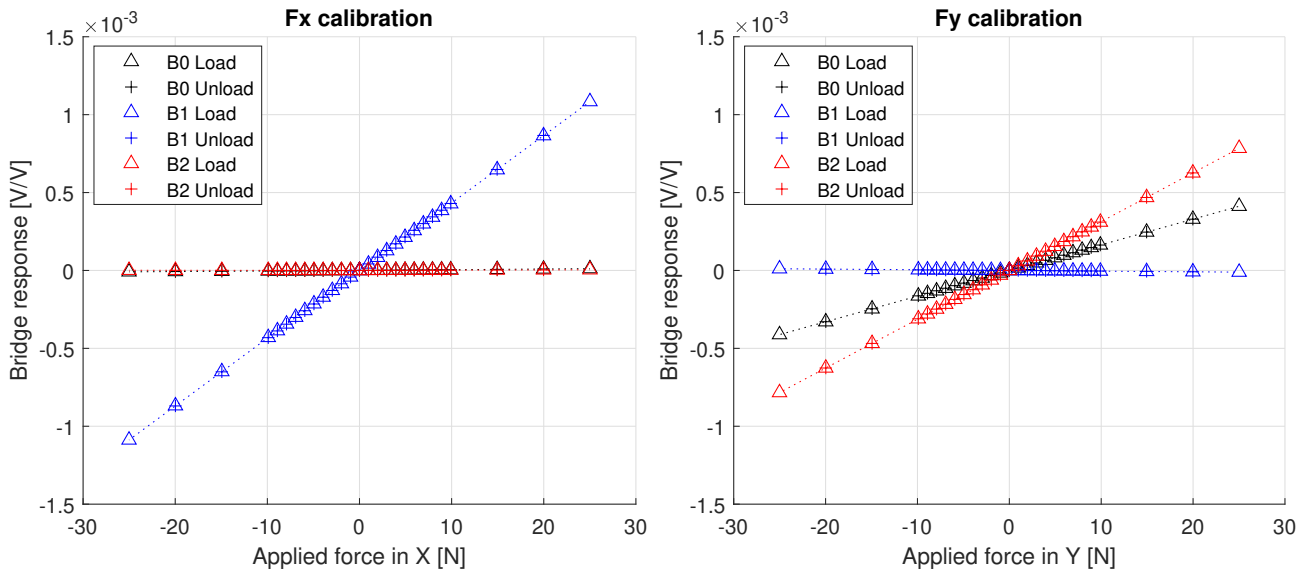
Figure 3.6: Calibration curves for F_x and F_y on IT1

The calibration data contained is graphed to visualize the bridge activation for each direction in Figure 3.6 for the forces on IT1 (bridges 0, 1 and 2). The calibration curves for the torque in both IT1 and IT2 (bridge 3) are presented in Figure 3.7.
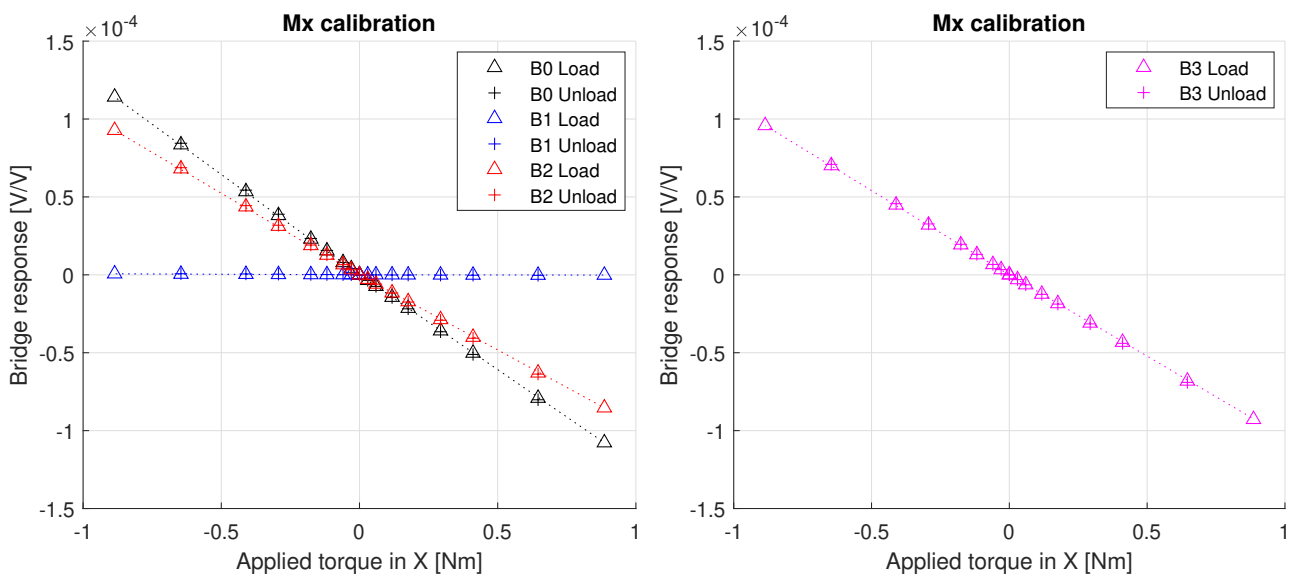
Figure 3.7: Calibration curves for M_x on IT1 and IT2

21

The WLS procedure starts by obtaining a first estimation of the calibration matrix $\mathbf{C}$, from which a first approximation of the weights matrix $\mathbf{W}$ can be computed. An intermediate iteration of the $\mathbf{C}$ is obtained with the initial $\mathbf{W}$ matrix, and the final $\mathbf{W}$ matrix is computed with the intermediate $\mathbf{C}$ matrix. Lastly, with the final $\mathbf{W}$ estimation and the covariance matrix, the final calibration matrix $\mathbf{C}$ is computed. The first estimation of $\mathbf{C}$ is calculated considering that $\varepsilon = 0$ as in Equation 3.1:

$$\mathbf{Y} = \mathbf{R}\mathbf{C} + \varepsilon \rightarrow \mathbf{C} = \left(\mathbf{R}^T\mathbf{R}\right)^{-1}\mathbf{R}^T\mathbf{Y} \tag{3.1}$$

The first estimation of the weight matrix $\mathbf{W}$ is obtained by means of the auxiliary matrix $\mathbf{V_w}$:

$$\mathbf{W} = \mathbf{V_w}^{-1} \tag{3.2}$$

The matrix $\mathbf{V_w}$ accounts for the uncertainties of the masses (u_L) used in the calibration but also for the uncertainties introduced by the misalignment of the weight threads, vibrations and other kind of perturbations from other sources such as human errors. The $\mathbf{V_w}$ matrix is a diagonal $N \times N$ matrix (where N is the total number of weight loads applied on the calibration) of the form:

$$\mathbf{V_w} = \begin{bmatrix} (\sigma_{\text{tot}})^2_{1,1} & & & & & & & \\ & \ddots & & & & & & \\ & & (\sigma_{\text{tot}})^2_{1,N_1} & & & & & \\ & & & (\sigma_{\text{tot}})^2_{2,1} & & & & \\ & & & & \ddots & & & \\ & & & & & (\sigma_{\text{tot}})^2_{2,N_2} & & \\ & & & & & & (\sigma_{\text{tot}})^2_{3,1} & \\ & & & & & & & \ddots \\ & & & & & & & & (\sigma_{\text{tot}})^2_{3,N_3} \end{bmatrix} \tag{3.3}$$

Where N_i are the number of loading weights applied in each type of load (F_x, F_y and M_x respectively, which satisfy $N_1 + N_2 + N_3 = N$) and $\sigma_{\text{tot }i,j}$ are the total uncertainty terms, given by:

$$\left(\sigma^2_{\text{tot}}\right)_{i,j} = \sigma^2_i + u^2_{ij} \tag{3.4}$$

Where u_{ij} are the uncertainties of the forces and moments due to the apparatus precision (in the weights and moment arm measurements) which are obtained directly from the measurements, and σ_i (where the i subindex refers to the load type or degree of freedom) accounts for the rest of uncertainties previously mentioned and their values are obtained based on the standard deviation as follows:

$$\sigma^2_i = \frac{1}{N-m}\sum_{k=1}^{N}\left(y_{k,i} - y_{\hat{k},i}\right)^2 \tag{3.5}$$

Where N is the total number of weight sets applied in the whole calibration, m is the number of degrees of freedom (equal to 3 for IT1 and equal to 1 for IT2), $y_{\hat{k},i}$ are the estimated loads for the i_{th} degree of freedom by applying Equation 3.1 with the first estimation of the $\mathbf{C}$ matrix, and $y_{k,i}$ are the values of the true applied loads for the i_{th} degree of freedom or load type. On the other hand, the uncertainties of the forces and moments u_{ij} are calculated following the standard uncertainty propagation rule. For the forces F_x and F_y, the expression is $F = mg$ and if the gravity acceleration is considered to be $g = 9.81\,\mathrm{m/s^2}$ without uncertainty, the uncertainty for the force is $u_F = g \times u_m$ where u_m is the uncertainty of the calibration masses (equal of the precision of the apparatus, $0.0001\,\mathrm{kg}$). For the moment, the expression is $M = F\,l = (mg)\,l$ where l is the arm of the moment (equal to $6\,\mathrm{cm}$ in the piece used for the calibration). The uncertainty has two sources and can be expressed as $u_M = g(l \times u_m + m \times u_l)$ where u_l is the uncertainty of the arm (equal to the apparatus precision, which was $0.001\,\mathrm{m}$ for a conventional ruler). The uncertainties related to the loads are shown in Table 3.3 and Table 3.4:

Table 3.3: Uncertainties in forces

Index	$u_F \times 10^3[\mathrm{N}]$	Index	$u_F \times 10^3[\mathrm{N}]$	Index	$u_F \times 10^3[\mathrm{N}]$
0	0.00	9	8.83	18	7.85
1	0.98	10	9.81	19	6.87
2	1.96	11	10.79	20	5.89
3	2.94	12	11.77	21	2.91
4	3.92	13	12.75	22	22
5	4.91	14	11.77	23	232
6	5.89	15	10.79	24	24
7	6.87	16	9.81	25	1.96
8	7.85	17	8.83	26	0.98

Table 3.4: Uncertainties in moment

Index	$u_M \times 10^3[\mathrm{Nm}]$	Index	$u_M \times 10^3[\mathrm{Nm}]$	Index	$u_M \times 10^3[\mathrm{Nm}]$
0	0.00	7	22.48	14	2.34
1	1.23	8	30.59	15	1.23
2	2.34	9	22.48	16	0.00
3	4.40	10	14.52		
4	6.46	11	10.48		
5	10.48	12	6.46		
6	14.52	13	4.40		

By means of Equation 3.2, the $\mathbf{W}$ matrix can be obtained, and the calibration matrix $\mathbf{C}$ can be reevaluated to its intermediate iteration by:

$$\mathbf{C} = \left(\mathbf{R}^T\mathbf{W}\mathbf{R}\right)^{-1}\mathbf{R}^T\mathbf{W}\mathbf{Y} \tag{3.6}$$

With the intermediate $\mathbf{C}$ matrix, the final estimations of the weight matrix $\mathbf{w}$ can be computed as:

$$\mathbf{W}_{\mathrm{i}} = \left(\mathbf{V}_{\mathrm{w}} + \mathbf{D}_{\mathrm{i}}\mathbf{V}_{\mathrm{R}}\mathbf{D}_{\mathrm{i}}^T\right)^{-1} \tag{3.7}$$

Where the subindex i refers to the degree of freedom or load type, meaning that several weight matrices will be obtained (3 for IT1 and 1 for IT2). $\mathbf{V}_R$ is a diagonally symmetric matrix. It is calculated using values from the repetition of several calibration tests. The diagonal terms are the variances between the readings of the strain gage outputs, and the off-diagonal terms to the covariances.

$$
\mathbf{V}_R = \begin{bmatrix}
u\left(r_{1,1}, r_{1,1}\right) & u\left(r_{1,1}, r_{2,1}\right) & \cdots & u\left(r_{1,1}, r_{N,1}\right) & u\left(r_{1,1}, r_{1,2}\right) & \cdots & u\left(r_{1,1}, r_{N,3}\right) \\
u\left(r_{2,1}, r_{2,1}\right) & u\left(r_{2,1}, r_{2,1}\right) & \cdots & u\left(r_{2,1}, r_{N,1}\right) & u\left(r_{2,1}, r_{1,2}\right) & \cdots & u\left(r_{2,1}, r_{N,n}\right) \\
\vdots & \vdots & \ddots & \vdots & \vdots & \ddots & \vdots \\
u\left(r_{N,1}, r_{1,1}\right) & u\left(r_{N,1}, r_{2,1}\right) & \cdots & u\left(r_{N,1}, r_{N,1}\right) & u\left(r_{N,1}, r_{1,2}\right) & \cdots & u\left(r_{N,1}, r_{N,n}\right) \\
u\left(r_{2,1}, r_{1,1}\right) & u\left(r_{1,1}, r_{2,1}\right) & \cdots & u\left(r_{1,2}, r_{N,1}\right) & u\left(r_{1,2}, r_{1,2}\right) & \cdots & u\left(r_{1,2}, r_{N,n}\right) \\
\vdots & \vdots & \ddots & \vdots & \vdots & \ddots & \vdots \\
u\left(r_{N,n}, r_{1,1}\right) & u\left(r_{N,n}, r_{2,1}\right) & \cdots & u\left(r_{N,n}, r_{N,1}\right) & u\left(r_{N,n}, r_{1,2}\right) & \cdots & u\left(r_{N,n}, r_{N,n}\right)
\end{bmatrix} \tag{3.8}
$$

The covariances and variances can be calculated from the matrix $\mathbf{R}_{\text{global}}\ [N \times k, n]$ (where n is the number of repetitions of the calibration process).

$$
\mathbf{R}_{\text{global}} = \begin{bmatrix}
1 & \rightarrow & n \\
& & \\
1 & & \\
\vdots & & [R1] \\
N & & \\
& & \\
1 & & \\
\vdots & & [R2] \\
N & & \\
& & \\
1 & & \\
\vdots & & [R3] \\
N & &
\end{bmatrix} \tag{3.9}
$$

The columns (R_1, R_2 and R_3 corresponding to the three load types in IT1) of the several $\mathbf{R}_n$ matrices are concatenated in a unique column, and the latter are concatenated horizontally. The $\mathbf{V}_R$ matrix can be obtained by transposing the matrix $\mathbf{R}_{\text{global}}$ and using it as input to the *cov* function in Matlab. Since the test plan follows a load-unload plan, only one set of measurements was taken ($n = 1$) and $\mathbf{V}_R$ is a scalar. The other new matrices to compute in Equation 3.7 are matrices $\mathbf{D}_i$. They are k different matrices of size $N \times k \cdot N$ and use the sensitivity coefficients of the intermediate matrix $\mathbf{C}$. Formally, they are obtained by taking partial derivatives on Equation 3.13:

$$\mathbf{D_i} = \begin{bmatrix} \frac{\partial y_{1,i}}{\partial r_{1,1}} & \frac{\partial y_{1,i}}{\partial r_{2,1}} & \cdots & \frac{\partial y_{1,i}}{\partial r_{N,3}} & \frac{\partial y_{1,i}}{\partial r_{1,2}} & \cdots & \frac{\partial y_{1,i}}{\partial r_{N,3}} \\ \frac{\partial y_{2,i}}{\partial r_{1,1}} & \frac{\partial y_{2,i}}{\partial r_{2,1}} & \cdots & \frac{\partial y_{2,i}}{\partial r_{N,1}} & \frac{\partial y_{2,i}}{\partial r_{1,2}} & \cdots & \frac{\partial y_{2,i}}{\partial r_{N,3}} \\ \vdots & \vdots & \ddots & \vdots & \vdots & \ddots & \vdots \\ \frac{\partial y_{N-1,i1}}{\partial r_{1,1}} & \frac{\partial y_{N-1,i}}{\partial r_{2,1}} & \cdots & \frac{\partial y_{N-1,i}}{\partial r_{N,1}} & \frac{\partial y_{N-1,i}}{\partial r_{1,2}} & \cdots & \frac{\partial y_{N-1,i}}{\partial r_{N,3}} \\ \frac{\partial y_{N,i}}{\partial r_{1,1}} & \frac{\partial y_{N,i}}{\partial r_{2,1}} & \cdots & \frac{\partial y_{N,i}}{\partial r_{N,1}} & \frac{\partial y_{N,i}}{\partial r_{1,2}} & \cdots & \frac{\partial y_{N,i}}{\partial r_{N,3}} \end{bmatrix} \tag{3.10}$$

However, only the sensitivity coefficients whose subscripts match correspond to the same load and have values different from 0. The previous equation can can be reduced to:

$$\mathbf{D_i} = \begin{bmatrix} \frac{\partial y_{1,i}}{\partial r_{1,1}} & 0 & \cdots & 0 & \frac{\partial y_{1,i}}{\partial r_{1,2}} & \cdots & 0 \\ 0 & \frac{\partial y_{2,i}}{\partial r_{2,1}} & \cdots & 0 & 0 & \cdots & 0 \\ \vdots & \vdots & \ddots & \vdots & \vdots & \ddots & \vdots \\ 0 & 0 & \cdots & 0 & 0 & \cdots & 0 \\ 0 & 0 & \cdots & \frac{\partial y_{N,i}}{\partial r_{N,1}} & 0 & \cdots & \frac{\partial y_{N,i}}{\partial r_{N,3}} \end{bmatrix} \tag{3.11}$$

Where the derivatives $\frac{\partial y_{p,i}}{\partial r_{p,j}}$ can be written as $c_{j,i}$ (this is, $\frac{\partial y_{p,i}}{\partial r_{p,1}} = c_{1,i}$; $\frac{\partial y_{p,i}}{\partial r_{p,2}} = c_{2,i}$; $\frac{\partial y_{p,i}}{\partial r_{p,3}} = c_{3,i}$). $\mathbf{D_i}$ matrices can be easily computed following the notation in Equation 3.12, through the horizontal concatenation (noted by $\oplus$) of k $N \times N$ matrices:

$$\left. \begin{array}{ll} \mathbf{D_i} = \mathbf{I_{1,i}} \oplus \mathbf{I_{2,i}} \oplus \mathbf{I_{3,i}} & \text{for IT1} \\ \mathbf{D_i} = \mathbf{I_1} & \text{for IT2} \end{array} \right\} \quad \text{where } \mathbf{I_{i,j}} = \mathbf{C_{i,j}} \mathbf{I_N} \tag{3.12}$$

Where $\mathbf{I_N}$ are identity matrices of size N. With that, the $\mathbf{W_i}$ matrices can be obtained and applied to Equation 3.6. Since there are i weight matrices (one for each degree of freedom), several $\mathbf{C_i}$ final iteration matrices are obtained. The ultimate $\mathbf{C}$ matrix is built by concatenating the columns from the corresponding load type of the several $\mathbf{C_i}$ matrices in a final $\mathbf{C}$ matrix (for IT1 the first column would be the first of the matrix $\mathbf{C_1}$, the second column the second one in matrix $\mathbf{C_2}$ and the third column the third in $\mathbf{C_3}$). The calibration matrix can be finally applied to the bridge output data:

$$\hat{y} = r\mathbf{C} \tag{3.13}$$

3.1.6 Calibration Coefficient Results

The obtained calibration coefficients after the WLS approach are shown as matrices in Equation 3.14 for IT1. There are two matrices, each of one corresponding to the direction of the applied load. For this study the thrust and the torque will always have the same direction (since only one direction of rotation is considered), meaning that only the matrix $\mathbf{C_{pos}^1}$ will be used for thrust and $\mathbf{C_{neg}^1}$ will be used for torque (since for the selected counterclockwise direction of rotation the torque direction is the negative according to the calibration).

$$\mathbf{C_{pos}^1} = \begin{bmatrix} -5.3584 \times 10^2 & -4.3589 \times 10^4 & -1.4001 \times 10^4 \\ 2.3089 \times 10^4 & 2.5217 \times 10^2 & 1.2149 \times 10^2 \\ 5.8700 \times 10^2 & 5.4847 \times 10^4 & 7.3662 \times 10^3 \end{bmatrix}$$

$$(3.14)$$

$$\mathbf{C_{neg}^1} = \begin{bmatrix} -7.1300 \times 10^2 & -4.5521 \times 10^4 & -1.3469 \times 10^4 \\ 2.3002 \times 10^4 & 4.2267 \times 10^2 & 1.1599 \times 10^2 \\ 6.7904 \times 10^2 & 5.5866 \times 10^4 & 7.0862 \times 10^3 \end{bmatrix}$$

For the IT2, the resulting matrices are shown in Equation 3.15 and are scalars, since only one bridge was used to estimate the torque. Anew, only the $\mathbf{C_{pos}^2}$ will be used.

$$\mathbf{C_{pos}^2} = \begin{bmatrix} -7.9009 \times 10^3 \end{bmatrix}$$
$$\mathbf{C_{neg}^2} = \begin{bmatrix} -7.9908 \times 10^3 \end{bmatrix}$$

$$(3.15)$$

3.1.7 Measure Uncertainty Computation

The uncertainty existing in the calibration coefficients was computed according to the specifications in [10]. The error matrix $\mathbf{V_p} = \left(\mathbf{R}^T \mathbf{W} \mathbf{R}\right)$ has diagonal elements which correspond to the variances or squared uncertainties u_c^2. The propagation law of uncertainty in the estimated loads (noted by subscript $\hat{y}$) for the bridge outputs r can be expressed as:

$$\mathbf{V_{\hat{y}_i}} = r\mathbf{V}_{p_i} r^T = r\left(\mathbf{R}^T \mathbf{W_i} \mathbf{R}\right) r^T \tag{3.16}$$

For IT1, the error matrices for the positive and negative directions associated with the calibration data are:

$$\mathbf{V_{pos}^1} = \begin{bmatrix} 3.9011 \times 10^1 & 1.8967 \times 10^0 & 2.0916 \times 10^1 \\ 1.1885 \times 10^2 & 5.7787 \times 10^0 & 6.3724 \times 10^1 \\ 2.6729 \times 10^1 & 1.2995 \times 10^0 & 1.4330 \times 10^1 \end{bmatrix}$$

$$(3.17)$$

$$\mathbf{V_{neg}^1} = \begin{bmatrix} 3.7603 \times 10^1 & 1.8898 \times 10^0 & 2.0202 \times 10^1 \\ 1.1813 \times 10^2 & 5.9366 \times 10^0 & 6.3461 \times 10^1 \\ 2.4707 \times 10^1 & 1.2416 \times 10^0 & 1.3273 \times 10^1 \end{bmatrix}$$

The error matrices for IT2 are a scalar since only one bridge was used for the calibration of the torque. As a result, the uncertainties are higher.

$$\mathbf{V_{pos}^2} = \begin{bmatrix} 1.4748 \times 10^3 \end{bmatrix}$$
$$\mathbf{V_{neg}^2} = \begin{bmatrix} 1.4646 \times 10^3 \end{bmatrix}$$

$$(3.18)$$

3.1.8 Calibration Verification

The calibration coefficients are verified by testing the selected propellers (subsection 3.2.1) in isolation for a range of angular velocities Ω. The thrust and torque values obtained are compared to those provided by the manufacturer APC [11] and those obtained by CFD simulations using own 3D CADs of the propellers (section 4.7). Additionally, the Figures of Merit (FM) for the isolated rotors computed with the thrust and torque of the different data sets are presented. The data provided by APC has been calculated using the NASA Transonic Airfoil Analysis Computer Program [12]. The program uses the potential flow theory (also known as vortex theory) to compute the lift and drag around a series of 2D profiles (the real geometric data of the propeller airfoil sections used in the NASA software is provided by APC and used to build 3D CADs in section 4.2). Due to this reason, APC warns that the values may not match the experimental data for all scenarios.

The tests were performed on APC 10×6E, 9×6E and 8×6E for both IT2 and IT2 with increments in Ω of 500 RPM for the range of [1500, 4500] RPM, while the APC data has increments of 1000 RPM and the CFD values are available for the speeds of 2000, 3000 and 4000 RPM (selected angular velocities Ω for the experiments, subsection 3.2.5). In Figures 3.8, 3.9 and 3.10 the comparisons between APC, experimental and CFD values are presented for thrust on IT1, torque on IT1 and torque on IT2 respectively. In the left graphs the error bars are computed accordingly to subsection 3.1.7 with confidence intervals of the 95% (2σ), while on the right graphs the CFD values are displayed along with the rest (without error bars in the experimental values for the sake of clarity) .
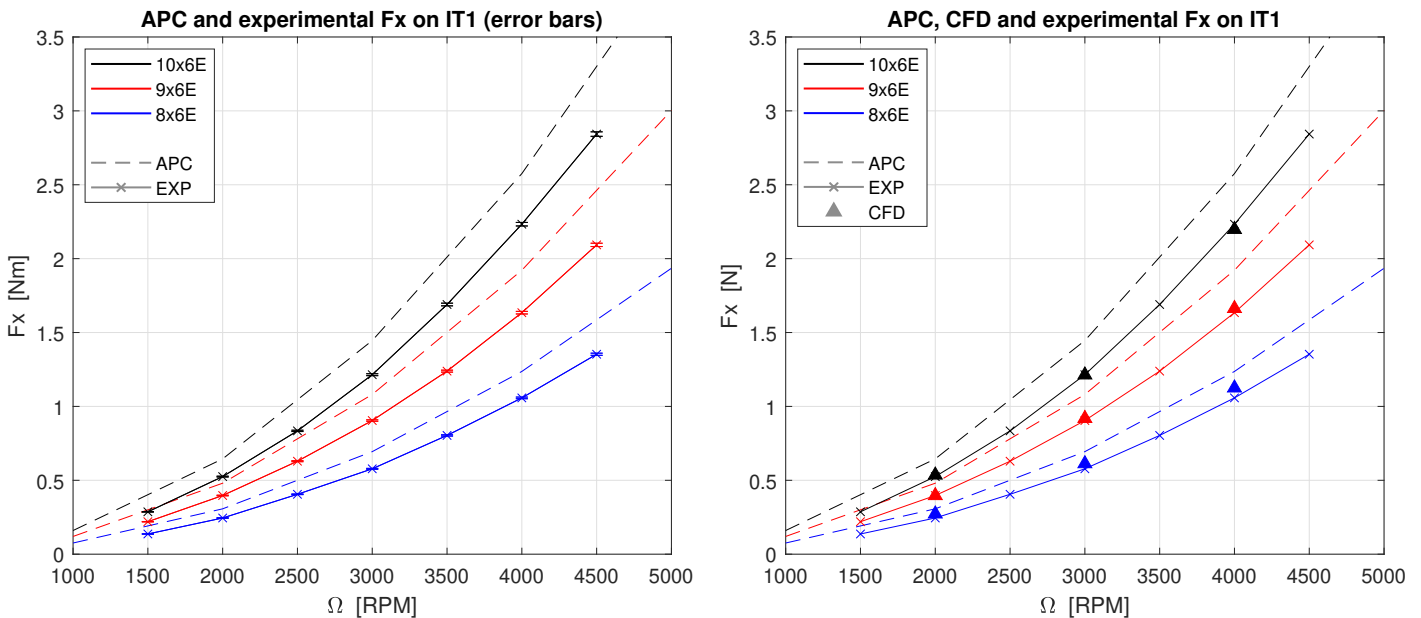
Figure 3.8: APC, CFD and computed experimental values for thrust (F_x) as function of Ω for the selected propellers on IT1

Figure 3.9: APC, CFD and computed experimental values for torque (M_x) as function of Ω for the selected propellers on IT1

The resulting curves for IT1 show that the measurements are very solid for thrust although for torque the expected trend is not followed quite as smoothly since there is a wider variability in the measures, and more uncertainty is associated with the results. All in all, the test bench proves to be satisfactory. Acknowledging that the CFD and the experimental values are much closer between them, the APC values for thrust seem to be quite overpredicted and the torque ones seem to be slightly underpredicted (specially for lower speeds and smaller propellers, as APC suggests).
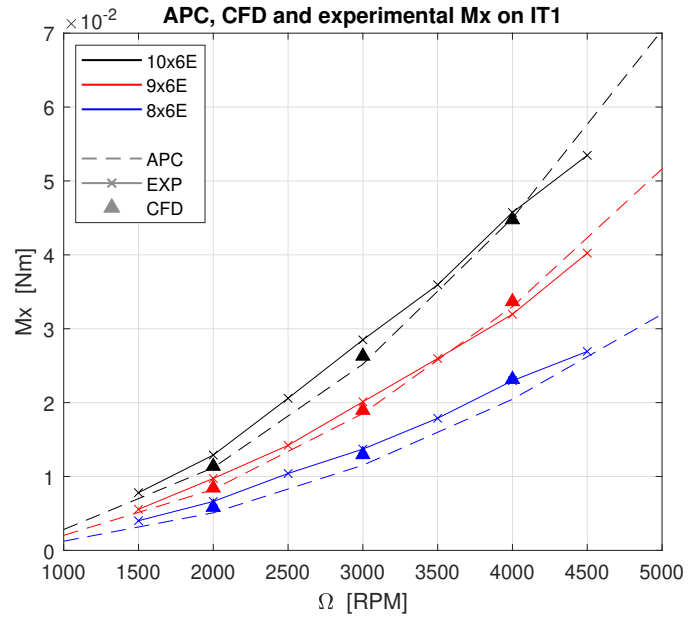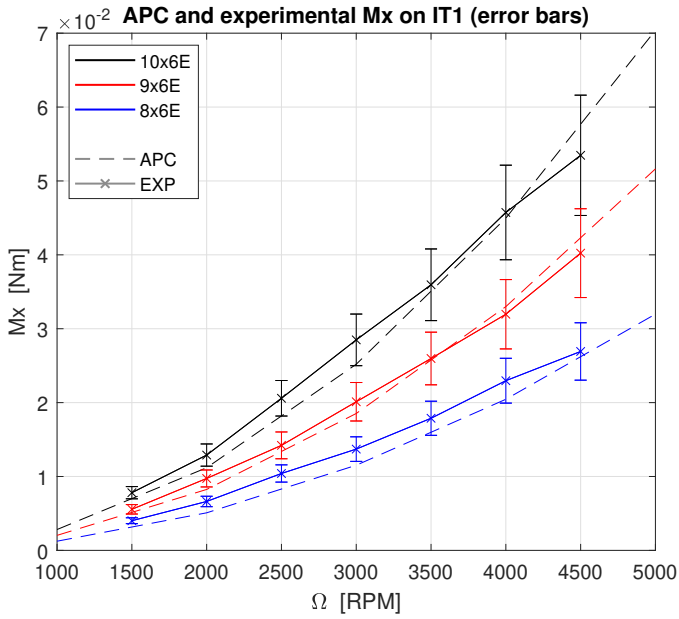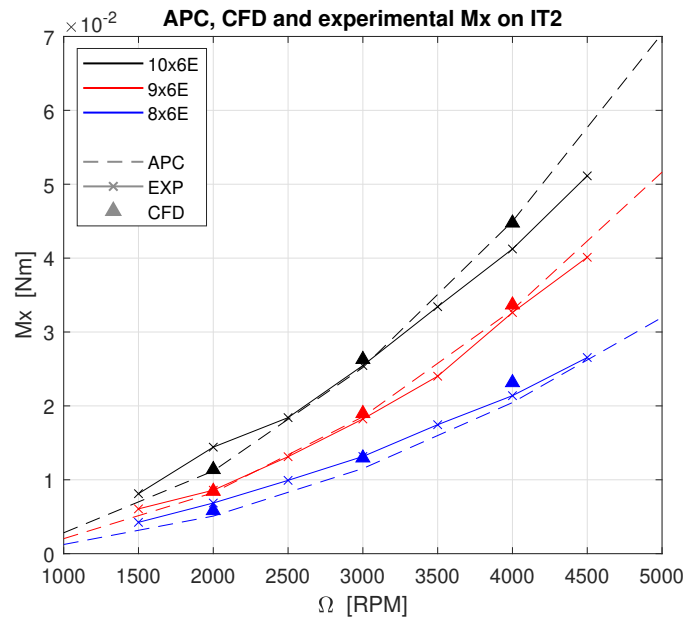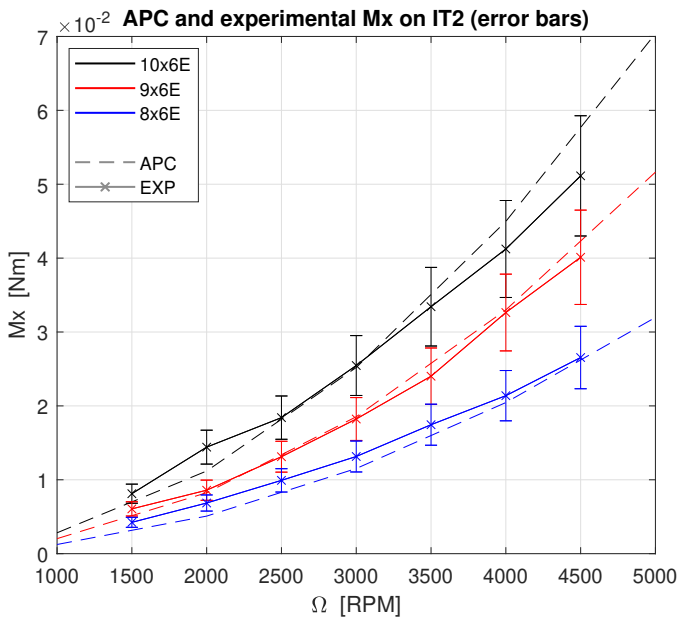

Figure 3.10: APC, CFD and computed experimental values for torque (M_x) as function of Ω for the selected propellers on IT2

For IT2, the torque curves are similar to those obtained with IT1. The uncertainty is slightly higher since the calibration only accounted for one axis. In order to assess the difference quantitatively, the mean relative error (MRE) is computed for each propeller. The mean relative error between the reference data (y_0) and the assessed data ($\hat{y}$) is the average of the relative error (RE) computed as in Equation 3.19 for the different tested speeds for a given propeller.

$$\text{RE} = \frac{|\hat{y} - y_0|}{y_0} \tag{3.19}$$

In Table 3.5 the MRE for thrust and torque obtained experimentally with IT1 for the selected propellers are presented, both for APC and CFD values taken as reference. It can be appreciated quantitatively how the experimental values are much closer to the CFD values than to those of APC regarding thrust, confirming that it is overpredicted by APC. About torque, the experimental values are also closer to the CFD values than to APC values, although the difference is not as large as for thrust.

Table 3.5: Mean relative error for thrust and torque on IT1 using both APC and CFD values as reference y_0

Propeller	APC y_0		CFD y_0	
	MRE F_x	MRE M_x	MRE F_x	MRE M_x
10×6E	15.95%	10.04%	1.23%	7.96%
9×6E	16.20%	9.91%	1.14%	8.82%
8×6E	17.14%	20.49%	5.12%	6.71%

Correspondingly, in Table 3.6 the MRE for torque obtained experimentally with IT2 are presented. The calibration coefficients obtained lead to similar values as for torque in IT1. It is concluded that the calibration procedure is satisfactory and that the test bench is reliable enough.

Table 3.6: Mean relative error for torque on IT2 using both APC and CFD values as reference y_0

Propeller	MRE T_x (APC y_0)	MRE T_x (CFD y_0)
10×6E	12.75%	12.54%
9×6E	5.86%	5.63%
8×6E	17.84%	8.90%

Lastly, the Figures of Merit (FM) for the isolated propellers are presented in Figure 3.11. The FM are computed as in Equation 2.17, where the ideal power is obtained by Equation 2.10 with the corresponding thrust value and considering that the air density is $\rho = 1.225 \ \text{kg/m}^3$, and the actual power is considered to be the mechanical power computed as $P_{\text{mech}} = \Omega M_x$.
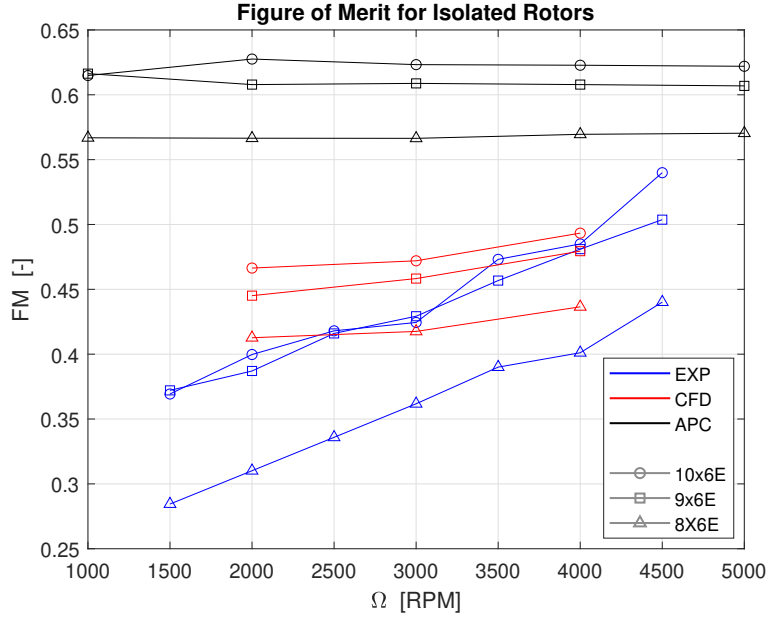
Figure 3.11: Figure of Merit (FM) for isolated propellers APC 10×6E, 9×6E and 8×6E with experimental (IT1), APC and CFD data

The highest FM values are obtained for APC 10×6E and the lowest for 8×6E (the area reduction for the smallest propeller does not make up for the thrust and torque reductions, so the computed ideal power is smaller in proportion to the actual power for smaller propellers than for bigger propellers for the studied cases). It can be noticed that the APC FM values are considerably higher than those obtained with experimental and CFD values. This could be anticipated since the thrust was overpredicted and the torque slightly underpredicted by the manufacturer APC. Also, the APC thrust and torque values (and the consequent ideal and actual powers) result in FM values that remain quite constant with the Ω increase. The FM values for the CFD and experimental data show an increasing trend with Ω (more noticeable for the experimental FM values), and the CFD FM values are higher than those obtained experimentally, especially for lower rotation speeds Ω.

3.2   Test Plan

There are many variables that may influence the performance of a tandem rotor configuration such as the rotor direction of rotation and rotation speed, the number of propeller on each rotor plane (one or two), the pitch of the blades, the rotor diameter, the rotor solidity, the rotor-plane distance h, the interaxial distance d, the flight condition (hover, climb, forward flight etc.). Due to the magnitude of the work, the parametric study of the number of propellers on each rotor plane, the rotor solidity, the flight condition, the pitch and the direction of rotation were left out.

As mentioned, the direction of rotation is also kept the same for all propellers. This decision is motivated by the fact that as the interaxial distance d increases, the initially beneficial increase in the flow velocity experienced by the downstream rotor blades when the rotors have opposing rotation directions

seems to lessen or even become detrimental as some regions of the blades experience very low or null velocities (as stated in [4]). This is an opportunity to explore this area since it is unconventional in practice, as several rotors with the same direction of rotation could not achieve torque balance (although for a drone with alternating directions of rotation in the repeated sets of propellers mounted on its several arms, global torque balance can be accomplished).

The parameters under study are then:

- Front (or upstream) rotor diameter

- Back (or downstream) rotor diameter

- Interplanar distance h

- Interaxial distance d

- Front rotor speed Ω_F

- Back rotor speed Ω_B

Thus, the tests consist in setting different combinations of h and d distances between the front rotor plane with one propeller and the back rotor plane with two propellers (all of them with two blades and the same pitch, but variable diameter between the front rotor and the back rotors), for different combinations of rotation speeds and in hover condition.

3.2.1   Selected Propellers

The selected propeller manufacturer was APC [13] since it provides data files with the geometric information about their propellers (not directly 3D CADs), so 3D CADs for the propellers can be modelled after them for the computational part of the study. The selected pitch for the study was 6 inches/revolution (intermediate pitch among the availables in the market). The chosen diameters were 8, 9 and 10 inches since bigger propellers produce a higher torque and the BLDC electric motors can experience overheating or even fail at high speeds due to the overload. Also for the latter reason and to continue with the work of former students, propellers with two blades were selected (propellers of the APC Electric family). APC uses the standard notation diameter×pitch, with the design rotation direction being noted by E or EP (meaning counterclockwise (CCW) or clockwise (CW) rotation respectively). Thus, the propellers are APC 10×6E, 9×6E and 8×6E.

Figure 3.12: APC 10×6E, 9×6E and 8×6E

3.2.2 Propeller Diameter Combinations

As mentioned earlier, only the configurations with a single front rotor and two back rotors are to be studied (with equal back rotors). All the possible latter diameter configurations with the selected propellers (subsection 3.2.1) are displayed in Table 3.13. Due to the amount of time that a combination of propellers takes to measure completely, the range of study was reduced to those cases in which the front rotor is bigger or equal in size as the back rotors (upper right triangular matrix in Figure 3.13). The diameter combinations tested experimentally are presented in Table 3.7:

Table 3.7: Propeller configurations tested experimentally

Front Rotor	Back Rotor
10×6E	10×6E
	9×6E
	8×6E
9×6E	9×6E
	8×6E
8×6E	8×6E
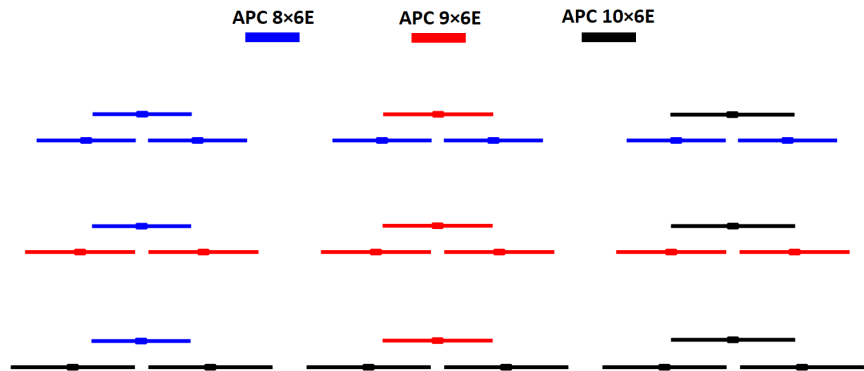
Figure 3.13: All possible configurations for a single front rotor and two back rotors with the selected propellers

3.2.3 Interplanar Distances

The interplanar separation h is the distance between the rotor planes. Three distances were tested: [90, 150, 210] mm.

3.2.4 Interaxial Distances

The interaxial separation d is defined as the distance between the front rotor axis and one of the back rotor axes. Four distance were tested: [140, 160, 180, 210] mm.

3.2.5 Rotation Speeds

The study with the rotation speed comprises the range between 2000 and 4000 RPM, with increments of 1000 RPM. The lower limit is established at 2000 RPM since the thrust and torque generated (especially in 8×6E) are quite small and better experimental results are expected for higher values to measure. The upper limit is established at 4000 RPM owing to the durability of the motors, since they were approaching the maximum load regime for higher speeds when the biggest propeller (10×6E) was mounted. For every combination of propellers in subsection 3.2.2 and every combination of distances in subsection 3.2.3, nine rotation speed combinations were tested:

Table 3.8: Rotation speed combinations to test

Front Rotor Ω [RPM]	Back Rotor Ω [RPM]
	2000
2000	3000
	4000
	2000
3000	3000
	4000
	2000
4000	3000
	4000

Chapter 4

Computational Fluid Dynamics (CFD) Approach and Methodology

4.1 Introduction to CFD

Computational fluid dynamics (CFD) simulations consist in solving a physical problem on a control volume numerically. The finite volume method [14] is applied, which entails the discretization of the control volume (now computational volume) into smaller elements and the discretization of time into time steps. The discretized governing fluid equations are solved on each of these elements and the solution is propagated every time step. The main discretized governing equations solved in most of CFD problems are five for a three dimensional case: conservation of mass (one), conservation of momentum (three) and energy (one) [14]. The fundamentals of CFD along with the methodology followed to asses the study of the rotor interaction problem with the chosen CFD software Simcenter STAR-CCM+ [15] are presented in this section.

4.2 3D Modelling of the Propellers

Since a computational study is to be carried out, the differences with respect to the experimental study should be aimed to be as little as possible. In CFD, the quality of the computer-aided design (CAD) models and the resemblance between them and the physical objects could be an important source or error. For that reason it is important to model the propellers with the highest degree of similarity to the real APC propellers. Fortunately, the company issues enough data for good 3D CADs to be built.

4.2.1 APC Propeller Datasheet

The company APC provides for the datasheets of their propellers if requested. The datasheets contain several data regarding the inertial properties, natural frequencies at certain speeds and geometric information about the propellers. The most relevant section in the datasheet for the sake of 3D CAD

34

building is the Airfoil Data Section, which contains the previously mentioned geometric info. In said section, it is stated which airfoils are used in the design of the blades (including the spanwise transition distances between them) as well as geometric data about the several airfoil sections that are defined in the spanwise direction. From this geometric data, it is possible to apply the required transformations to the base airfoils so that the sections meet their specific design in terms of shape and position. The geometric parameters that are relevant for the obtention of each airfoil are:

- **Station** The spanwise (lateral axis or Y axis in Figure 4.6) location of the sections, in inches.

- **Chord** The chord of the sections, in inches.

- **Pitch** The pitch angle formed by the chord, in inches/revolution.

- **Sweep** Position in the longitudinal coordinate (X axis in Figure 4.6) of the most advanced point in the airfoil section, in inches.

- **Thickness ratio** Nondimensional coefficient that relates maximum thickness of the airfoil section (not the base airfoils but the true airfoil sections of the propeller) and its chord.

- **Twist** Angle formed by the chord of the section defined from the leading edge (LE) to the trailing edge (TE), in degrees.

- **Maximum thickness** Maximum thickness of the airfoil section, in inches.

- **Z high** Position of the highest point in the airfoil section in the vertical coordinate (Z axis in Figure 4.6), in inches.

Also, the base airfoils used along the blade are indicated. For most of the APC electric propeller family, there is two of them (Figure 4.1): E63 and NACA 4412 (also referred to as APC12).

(a) E63 airfoil   (b) NACA 4412 airfoil
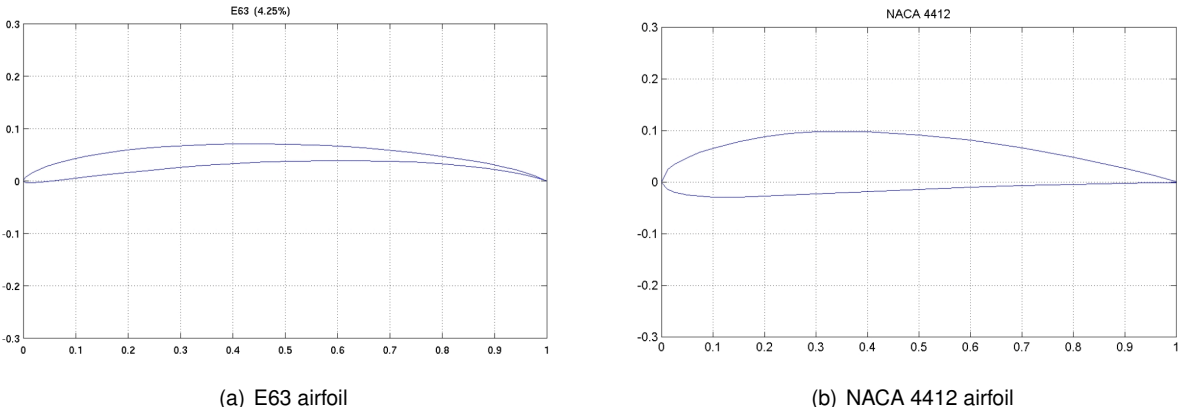
Figure 4.1: E63 and NACA 4412 airfoils [16]

In the datasheet the several segments of the blade are also indicated (their proportion varies between propellers). From the propeller hub to the first section, there is no data. From the first section to the transition start span, the base airfoil is E63. From the transition start span to the transition end span, the

base airfoil is not E63 nor NACA 4412, but a pondered blend between both of them. Finally, from the transition end span to the final span the base airfoil is NACA 4412.

4.2.2 Airfoil Profiles

With the previous data it is possible to obtain the coordinates of the points that shape the several airfoils of the blade. With the coordinates of the airfoil section points, accurate CADs can be modelled. A Matlab script that runs all the necessary steps for that conversion has been developed. It exports the several airfoil section coordinates, LE and TE coordinates and allows for a previsualization of the selected available propeller in the database.

The first step is to obtain the E63 and NACA 4412 profiles. Their coordinates were downloaded from the UIUC Airfoil Coordinate Database [16] in a discrete point coordinate format, the Standard *.dat format. The chord is normalized to the unit with the LE on the origin, and the order goes from the upper surface TE to the lower surface TE in counterclockwise direction as Figure 4.2 shows.
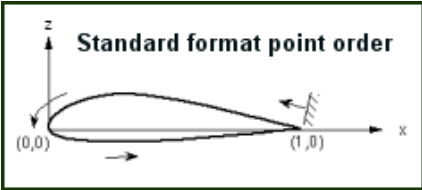
Figure 4.2: Standard format point order [16]

Since the two profiles do not have the same X axis coordinates, new points are created (at the Y position given by the slope between the previously existing points and the X position to add) in each profile until both of them have the same points. Then, a much higher point density is achieved by adding a lot of points along the profile so that the maximum thicknesses of the profiles can be found (Figure 4.3). The thickness ratios for the E63 and NACA 4412 profiles are 0.0427 and 0.1191 respectively.
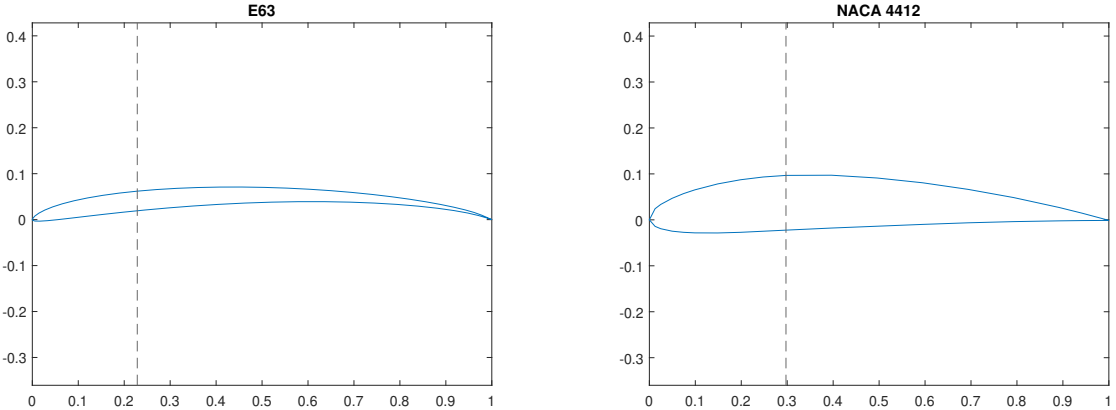
(a) E63 airfoil and maximum thickness location

(b) NACA 4412 airfoil and maximum thickness location

Figure 4.3: E63 and NACA 4412 airfoils along with their maximum thickness location

36

The next task is to obtain the transition profiles for the transition segment of the span. For that, the Y coordinates of the transition profiles fall between the Y coordinates of the original profiles E63 and NACA 4412. For example, if a transition profile is located at the 35% of the transition segment, the Y coordinates of the profile points will be 35% between the first airfoil and the second. As an example, the APC 10×5.5MR has 15 airfoil sections located in the transition segment of the span. The example calculated transition profiles are shown in Figure 4.4.
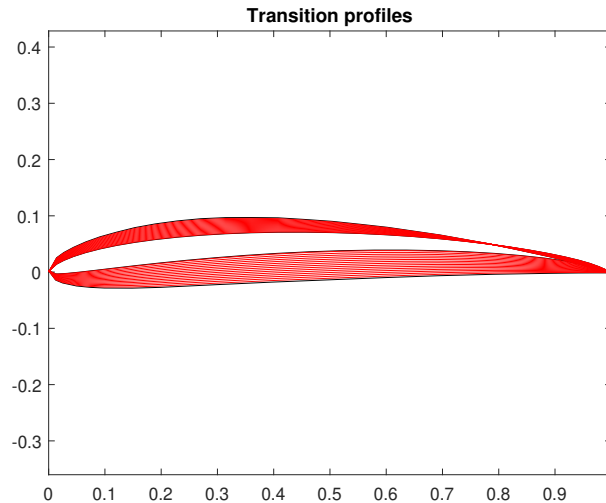
Figure 4.4: Normalized transition profiles (red) alongside the base airfoils (black) for propeller APC 10×5.5MR

The maximum thickness and consequently the thickness ratio of all of these transition profiles also needs to be found, as it will be mandatory for the correct scaling of the true propeller airfoil sections. With all of this data, the operations applied to the base and transition airfoils are:

- **Chord scaling** Since the base and transition profiles are normalized, the chord scaling is achieved by multiplying the X coordinates of the base or transition profile by the chord of the true airfoil section given by APC.

- **Thickness scaling** APC provides the thickness ratio of the final airfoil sections for their propellers. Since the Z coordinates of the base and thickness profiles already correspond to their original thickness ratio (which is different from that of the final airfoil section), a thickness scaling factor can be obtained as:

$$\text{Thickness factor} = \frac{\text{APC thickness ratio}}{\text{Original thickness ratio}} \qquad (4.1)$$

The Z coordinates of the base or transition profile are scaled by multiplying them by the thickness scaling factor and by the chord (to keep the proportion since the X coordinates were already scaled by the chord).

- **Airfoil rotation** The scaled airfoil is now rotated by applying a 2D rotation centered at the TE to all

37

the points of the profile, in counterclockwise direction. The angle of rotation is the twist given by APC (since it is already in degrees and the pitch is in inches/revolution).

- **Sweep translation** The X coordinates of the scaled and rotated airfoil undergo a translation so that the most advanced point of the profile after the rotation (in most cases still the LE) matches the X coordinate that the sweep parameter given by APC indicates.

- **Height translation** The Z coordinates of the scaled and rotated airfoil undergo a translation so that the highest point of the profile after the rotation (in most cases still the LE) matches the Z coordinate that the Z high parameter given by APC indicates.

- **Span coordinate addition** The span coordinate (Y axis) is added to the points of the profile making them three dimensional, according to the station APC parameter.

As a way to check the validity of the computed profiles, their maximum thickness after the scaling can be compared to the maximum thickness given by APC (Figure 4.5).
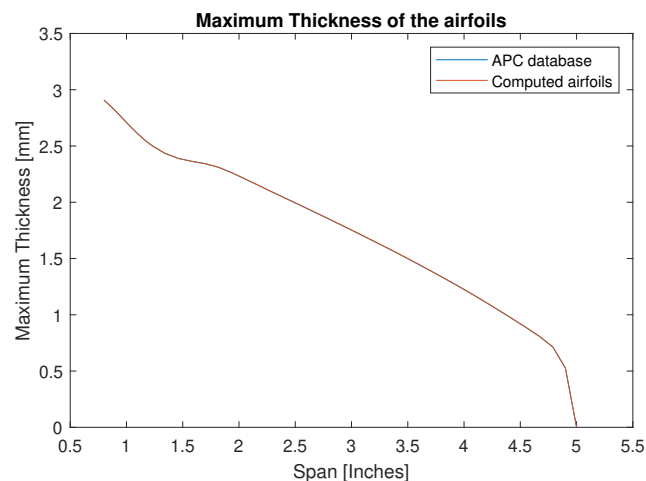
Figure 4.5: Maximum thickness of the computed sections vs maximum thickness of the true APC sections [13] for propeller APC 10×5.5MR

According to the company, the propeller hub section (located at the origin in the spanwise direction) can be modelled as an ellipse. The major and minor semiaxes for each propeller can be found in APC webpage [13]. The LE and TE points of the several airfoils and the propeller hub can be joined to obtain the LE and TE lines. As an example, the visualization of the APC 10×5.5MR sections is shown in Figure 4.6:
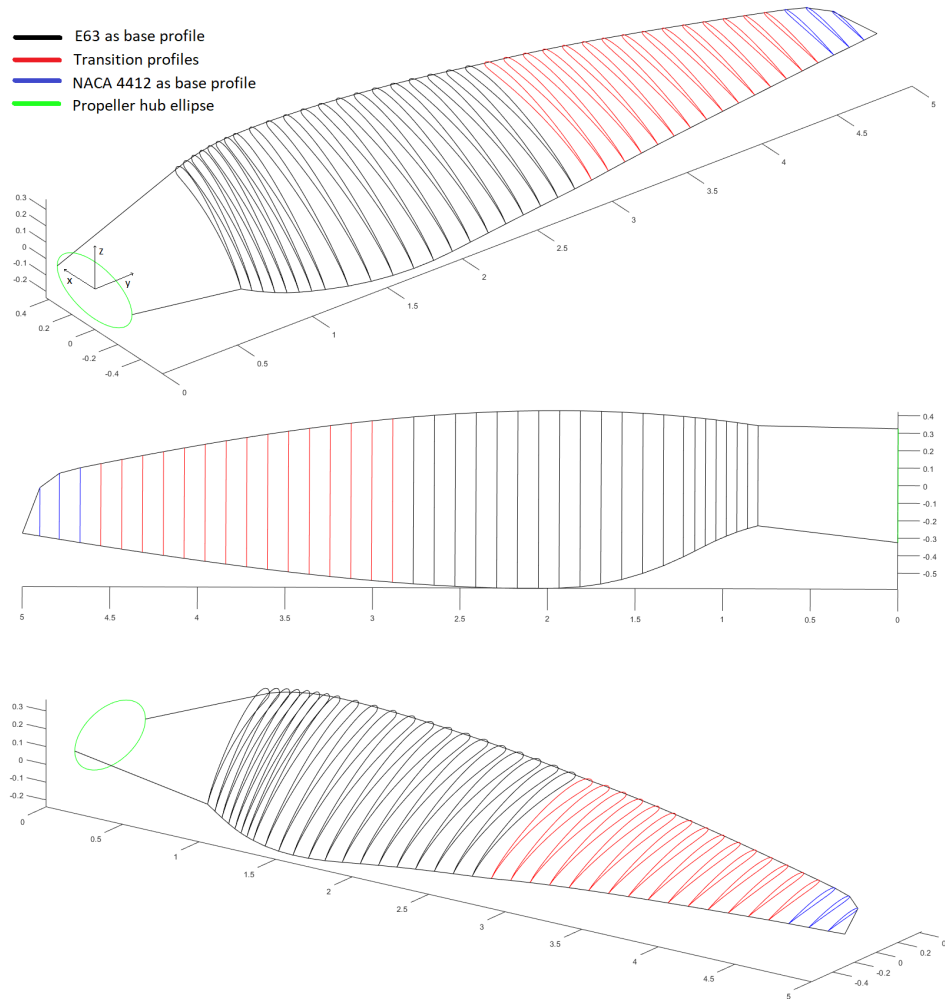
Figure 4.6: Airfoil sections along with LE and TE lines for propeller APC 10×5.5MR

Every intrados and extrados lines for the airfoils, along with the LE and TE lines are exported as *.csv files to be imported into the CAD software.

4.2.3   CAD Modelling of the Propellers

The software selected to build the 3D CADs of the propellers was Solidworks [17] (due to license availability and better performance in creating smooth lofted curved surfaces in comparison to other softwares like Autodesk Fusion360 [18]). In first place, the intrados and extrados curves for the airfoils, as well as the LE and TE lines are imported. Then, two lofted surfaces are created (intrados and extrados surfaces). These will go through the airfoil intrados and extrados imported lines and will use the LE and TE as guidelines or rails (note that not all of the sections given by APC are used, due to the overload of the loft tool when creating a surface that goes through too many selected lines). Another loft (this time a volume loft) is created from the ellipse section in the hub to the first airfoil, using the LE and TE lines as rails again. Finally, the hub is built by sketching a circumference with radius equal to the major semiaxis of the ellipse section, and extruding it a distance equal to the minor semiaxis of the ellipse section in both directions, creating a cylinder. The opposite blade is created using the circular pattern tool at 180°

around the Z axis and ultimately, a fillet of radius 0.5 mm (measured on real propellers) is added to the top hub surface. The CAD building procedure and final result for the propeller APC 10×6E is shown in Figure 4.7. The TE remains sharp and the transition between the design airfoils along the span is well captured.
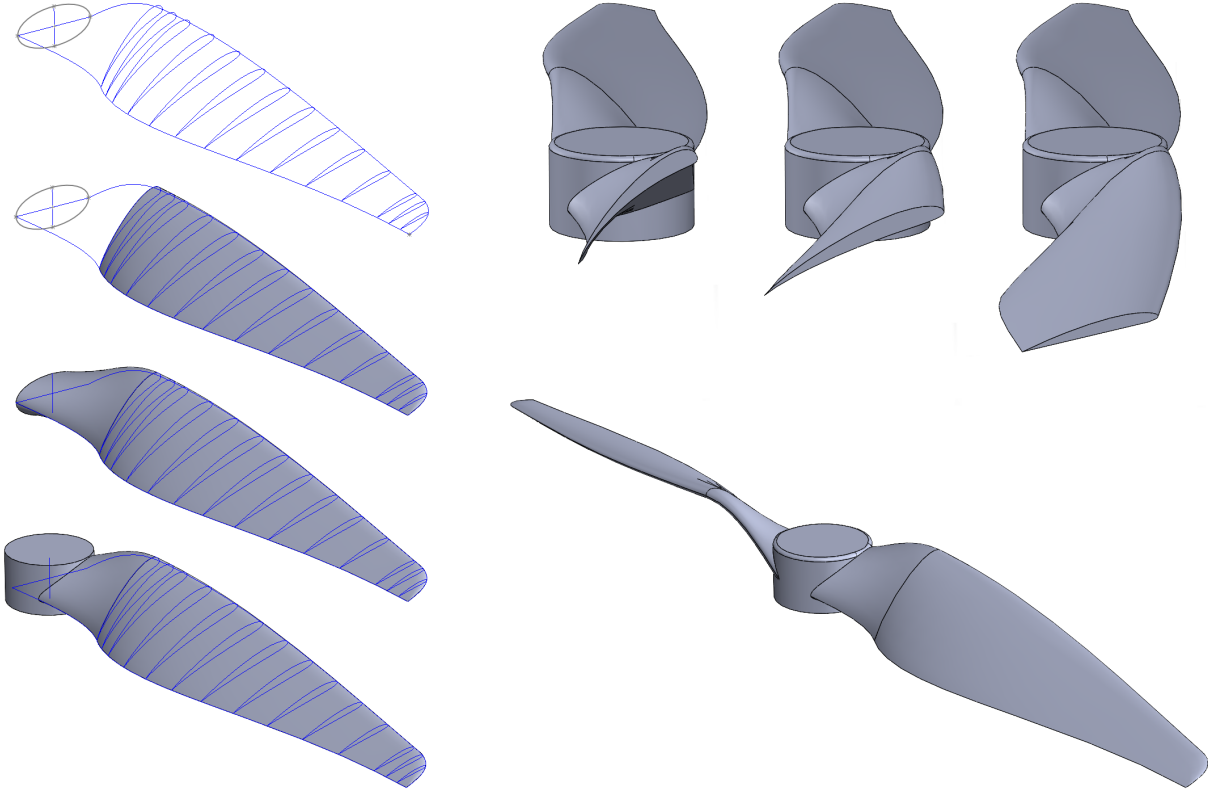
Figure 4.7: APC 10×6E CAD procedure and final result

The APC 10×6E, 9×6E and 8×6E are modelled following this procedure (Figure 4.8). The 3D CADs are then exported in STEP AP214 (*.step) format since the chosen CFD software Simcenter STAR-CCM+ [15] will not recognize the individual surfaces otherwise, and with an elevated tessellation density to represent them faithfully (the tessellation process is the covering of a surface with flat regular polygons so that the information of the surface is stored as vertex coordinates). At this point, the 3D CADs are ready to be imported into the CFD environment.
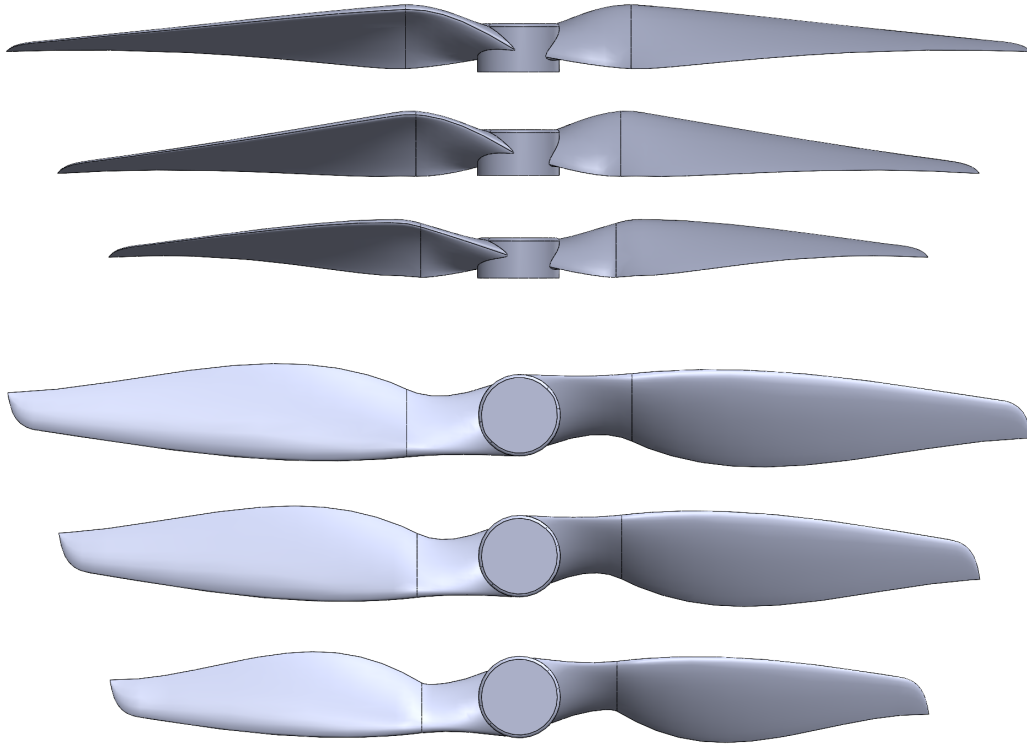
Figure 4.8: APC 10×6E, 9×6E and 8×6E 3D CADs

4.3   Available CFD Approaches for Rotating Bodies

When performing a CFD study on a rotating body such as a propeller, there are three main approaches that could be followed to account for the motion during the simulations. These are the Moving Reference Frame (MRF) approach, the Rotating Mesh approach and Overset Mesh approach [19]. The overset mesh approach is a variation of the conventional rotating mesh (or sliding mesh) approach, while the MRF approach has different foundations and applications.

4.3.1   Moving Reference Frame

The MRF approach is also referred to as the frozen rotor approach [20], since the mesh around the rotating body remains static. In reality, there is not a motion of the body (or the mesh around it), but it is the flow surrounding it which accounts for the rotation. A velocity source term is imposed to the flow, by which every cell of the MRF doamain would be experiencing a velocity that depends on the rotation speed of the body and the distance of each cell to the rotating body reference frame origin. More precisely, this rotation source term corresponds to the centrifugal and coriolis terms in the Navier-Stokes equations that are solved on the domain, when these are derived for a reference frame that rotates with the propeller [19].

It is important to remark that the MRF method can only be applied to steady simulations, since it accounts for the final state of the flow that goes around the static body [20] [19] (as a time averaged

solution). This means that no transient effects can be captured nor the interactions of the rotating body with surrounding elements over time. However, as simple and coarse as it may seem, not only can the MRF technique be precise enough when applied to some cases of study but it can even be more suitable in certain situations due to its very low computational cost. For most of the engineering studies that involve an isolated rotor in hover or axial climb conditions, knowing the full time varying flow field is not necessary, since it becomes cyclic after a certain number or rotations. Using MRF in those cases demands much less computational power, which saves a lot of computation time (it can get up to an order of magnitude lower than with rotating mesh alternatives [20]). That is why it is usually applied to fans, pumps or wheels and also it is usually used as a first run approximation to obtain an initialization of the flow field in rotating mesh simulation [19].
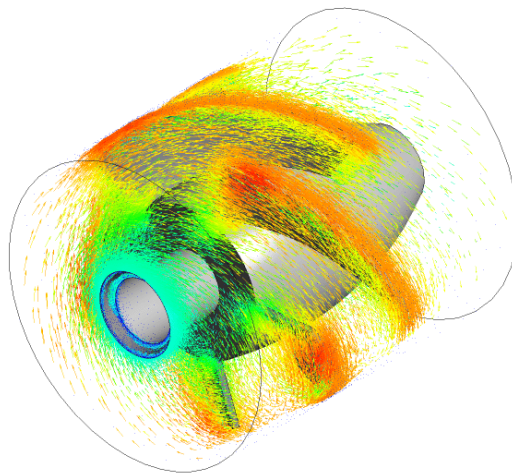
Figure 4.9: Example of application of the MRF approach on a turbine and the resulting vector velocity field representation around it [21]

4.3.2 Rotating Mesh

The rotating or sliding mesh approach is said to be theoretically the most accurate method for the simulation of rotating flows [19]. Not only does it grant more precision, but it is necessary for obtaining transient solutions in unsteady simulations. However, the rotating mesh approach is much more demanding in computational terms [20] and has a higher degree of difficulty in its implementation regarding the suitability of the mesh as it will be explained.

In the rotating mesh approach, there are two types of meshes in the computational domain: the stationary or static mesh and the rotating mesh that encloses the rotating body. The former does not experience any motion, meanwhile the latter is subjected to a rigid body motion. Both meshes do not overlap in space but should be neighbouring, and they are connected through an interface (which means that the adjacent cells can exchange information). The two mesh grids will slide relative to one another as the rotating mesh moves according to its rotation rate at the beginning of each time step. In comparison to MRF method, this implies simulating the real nature of the motion and can capture all of the

interaction effects with total fidelity, although it entails a series of requirements regarding the time step and the interface and mesh quality. To start with, the cell size of those cells that are in contact with the interface should be similar from both sides, since the meshes are detached and the faces of cells do not coincide completely as Figure 4.10 shows.
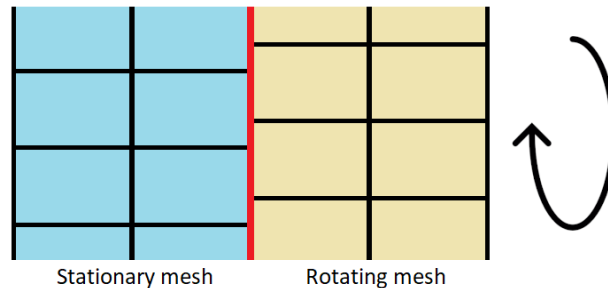
Figure 4.10: Non-conformal interface between the stationary and rotating meshes

Since the two meshes are built separately they are non-conformal, and when a cell surface on the interface is in contact with two or more cell surfaces simultaneously the software has to interpolate the solution. This is why cells on the interface should be of similar size to avoid situations where a big cell surface is in contact with many small cell surfaces since it leads to worse results [19]. Additionally, for the correct transmission of information between cells, the time step should be very small. Not only is this important for a reliable propagation of the solution, but also it can make the simulation diverge if the time step is too large [22] as it will be explained. This requirement along with the need to update the mesh position every time step make the rotating mesh approach more time consuming in computational terms, and this limitations will be discussed in subsection 4.6.4.

The rotating mesh approach is the chosen method for the study due to its capability to account for several rotating regions even at different rotations speeds with accuracy (unlike MRF), and because in general it provides for more precise results than the overset mesh approach and is slightly faster [23] (since the interface boundaries do not need to be updated every time step).

4.3.3   Overset Mesh

The overset mesh method (also referred to as the chimera grid method [19]) can be applied to a wider range of cases of study than the sliding mesh due to the capability of the interface (more precisely the overlap region) to dynamically change during the simulation. This is specially useful when large relative motions between the components of the simulation are involved (cases in which the conventional rotating meshes surrounding the bodies would periodically collide with other elements of the simulation, or for the analysis of translation motions where the mesh surrounding the moving body would collide with the stationary mesh).

When using the overset mesh approach, there are two kind of meshes: the background mesh and

the overset meshes. The background mesh is analogue to the stationary mesh used in the rotating mesh approach, but it encompasses all of the computational volume (the stationary mesh needs gaps where the rotating meshes are placed). The overset meshes, on the other hand, are comparable to the rotating meshes themselves. They are applied a rigid body motion and surround the moving body. Their outer surface must be defined as an overset boundary, and the overset mesh is always overlapped with the background mesh. The mechanism that makes the overset special lies in the capability of certain background and overset mesh cells to remain inactive (areas with inactive cells are usually called holes) so that only some layers of cells close to the overset boundary remain overlapped in practice and participate in the exchange of information between the two kinds of meshes. In Figure 4.11 the overset mesh scheme is shown (in this case, the background mesh is referred to as the major grid, and the overset mesh as the minor grid).
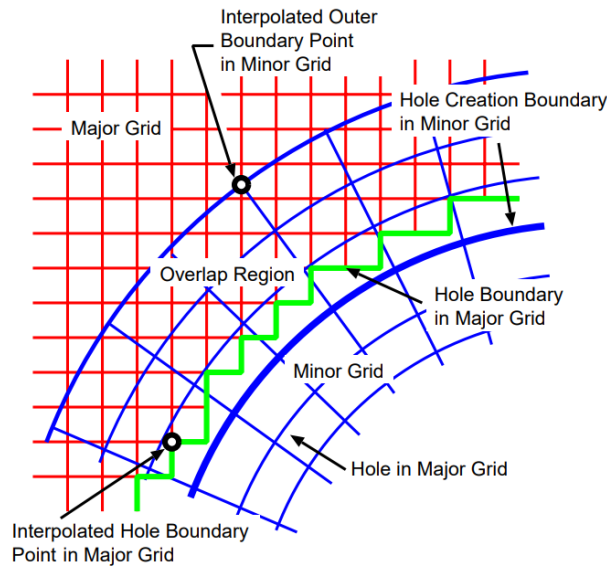
Figure 4.11: Overset mesh scheme [24]

4.4 Simulation Parameters

4.4.1 Spatial and Temporal Discretization

When a physical problem is approached numerically, it is discretized both in space and time. When certain partial differential equations are involved (as in most of fluid dynamics problems), the convergence of the simulation is not guaranteed. The Courant–Friedrichs–Lewy (or CFL) condition expresses that the information travelling within a time step along the mesh must be lower than the distance between cells, or that the information from a given cell should only propagate to its immediate neighbors so that the occurring phenomenons are captured. Mathematically, it is expressed as [22]:

$$C = u\frac{\Delta t}{\Delta x}$$ (4.2)

Where where C is Courant number, u is the magnitude of the velocity, Δt is time step size and Δx is the size of the smallest cell of the domain. To ensure stability C should be lower than 1 [22], meaning that for a very fine mesh the time step should be chosen accordingly. The required mesh resolution for the present problem is found in subsection 4.6.3 through a mesh independence study. However, for unsteady simulations that need to be carried out for long periods of time (as it is the case), larger time steps that yield C numbers above 1 can be used if they are proved to be small enough for the simulation requirements [25] (subsection 4.6.4).

It is important to state which discretization schemes in particular are used for the solution propagation. The temporal and spatial discretiszation schemes appear in Table 4.1.

Table 4.1: Discretization schemes used in the simulations

Discretization	Method	Order
Temporal	Implicit	1st
Spatial	Upwind	2nd

4.4.2 Coupled and Segregated Flow Solvers

In CFD there are two main approaches to solve the governing discretized equations, referred to as coupled flow and segregated flow solvers. The coupled flow (or density based) solver approach is suitable for high-speed compressible flows while the segregated flow (or pressure based) solver is used in low-speed incompressible flows [26]. In both methods the velocity field is obtained with the momentum equations and the main difference lies in the obtaining of the pressure field: in the density based solver the density field is obtained through the continuity equation and the pressures are derived from the equation of state (pressure coupled with density and hence with velocity), while in the segregated or pressure based solver the pressure field is given by a pressure equation or, in other words, the pressure field is decoupled from the velocity field (only acceptable for incompressible flows, which are under $Ma = 0.3$ for air [14]). Also, segregated solvers are more stable and can reach convergence faster [26]. Since the maximum speed expected is of the order of the largest propeller tip velocity, 53.2 $\mathrm{m/s}$ on APC 10×6E at 4000 RPM ($Ma = 0.16$), the segregated flow solver is chosen, along with the ideal gas model.

4.4.3 Turbulence Models

Turbulent flow is a flow regime present in most of situations. Unlike laminar flow, turbulent flow has rotational components in three dimensions, its chaotic and carries more energy [27]. The structures formed by the turbulent flow are called eddies, and the larger ones dissipate the flow energy into smaller scale eddies, until by viscosity action they vanish. The turbulence of the flow is relevant for the prediction of the drag force specially [27], and there are several approaches to model it:

- **Direct Numerical Simulations (DNS)** The turbulence is explicitly resolved and not modelled in any way. The high fidelity flow is the consequence of solving the discretized equations with spatial

and temporal scales small enough that are able to capture any scale of turbulence. DNS are incredibly demanding in computational terms and are usually used as validation tools [28].

- **Reynolds-averaged Navier-Stokes (RANS)** The Navier-Stokes equations, from which momentum conservation is derived, can have the velocity decomposed in a mean value term (independent of time) and a fluctuation velocity term as $u(x,t) = \bar{u}(x) + u'(x,t)$ [29]. The derivation of this formulation leads to the Navier-Stokes equations to be almost the same except for all its velocity terms being averaged and having an additional term. The resulting RANS equations for a stationary flow of an incompressible Newtonian fluid in Einstein notation can be expressed as [29]:

$$\rho \bar{u}_j \frac{\partial \bar{u}_i}{\partial x_j} = \rho \bar{f}_i + \frac{\partial}{\partial x_j} \left[-\bar{p}\delta_{ij} + \mu \left(\frac{\partial \bar{u}_i}{\partial x_j} + \frac{\partial \bar{u}_j}{\partial x_i} \right) \right] - \frac{\partial}{\partial x_j} \left(\rho \overline{u_i' u_j'} \right) \tag{4.3}$$

Where the new nonlinear extra term $\frac{\partial}{\partial x_j} \left(\rho \overline{u_i' u_j'} \right)$ accounts for the time average of the velocity fluctuations and is called apparent stress or Reynolds stress. In this way, the steady-state solution is decoupled from the time-varying fluctuations, although for the problem to be closed the Reynolds stress term needs to be modelled (all RANS models are based on the modelling of this term [29]).

- **Large Eddie Simulations (LES)** The smallest temporal and length scales are ignored through a low-pass filter and only the large scales are resolved. Similarly to RANS, the smallest scales are modelled statistically [28].
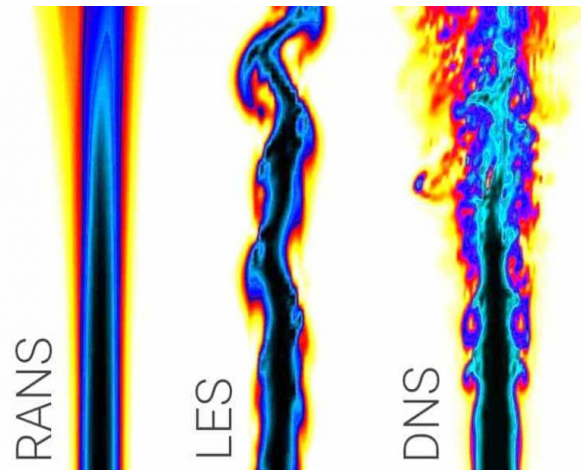
Figure 4.12: Jet modelled with RANS, LES and DNS turbulence approaches [30]

Figure 4.12 shows the turbulence of a jet solved with RANS, LES and DNS respectively. For the study, RANS turbulence models will be used since the computational cost of DNS and LES are too elevated for the available resources. There are several RANS models based on the modelling of the Reynolds stress term, that can be expressed as a function of the turbulent kinetic energy (TKE or k) $k = \frac{1}{2} \left(\overline{(u')^2} + \overline{(v')^2} + \overline{(w')^2} \right)$ [29]. The models solve the turbulent kinetic energy k coupled with equations for other turulence-related parameters. The coefficients for this models are obtained empirically. The most pupular RANS models are:

46

- **($k - \varepsilon$)** In this model the turbulent kinetic energy k and the turbulent dissipation ε (rate at which the velocity fluctuations dissipate) equations are solved. Performs worse for severe pressure gradients and separation, so it is more suitable for flows away from walls [31] (it is classified as a high Reynolds turbulence model).

- **($k - \omega$)** This model also solves two transport equations: k and the turbulent frequency or specific turbulent dissipation rate ω. It predicts better the flow close to the walls [27] (low Reynolds turbulence model).

There are other simpler models based only on one equation as Spalart-Allmaras. However, the chosen turbulence model is the SST $K - \omega$ (SST stands for shear stress transport). It is a modified $K - \omega$ model which combines original near wall prediction with that away from walls of $k - \varepsilon$ through blending functions [31], since the turbulence on the wake is also relevant for this study as it is the turbulence around the propeller.

4.4.4 Boundary Conditions

The typical boundary conditions that enclose the problem which are applied in this kind of analysis are the following [14]:

- **Velocity inlet** This condition establishes a velocity (in magnitude and direction) on the inlet boundary of the domain. It could be used to simulate different climb speeds by setting the velocity of the incoming flow, although for the hover condition it is set to null velocity.

- **Pressure outlet** A constant pressure is imposed on the outlet boundary, specifically the atmospheric pressure for this study (undisturbed). The inlet and outlet boundaries should be chosen accordingly to the general direction of the flow, since the mass flow is expected to be positive on the inlet and negative on the outlet.

- **Freestream** This condition is suitable for boundaries on which the flow direction could either be inward or outwards the computational volume.

- **Interface** This boundary condition can only be applied on surfaces which are shared by two regions. It connects both regions so that the solution can be propagated.

- **Wall** No-slip boundary condition applied on surfaces through which the fluid cannot flow. In this study it will be applied to the surface of the propellers.

4.5 Mesh Parameters

4.5.1 Computational Volume

The computational volume is to be meshed and divided into smaller volumes with connectivity between them (cells) so that the discretized governing equations are solved in each of them. As the

selected approach for the simulations in section 4.3 is the sliding mesh method, there will be two kinds of volumes: static and rotating.

The static volume should be big enough so that the flow in the region of interest is not affected by the imposed boundary conditions in the far-field. It is recommended that the domain is at least 15 times bigger than the characteristic length of the problem [32] (in this case, the rotor diameter) downstream. The downstream distance selected is 4 m, equivalent to 15.75 times the the biggest propeller diameter, APC 10×6E. As for the upstream direction, half of the downstream length is enough and can be shaped as a hemisphere instead of as a cylinder to reduce the total number of cells and reduce the computational cost. Also, it is intended that the cell density around the propeller (the rotating volume and its surroundings) is high enough to provide for the desired accuracy and resolution. That is why a mesh refinement is applied in a volume that encloses the rotating region, so that the cells of the static region inside it have a smaller size in comparison to the size they would have accordingly to the mesh controls (referring to the growth rate in subsection 4.5.3). The static region extends downstream for more than two times the height of the rotating region to capture the wake with more detail, and upstream it is shaped as an ellipsoid to reduce the amount of total cells while still capturing the greatest velocity and pressure gradients above the propeller.

As for the rotating volume, it needs to be modelled as a volume of revolution so that it is always in contact with the stationary volume. The chosen shape is a cylinder for simplicity. Its specific dimensions are discussed in subsection 4.6.2. A visualization of the computational volumes along with the boundary conditions described in subsection 4.4.4 and applied on the pertinent surfaces is presented in Figure 4.13.
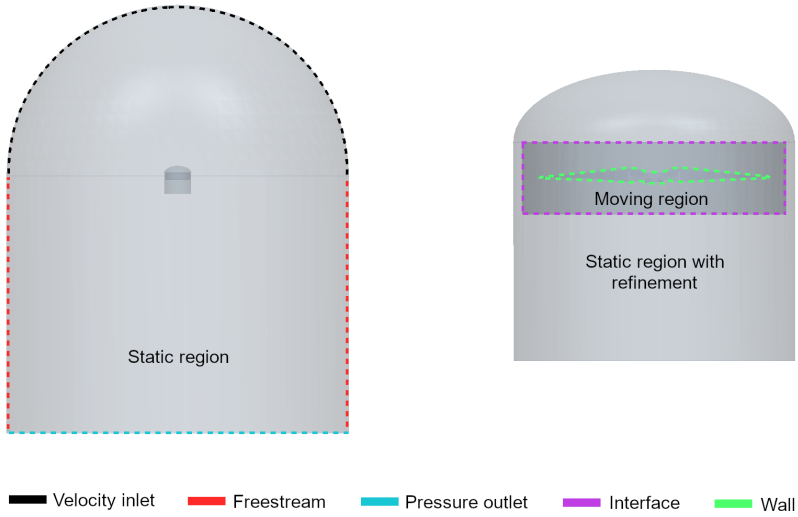

Figure 4.13: Different boundary condition types on the several computational domain surfaces

4.5.2 Element Type Selection

The element type with which the regions will be meshed also has an impact on the result and on the computational efficiency. The most efficient meshes are the so called structured meshes [33], constituted by topologically regular elements (often quadrilateral or hexahedral elements for 2D and 3D respectively) that have an implicit connectivity between elements. This implicit connectivity works like an indexing of elements, which allows for a fast identification of neighbours and speeds up the calculus. However, the appliance of these meshes to complex geometries require a high degree of manual intervention and expertise on the area [33] (and increases the mesh generation time remarkably, specially if several cases have to be set as in this study). For that reason, unstructured meshes are used for the study.

In the rotating region a polyhedral mesh is used since they usually capture more precisely the gradients due to the greater number of neighbours when interpolating [34]. Also, they seem to work better for flow structures in which there is not a specifically predominant direction of the flow (since the faces are oriented randomly and the centroids of the cells are not aligned in a specific direction). In general, they are better than hexahedral meshes [34]. However, to capture correctly the boundary layer on the propeller surface, the first layers of cells need to be meshed with prismatic layers [35] as explained in subsection 4.5.4.

The rest of the domain (static region) is meshed with an unstructured hexahedral mesh, by using the trimmer mesh tool in STAR-CCM+. Several tests with full polyhedral mesh (both in the rotating and static region) and with hexahedral mesh only on the static region were performed, and no difference was found in terms of convergence speed or thrust and torque values. However, the meshing time for the hexahedral mesh was faster than for the polyhedral and the computational time spent per iteration was lower too due to the less complex connectivity between cells. This is why the hexahedral mesh is chosen for the static region.

4.5.3 Mesh Controls

The size of the cells should gradually increase from the fine mesh regions to the outer areas of the domain (not of interest and with negligible changes) to save computational time. In order to control the relations between cell sizes in the different regions, all of them are expressed as a function of the global parameter $\mathrm{Base\,size}$. In this way, the proportions between cell sizes are maintained even when the global size of the mesh changes. It is important since the mesh controls such as the growth rate (maximum proportion at which cells can grow as they distance from a surface to guarantee a smooth transition, 1.05 inside the rotating region) or the target cell size at the refinement region are set so that the transition is smooth and the cell sizes at the interface are similar in size from both sides (Figure 4.14) to contribute to a correct propagation of the solution.
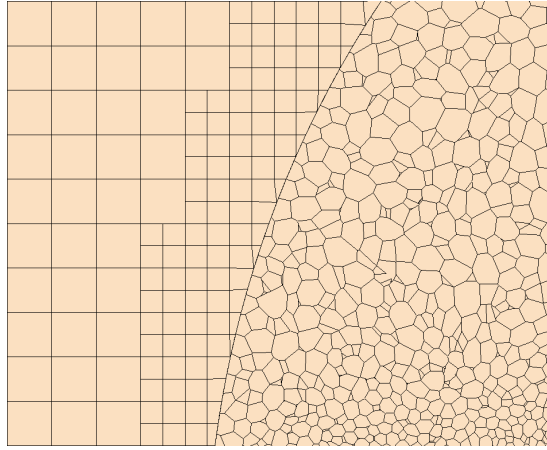
Figure 4.14: Upview cut of the interface between the rotating volume and the static volume

4.5.4 Non-dimensional Wall Distance Y+ and Prism Layer on the Propeller

The boundary layer appears on the surface of a body surrounded by fluid when on movement and encompasses the transition from static flow on the surface to the fully developed flow. One the formal definitions for the boundary layer width is that for which the 99% of the undisturbed flow velocity value is reached [36]. The abrupt velocity gradient in the boundary layer is responsible for great viscous force on the surfaces, and a correct prediction of the boundary layer is essential in a CFD study if the skin forces are to be estimated correctly [36].

As the flow inside the boundary layer is highly aligned, a conventional meshing around the propeller surface could induce errors when capturing the velocity gradients [35]. That is why prismatic layers are used around surfaces where a boundary layer is to be captured. All of the elements of the prismatic layer grow in height at the same rate so their centroids are aligned, and they are stretched in the direction of the flow. When capturing the boundary layer with prismatic layers, there are two main approaches [35]:

- **Wall functions approach** Since a lot of layers are required to have a good resolution of the velocity gradient and this is computationally expensive, empirically derived equations that describe (wall functions) it can be used to interpolate the gradient with a lower number of layers. They work well for flows with no separation and fail to predict it, and are meant to be used with high Reynolds turbulence models.

- **Viscous sublayer approach** The velocity gradient is fully captured in the boundary layer with enough resolution on the prismatic layers (more computationally expensive). It is meant to be used with low Reynolds turbulence models and separations can be captured. This is the approach that will be used for the simulations in the present work.

In Figure 4.15 (b) both approaches are illustrated. However, there are restrictions regarding the centroid (red dots) height of the first cell so that these models are valid. In reality, the boundary layer is subdivided in sublayers where the velocity has different behaviours: viscous sub-layer, buffer layer and
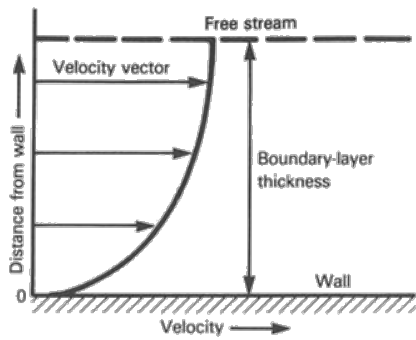
(a) Boundary layer scheme [36]
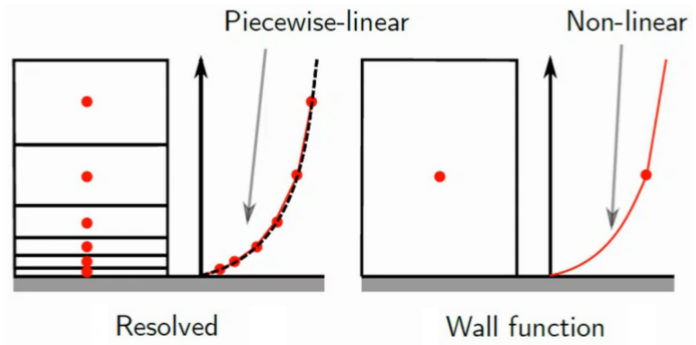
(b) Viscous sublayer and wall function approaches [37]

Figure 4.15: Boundary layer scheme and viscous sublayer and wall functions approaches to capture it

log-law region [35]. The centroid of the first cell should not be located in the buffer layer (transition region) for any of the approaches. In nondimensional terms, the buffer layer nondimensional wall distance Y+ range is 5 > Y+ > 30 [35]. This means that for the viscous sublayer approach the nondimensional wall distance Y+ of the first prismatic cells on the meshed surface should be Y+ < 5 and for the wall function approach it should be contained between 30 > Y+ > 300 for good gradient approximations [35].

As the viscous sublayer approach is chosen, the Y+ for the first prismatic cells should be below 5. The boundary layer is estimated to be around 0.85 mm thick for the average propeller chords used [38] and the flow velocity that the rotation speed range produces. A compromise between computational cost and precision is reached for 7 prismatic layers covering a total height of 0.83 mm with a prism layer stretching (rate of separation between cells with respect to the previous separation) of 1.5 which guarantees a Y+ range under 5 almost for the entirety of the propeller surface as shown in Figure 4.16.
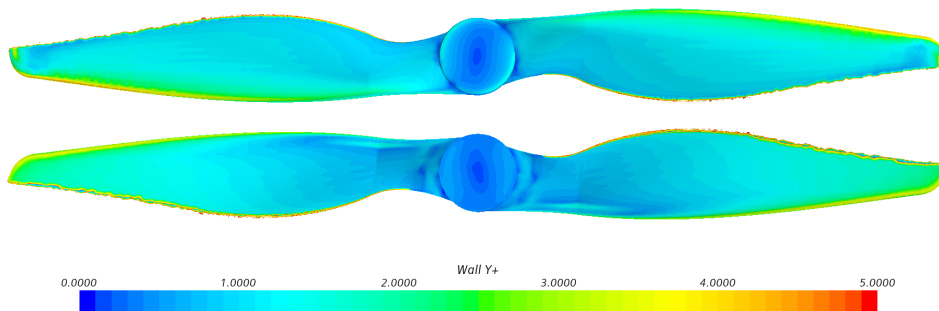

Figure 4.16: Y+ distribution on APC 10×6E propeller for the selected prismatic layer

The resulting prism layer around the propeller can be visualized around a blade section of the propeller by cutting the mesh laterally, as in Figure 4.17.

51

(a) Zoomed in mesh cut around the LE

(b) Zoomed out mesh cut
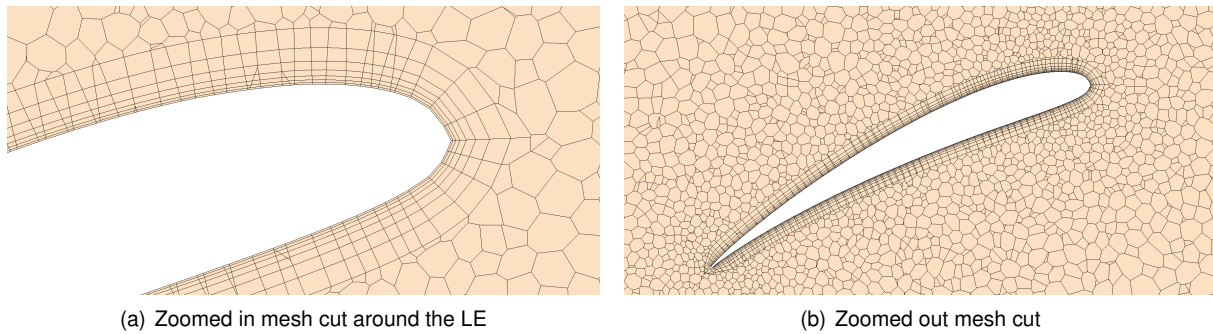
Figure 4.17: Side mesh cut around the profile at 20% of the span for an APC 10×6E propeller

4.6 Mesh Independence Study

4.6.1 Convergence Criteria

As these are unsteady simulations, there is no such thing as a converged final value for the magnitudes of interest (thrust and torque on the propellers) overtime. The calculus is initialized with a static flow field around the body, so as the body rotates and the flow develops, the pressure and friction forces on it keep changing (which does not mean their values are not realistic: it is the transient regime). However, this kind of simulation (propellers in hover or axial climb condition) can be considered to be somehow "steady" within the unsteady since they are expected to reach a final state in which thrust and torque are maintained overtime [39]. Thus, the running case is considered to have reached its final state when the average values of thrust and torque do not change overtime [39] (since they exhibit an oscillatory behavior due to the unsteady nature of the simulation). As an example, for the propeller APC 10×6E at 4000 RPM with the mesh and simulation parameters selected along this section this state is reached at around 0.055 s (about 4 rotations, even if the wake is not yet fully developed the flow structure around the propeller has reached its final state).

Nevertheless, as the flow conditions change overtime in unsteady simulations (in this case, due to the rotation of the propeller), the state of the flow at each time step is solved as if it was a steady simulation. This is, for every time step (entailing a rotation of the propeller and the moving mesh region), the final state of the flow for that particular "steady" flow is reached through several sub-iterations or inner iterations. For every time step, the solution may or may not be converged depending on the number of inner iterations. There are several indicators of convergence, although for complex unsteady cases, a common criteria to follow is performing the necessary sub-iterations until a drop of the residuals by 2 orders of magnitude (relative to the first sub-iteration) is achieved for each time step [32]. Residuals are the imbalances that appear when solving the governing fluid equations in each cell due to the numerical approach, so as more sub-iterations are performed, the better these equations are fulfilled. CFD softwares typically show the averaged residuals over the meshed regions for the following equations: continuity, X, Y and Z momentum, energy, and the turbulence transport equations (specific dissipation rate (SDR) and turbulent kinetic energy (TKE) if the $k - \omega$ model is selected). For the variety of cases

studied in which the mesh and simulation parameters selected along this section have been applied (time step equivalent to a 5° rotation), the 2 orders of magnitude drop for the mentioned residuals is achieved at 30 sub-iterations.

4.6.2 Effect of the Rotating Volume Dimensions

The size of the rotating volume that encloses the rotor should not be determinant for the result since the interface connects the two regions. However, as the interface is nonconformal, the connection of both regions involves the interpolation of the solution between cells since a single cell face could be adjacent to more than one neighbour cell faces. Also, the use of an interface can also impact the result if the rotation per time step Δ_t is too large, since the flow on one side of the interface could differ notably from that on the other side with respect to the previous time step [25] (this could even make the simulation diverge).

As stated before, the rotating region has to be shaped as a surface of revolution (in this particular case, a cylinder). Then, in order to reduce the reliance of the solution on the interface, the rotating cylinder should enclose not only the propeller but also the region where the greatest gradients in velocity take place. As for the cylinder radius, it was set to be always 2 cm greater than that of the propeller so specially the tip flow could develop enough in the radial direction inside the rotating volume. Increasing this gap did not lead to significant changes in the solution and it would restrict the minimum interaxial separation d in the three propeller simulations (since the rotating meshes would overlap). As for the axial direction, the rotating cylinder needed more separation from the propeller surface. The impact of the rotating region height (where the propeller is placed in the middle) is presented in Figure 4.18:

(a) Thrust versus rotating region height

(b) Torque versus rotating region height
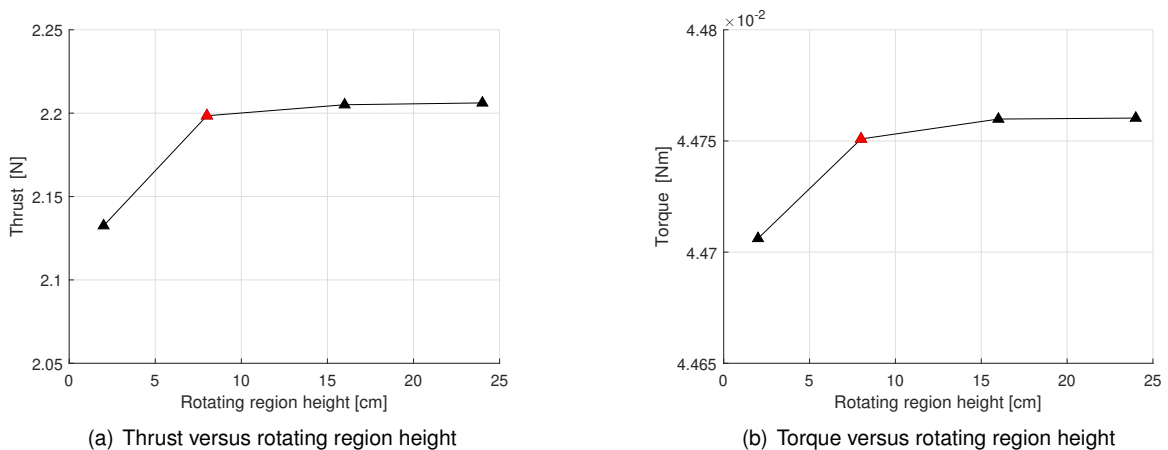
Figure 4.18: Effect of the rotating region heigh on thrust and torque for APC 10×6E at 4000 RPM

The rotating region height chosen is 8 cm (red marker in Figure 4.18) since that value does not restrict the interplanar separation between rotors h and the percentage variations in thrust and torque of the next proposed height with respect to the chosen one are under a 1% as Table 4.2 shows.

Table 4.2: Percentage variation for thrust (F_x) and torque (M_x) with respect to their previous iteration for APC 10×6E at 4000 RPM (rotating region height effect)

Height [cm]	F_x variation	M_x variation
2	–	–
8	3.00%	0.11%
16	0.29%	0.02%
24	0.05%	0.001%

4.6.3   Independence Study with Element Size

For the selected mesh control values and rotating region size defined previously, a mesh indepen-dence study with the element size is carried out. In the STAR-CCM+ environment, the target sizes for the elements in the different regions have been referenced to the global parameter $\mathrm{Base\,Size}$, this can be gradually reduced to perform a sensibility study of the magnitudes of interest (thrust and torque) with the cell size (or likewise, the number of cells).

(a) Thrust versus number of cells in the rotating region   (b) Torque versus number of cells in the rotating region
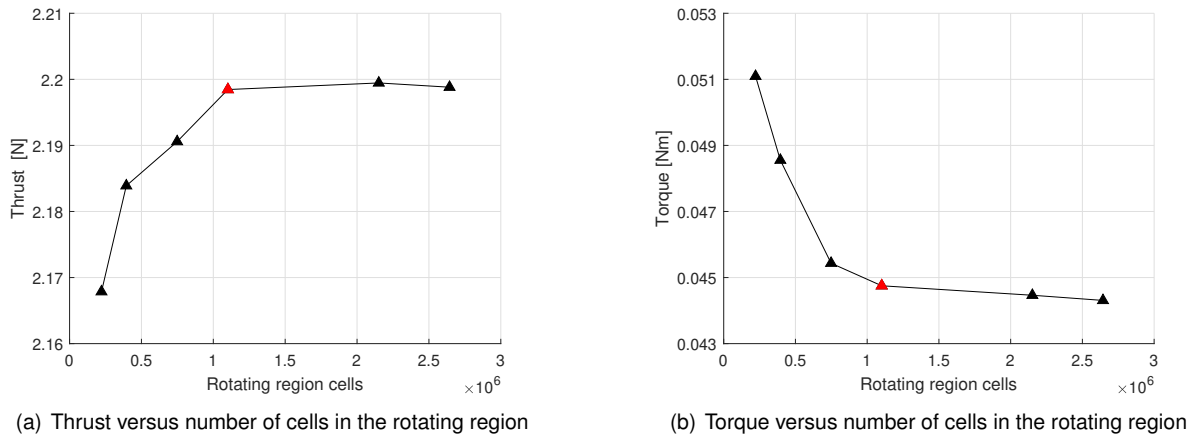
Figure 4.19: Mesh independence study with the element size on APC 10×6E at 4000 RPM

In Figure 4.19 the results of the mesh independence study are displayed, where the cell size change is reflected as the number of cells in the rotating region. It is considered that mesh independence with the cell size is achieved when the percentage variation of the interest magnitudes is less than 1% with respect to the previous iteration (meaning that the cell size for the prior iteration was adequate for the study). As Table 4.3 shows, mesh independence is achieved for 1.10×10^6 cells in the rotating volume (red marker in Figure 4.19).

Table 4.3: Percentage variation for thrust (F_x) and torque (M_x) with respect to their previous iteration for APC 10×6E at 4000 RPM (spatial discretization)

N cells $\times 10^6$	F_x variation	M_x variation
0.22	–	–
0.39	0.73%	5.23%
0.75	0.31%	6.87%
1.10	0.36%	1.53%
2.15	0.05%	0.64%
2.64	0.03%	0.35%

4.6.4 Independence Study with Time Step

The mesh independence study was relative to the spatial discretization. As for the temporal discretization, the time step Δ_t should have been that which satisfied that the Courant number $C <= 1$ for the smallest cell size Δ_x [22]. For rotating meshes there is another restriction regarding the rotation rate: the time step should be small enough so that the rotation of a cell on the interface each time step is equal or smaller than Δ_x (no more than one adjacent cell on the interface is skipped every time step). As this is unattainable for simulations of this kind running on a conventional PC due to computational cost, all the previous simulations have been run with a reasonable time step for propeller CFD simulations according to [25], equivalent of a 5° rotation (which, for 4000 RPM, yields a time step of $\Delta_t = 2.08 \times 10^{-4}$ s). The Δ_t value is reduced to assess its effect on the results:

Table 4.4: Percentage variation for thrust (F_x) and torque (M_x) with respect to their previous iteration for APC 10×6E at 4000 RPM (temporal discretization)

Rotation [°]	$\Delta_t \times 10^{-4}$ [s]	F_x variation	M_x variation
5	2.08	–	–
2.5	1.04	0.14%	0.47%
1	0.42	0.09%	0.31%

As Table 4.4 shows, the reduction in time step does not lead to significant differences in the results (less than 1%), so the original time step is kept (specifically the equivalence for 5° of rotation for other rotation speeds).

4.7 Verification of the CFD Simulations

For the verification of the CFD simulations, nine of them involving the propellers and rotation speeds Ω used in the experimental study have been carried out (for isolated rotors), as Table 4.5 shows:

Table 4.5: Simulations carried out for the validation of the CFD methodology

Propeller	Ω [RPM]
APC 8×6E	2000
	3000
	4000
APC 9×6E	2000
	3000
	4000
APC 10×6E	2000
	3000
	4000

The mesh and simulation related parameters obtained for the mesh independence study on APC 10×6E have been applied on the smaller rotors 9×6E and 8×6E. The results regarding thrust and torque on each propeller for the simulated rotation speeds is compared to the experimental data and to the manufacturer provided data in subsection 3.1.8. As concluded in the validation of the experimental

setup section, the CFD sensibility for thrust and torque is quite good when comparing the obtained values to the experimental results for the isolated rotors tests.

4.8   Methodology for Multiple Rotor Simulations

For the multiple rotor simulations, a STAR-CCM+ base file was created so that the time dedicated to the pre-process phase of the simulations was reduced. The size of the rotating regions, the refinement volume around them and the separation between these elements was automatically set on the CAD editor as functions of the selected propellers for the front and back rotor planes, and the interaxial and interplanar distances d and h. A CAD editor view for a possible configuration is shown in Figure 4.20.
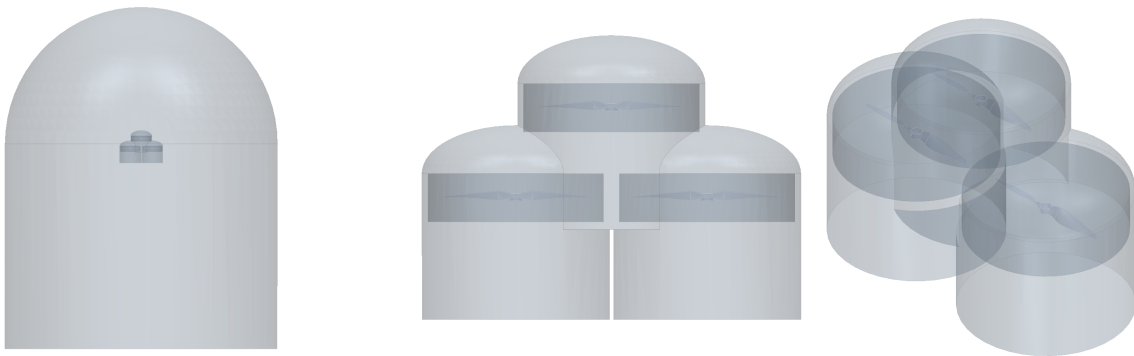
Figure 4.20: Total computational volume (left) along with refinement and rotating volumes (right) in STAR-CCM+ CAD viewer for $d = 160$ mm and $h = 150$ mm with APC 10×6E used in both front and back rotor planes

After selecting the desired propeller combination and the d and h separations, the CAD, parts and regions are automatically updated hierarchically according to these parameters. Then, the mesh operations for the static region and the rotating regions are executed and the meshing process is completed.

The methodology followed is analog to that for single propeller simulations: during the first rotations (from 7 to 15, depending on the h separation) the simulations are run with a coarser mesh and a higher time step than the specified (the set $\mathrm{Base\,Size}$ global parameter is 3.5 times larger than for the final mesh, and the time step used is equivalent of a $10°$ rotation instead of $5°$). This is to set a preliminary flow field solution for when the front rotor wake reaches the back rotor and the transient regime is over around the proximity of the rotors (with a lower computational cost). After that, the regions are remeshed to the appropriate cell size (as in Figure 4.21), and the time step is reduced.
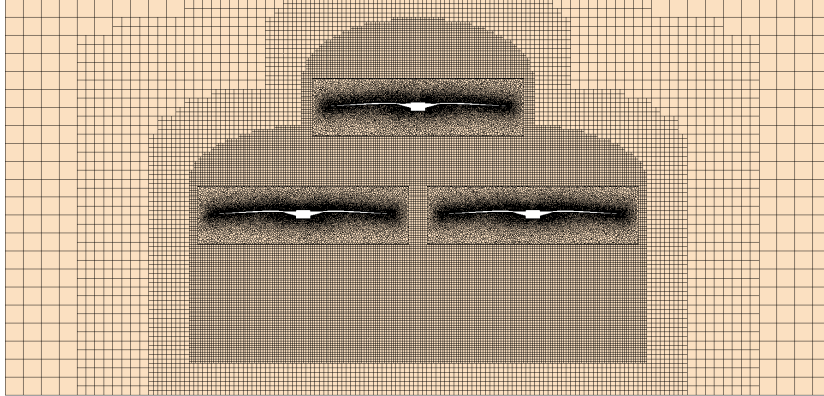
Figure 4.21: Zoom view of a frontal mesh cut for d = 160 mm and h = 150 mm with APC 10×6E used in both front and back rotor planes

The simulations are carried on until the thrust and torque monitors of the propellers stabilize and at least 5 rotations of the slower turning rotor are completed from then on (for a reliable average of thrust and torque).

Chapter 5

Results

In this chapter the results obtained for both experimental and CFD approaches are presented.

The experimental setup was too sensitive to the change of position of the ITs when switching between h and d distances regarding torque measurements. These were less reliable than thrust measurements due to their low magnitude and higher variability, and it was not possible to find any conclusive trend with the distance variation (the mere displacement of the wires had an impact on the already small torque difference measurements, added to the human error introduced when detaching and attaching the ITs from their previous position to the new one).

Regarding CFD simulations, the simulation and mesh parameters that were found suitable for isolated rotors and lead to accurate predictions of thrust and torque as shown in Figures 3.8 and 3.9, still allow for good thrust predictions for the back rotor in tandem configuration. However, the effect of the upstream rotor wake on the downstream rotor torque (mostly composed by drag) did not reflect the expected behavior and instead it decreased when the overlap increased, which is not physical. The mesh independence and simulation parameters studies were carried out for the isolated rotors, meaning that the resolution on the wake could not be enough to reproduce some of its characteristics (vorticity at lower scales) or that the used mesh failed to predict possible flow separations on the propellers due to the action of the wake. Smaller time steps (equivalent to up to $0.5°$ per time step) were used and the nature of the results did not change, so the degree of refinement of the mesh seemed to be the issue. Either way, it would have not been feasible to carry heavier simulations for a large number of cases with the available computational resources, so only the thrust results (pressure forces are easier to predict) are accounted also for the CFD study. Moreover, the simulations with three propellers entailed around a 30% of additional computational cost, so they were carried out with two propellers given that the downstream rotors were little affected by each other, as stated in section 5.2.

5.1 Experimental Results

The experimental analysis is broad. Accounting for all the propeller combinations, all of the d and h distances combinations and all of the front rotor and back rotor speeds combinations, there is a total of 648 measurements. The thrust produced by the back rotor on IT1 for each measurement is displayed in form of thrust loss percentage with respect to the isolated thrust values for the respective propellers and rotation speeds presented in Figure 3.8. The complete results of percentage thrust loss for the back rotor with respect to the isolated propellers are presented in Figures 5.2, 5.3 and 5.4 (featuring propeller combinations with front rotor diameters of 8, 9 and 10 inches respectively). By the direct visual inspection of the graphs, the general trends regarding thrust loss with respect to the isolated propellers on the back rotor can be established:

- The back rotor thrust loss with respect to the isolated rotor values increases very noticeably as the **interaxial separation** d decreases. This is due to the augmentation of the back rotor area under the influence of the upstream rotor wake flow, which carries energy in the downstream direction and is also highly turbulent (perturbing the aligned flow on the downstream rotor blades and even causing its premature separation).

- The back rotor thrust loss with respect to the isolated rotor values slightly increases as the **interplanar separation** h decreases. This is due to the fact that the undisturbed upstream rotor wake shrinks as it develops in the vertical direction, and although the average wake velocity increases as it develops too, the former effect seems to outweigh the latter. A visual representation of this is pictured in Figure 5.1, where the overlap of the back rotor with both the front rotor area and the wake area are displayed (estimated as it was presented in section 2.2.2, although the fully developed wake area is considered to be 0.78 times the front rotor area instead of the theoretical $\frac{1}{\sqrt{2}}$ times the rotor area as found by Leishman [5] experimentally, and the wake is assumed to be fully developed at a vertical distance h of 3 rotor radii).

- As the **front rotor diameter** increases, the thrust loss on the back rotor increases too. The reasoning is the same as for the d separations, since these are fixed and a rotor diameter increase translates into more overlap. There is an additional effect introduced by bigger propellers, as they generate a more turbulent and energetic wake due to the increased tip speed for the same rotation speed Ω. This can clearly be appreciated by checking the thrust loss of the propeller diameter combinations of [8 - 8], [9 - 8] and [10 - 8] inches in Figures 5.2, 5.3 and 5.4 respectively.

- As the **back rotor diameter** increases, the thrust loss on the back rotor increases too. Again, since the d separations are fixed, an increase in rotor diameter results in more overlap, and thus a greater region affected by the upstream wake (as pictured in Figure 5.1 when comparing APC 8×6E with 10×6E as back rotors for the same front rotor). This can be immediately noticed if the thrust losses for propeller diameter combinations of [10 - 8], [10 - 9] and [10 - 10] inches are compared in Figure 5.4. However, this does not mean that bigger propellers perform worse than

59

smaller propellers as back rotors in equal overlap conditions (it has not been tested, since it would require varying d distances according to the diameter combination).

- Increments in the **front rotor rotation speed** Ω_F result in greater thrust losses in the back rotor. This is because the induced velocity on the front rotor is higher for greater Ω_F, so it is the wake velocity and its degree of turbulence (affecting the downstream rotor to a higher extent).

- Increments in the **back rotor rotation speed** Ω_B result in smaller thrust losses in the back rotor. This is, as the back rotor speed Ω_B increases, the back rotor produces more thrust and the percentage thrust loss with respect to the isolated rotor thrust value is lower. In other words, the upstream wake disturbance (empowered by a higher overlap or greater front rotor speed) becomes less relevant as the down stream rotor blades rotate faster.

(a) h = 90 mm and d = 180 mm for all 10×6E rotors

(b) h = 210 mm and d = 180 mm for all 10×6E rotors

(c) h = 90 mm and d = 180 mm for 10×6E and 8×6E rotors

(d) h = 210 mm and d = 180 mm for 10×6E and 8×6 rotors
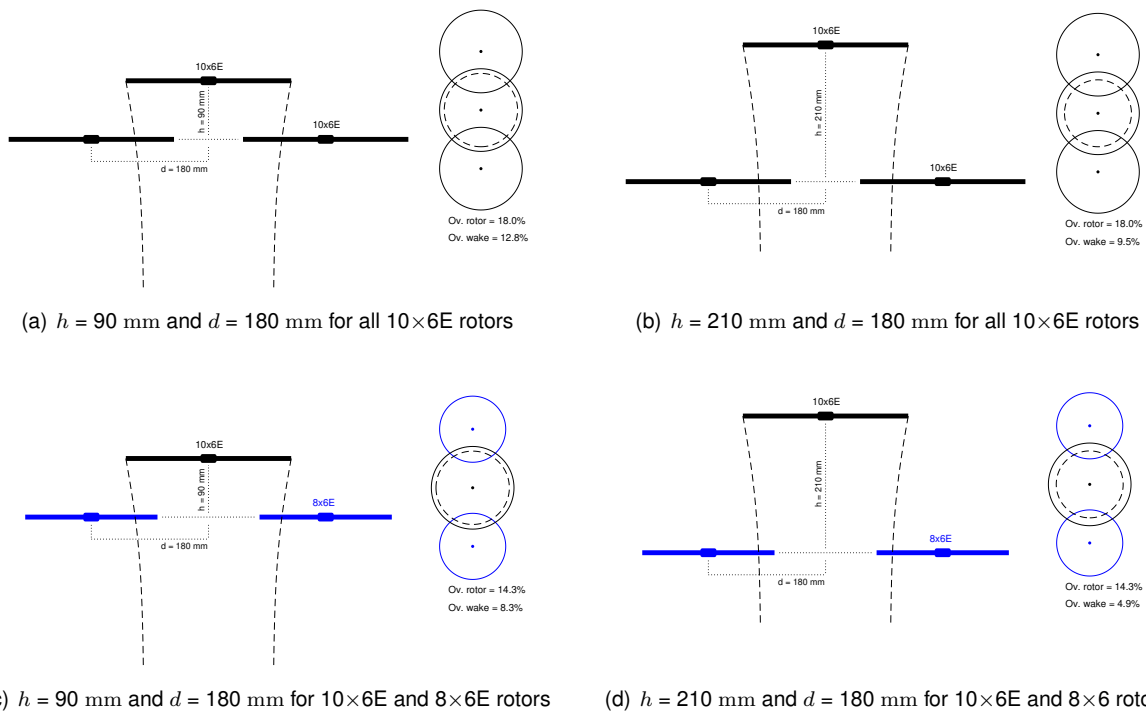
Figure 5.1: Back rotor area overlap with front rotor area and estimated undisturbed wake area (section 2.2.2)

Although these trends can be recognized with the naked eye, it is difficult to attend to all of the data presented in Figures 5.2, 5.3 and 5.4, so the magnitude of the impact that the study parameters have on the back rotor thrust performance for the three tandem rotor configurations is assessed through data averaging in the following subsections.
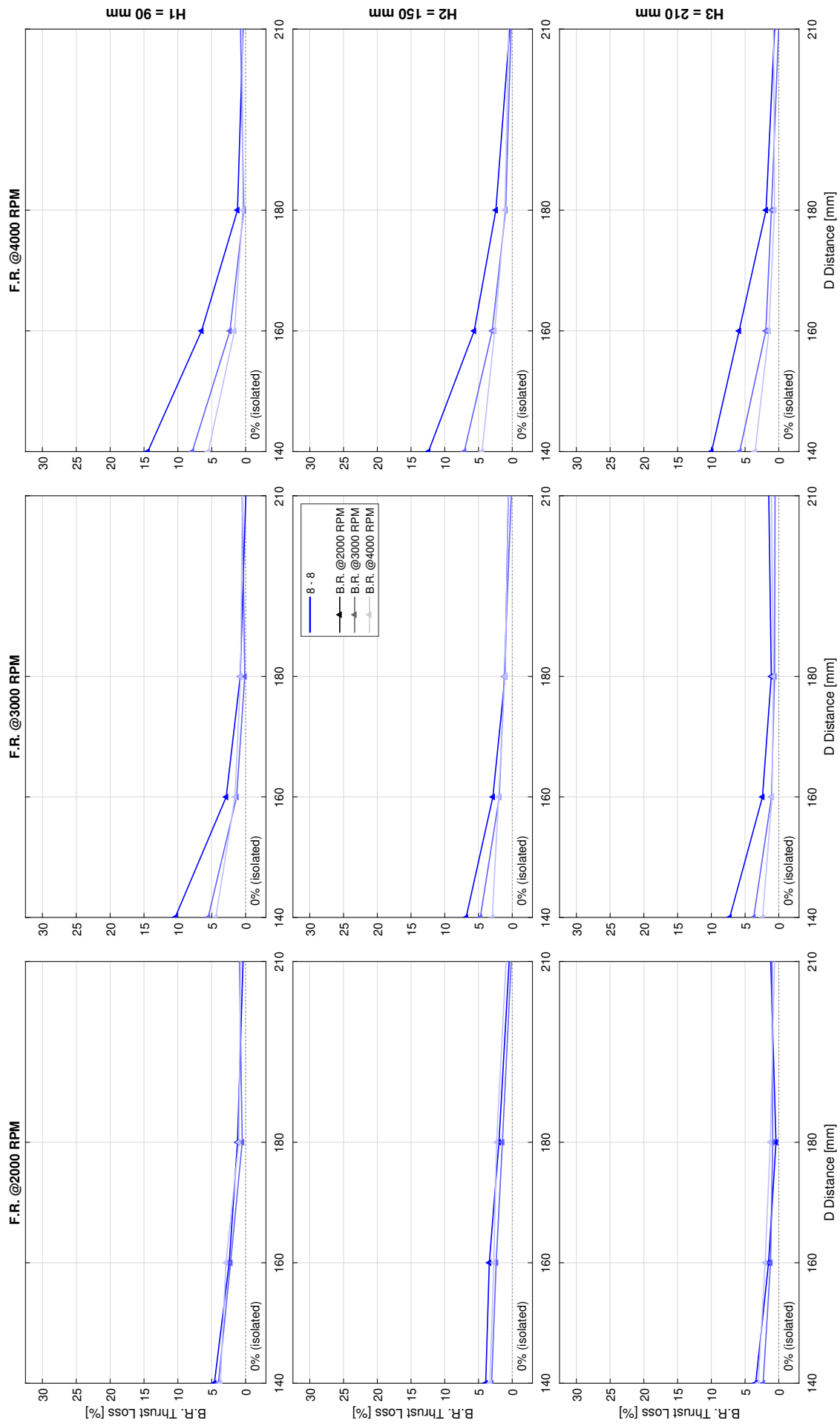
Figure 5.2: Percentage thrust loss for all d, h and rotor speeds combinations for propeller configurations with APC 8×6E as front rotor
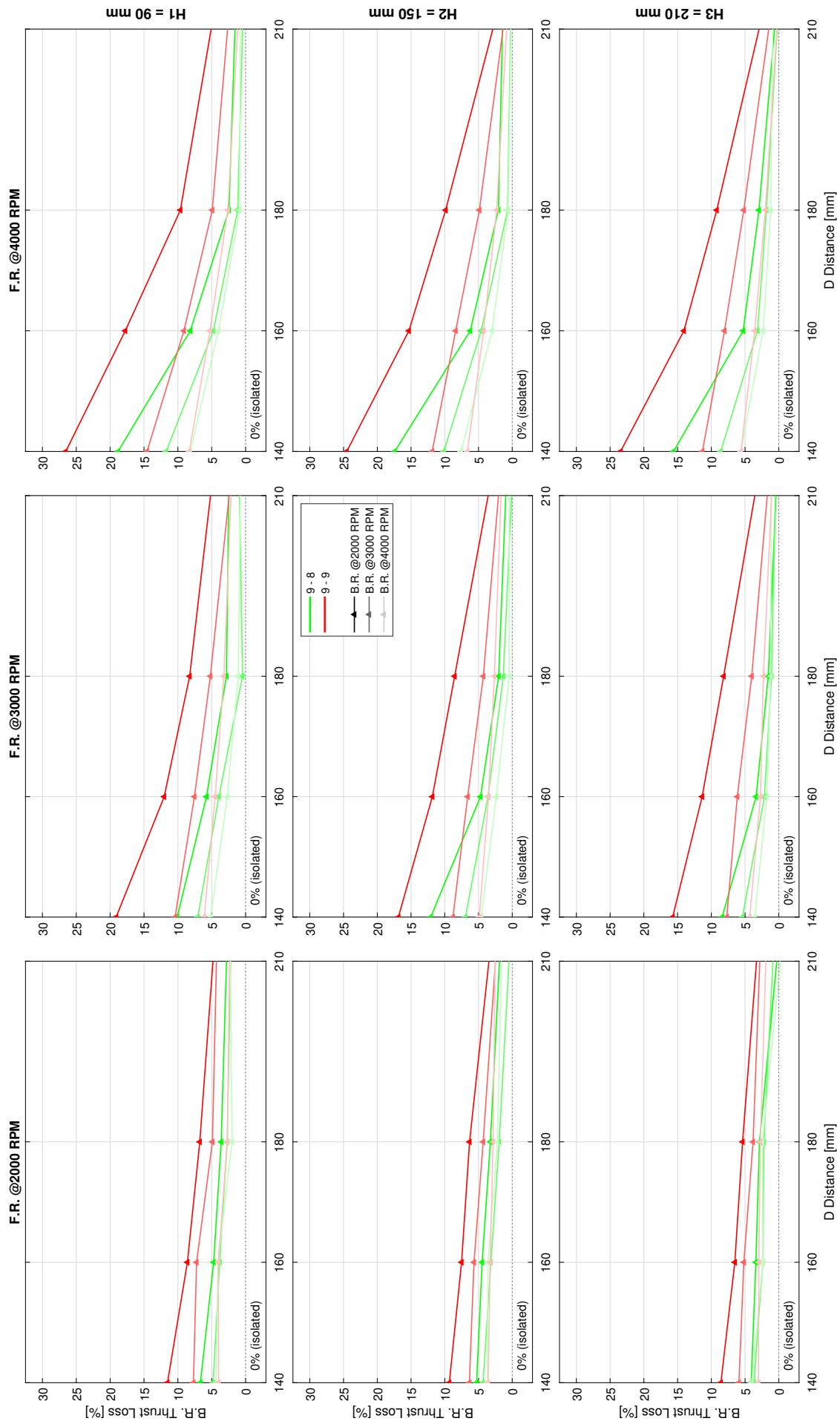
Figure 5.3: Percentage thrust loss for all d, h and rotor speeds combinations for propeller configurations with APC 9×6E as front rotor
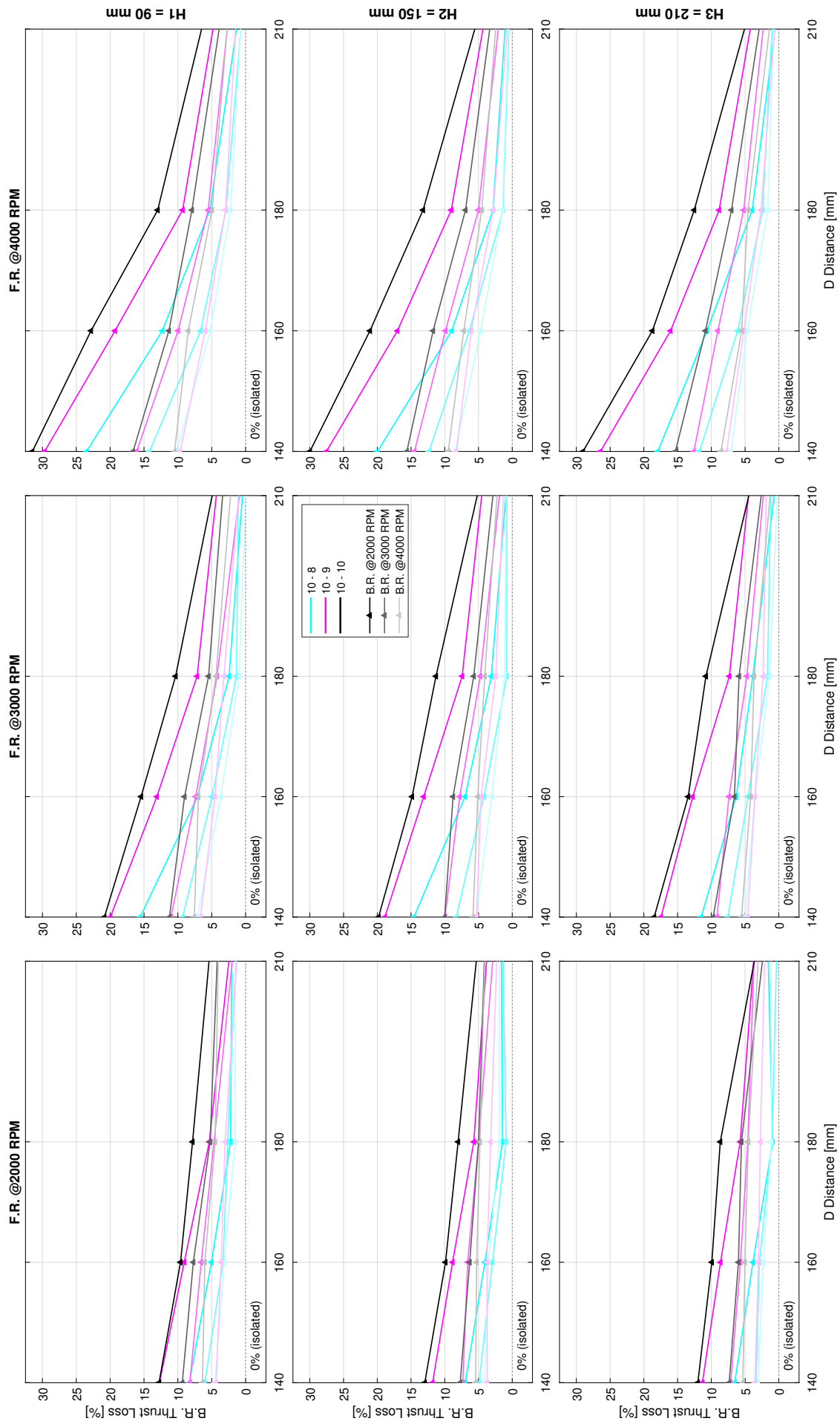
Figure 5.4: Percentage thrust loss for all d, h and rotor speeds combinations for propeller configurations with APC 10×6E as front rotor

5.1.1 Impact of the Rotor Diameter

The impact of the upstream and downstream rotor diameters on the back rotor thrust is highly linked to the overlap that the downstream rotor area experiences with the upstream rotor area, since the inter-axial separations d are fixed. The percentage of back rotor area overlap with respect to the front rotor area is shown in Table 5.1 for the several propeller combinations and d distances.

Table 5.1: Back rotor percentage area overlap with front rotor area for the several propeller combinations and d separations

| D [in]	Back rotor area overlap with front rotor area [%]			
	$d = 140$ mm	$d = 160$ mm	$d = 180$ mm	$d = 210$ mm
10 - 10	33.56%	25.47%	18.03%	8.43%
10 - 9	33.91%	24.73%	16.43%	6.12%
10 - 8	34.07%	23.59%	14.29%	3.46%
9 - 9	27.22%	18.82%	11.38%	2.75%
9 - 8	26.63%	17.01%	8.94%	0.61%
8 - 8	19.82%	11.38%	4.55%	0%

Although the study did not account for equal percentage area overlap on the back rotor (which would have required different sets of d separations for every propeller diameter combination), the impact of the back rotor area overlap (which is the main underlying cause that makes the rotor diameters and d separations to have an effect on thrust loss) can be assessed with the available data. Figure 5.5 embraces all of the back rotor thrust losses with respect to the isolated rotor measurements (which have already been presented in Figures 5.2, 5.3 and 5.4), with the back rotor percentage area overlap as the abscissa axis. No distinction of the study parameters is made other than the propeller diameter combination (different colors), and the data is plotted in sets of 4 measures (the different d separations that produce distinct overlaps according to the combination of propellers). For every vertical column of markers (a specific overlap due to a given d separation for a given propeller combination) the greatest thrust loss corresponds to the smallest interplanar distance $h = 90$ mm, the highest front rotor speed $\Omega_F = 4000$ RPM and the lowest back rotor speed $\Omega_B = 2000$ RPM, meanwhile the smallest thrust loss corresponds to the greatest interplanar distance $h = 210$ mm, the lowest front rotor speed $\Omega_F = 2000$ RPM and the highest back rotor speed $\Omega_B = 4000$ RPM.
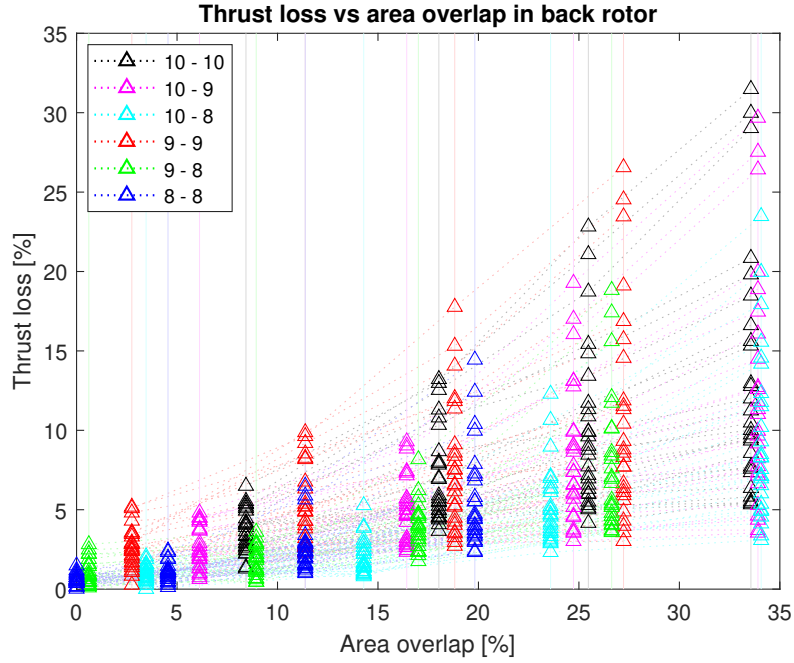
Figure 5.5: Back rotor thrust loss with respect to the isolated rotor versus back rotor percentage area overlap for all of the tests carried out

From the previous graph, some trends can be drawn:

- The thrust loss clearly increases with the rotor area overlap.

- The dispersion between the maximum and minimum thrust loss values is greater as the overlap increases in general, and seems to be the greatest when larger rotors are involved (specially when the back rotors are larger). The increasing dispersion means that the overlap empowers the rest of the other parameter effects (h separations and front and back rotor speeds Ω_F and Ω_B). For that reason, if the correlation between the thrust loss and the overlap area is to be obtained with the whole point cloud in Figure 5.5, the coefficient of determination obtained is R^2 = 0.454 (moderate correlation, meaning that there are other parameters influencing the dependent variable thrust loss). If the coefficient of determination is obtained for every series of d separations (every 4 points joined by dotted lines in Figure 5.5) and these are averaged, the average coefficient of determination is R^2 = 0.937.

- For similar area overlap values, the thrust loss is lower for smaller back rotor diameters (in cumulus of similar overlap values, the propeller combinations with APC 8×6E as back rotors experience less thrust loss on average).

Accounting for that, the average percentage thrust loss for the several propeller combinations is presented in Table 5.2. It can be noticed that the combination with the largest rotors (APC 10×6E both on front rotor plane and back rotor plane) experiences the greatest thrust loss. The effect of the front rotor diameter on the downstream rotor thrust can be evaluated with the [10 - 8], [9 - 8], [8 - 8] and [10 - 9], [9 - 9] diameter combinations. The average percentage thrust loss difference is less than a 1% for

any front rotor diameter increment (although nuances are lost with the complete averaging of the data since differences between propeller diameters are highlighted when other parameters are contemplated, in particular the d distance as it will be shown later on). On the other hand, the effect of the back rotor diameter is evaluated with the [10 - 10], [10 - 9], [10 - 8] and [9 - 9], [9 - 8] diameter combinations. The percentage back rotor thrust loss per back rotor diameter increment is higher than per front rotor increment, so apparently the back rotor diameter has a bigger impact on the back rotor thrust loss.

Table 5.2: Percentage thrust loss for the different propeller configurations averaged for all h, d, back rotor speed and front rotor speed combinations

D [in]	Av. T loss [%]
10 - 10	8.37%
10 - 9	7.01%
10 - 8	4.39%
9 - 9	6.54%
9 - 8	3.42%
8 - 8	2.67%

5.1.2 Impact of the Interaxial Distance

The interaxial distance d has a much bigger impact on the back rotor thrust than the interplanar distance h. To visualize this, a specific configuration for APC 9×6E as front and back rotors with all of them rotating at 4000 RPM is presented in Figure 5.8. It can be noticed that the increments in d distance produce much larger thrust variations than h increments. The effect of the interplanar distance h is more important for low d separations and loses relevance as d increases, since a greater back rotor area overlap with the upstream rotor empowers the effects of the rest of the parameters (such as the h separation) as stated in subsection 5.1.1.

(a) Downstream rotor thrust

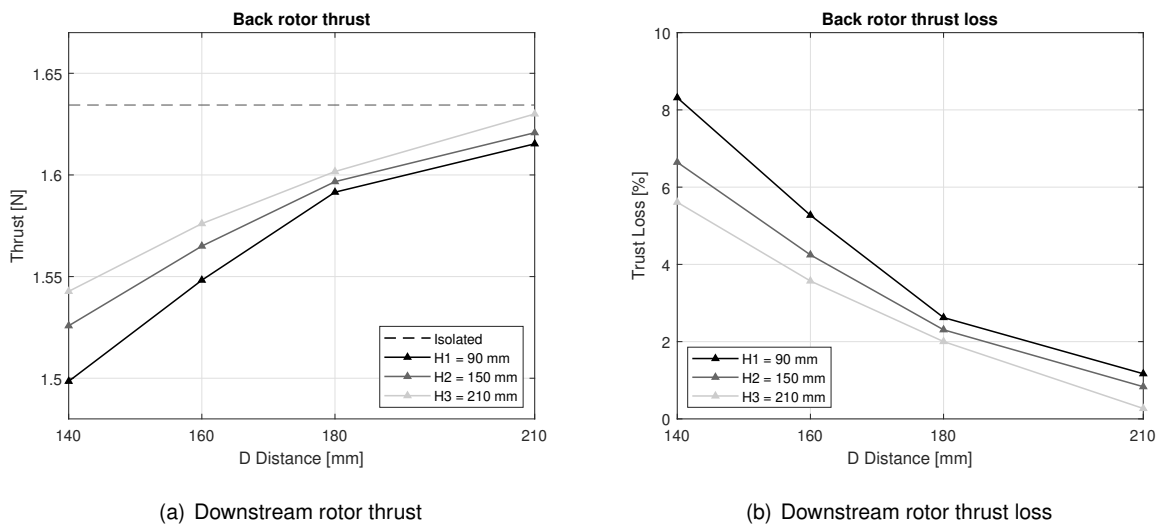(b) Downstream rotor thrust loss

Figure 5.6: Back rotor thrust and percentage thrust loss for APC 9×6E on both rotor planes at 4000 RPM for the several d and h separations

In order to assess the impact of the interaxial distance for the entirety of the experimental study,

for each propeller combination the percentage thrust loss is averaged for the rest of the parameters (back and front rotor speeds and h separation) except for the interaxial separation. This information is presented in Table 5.3.

Table 5.3: Back rotor percentage thrust loss for several propeller configurations and d separations, averaged for all h, back rotor speed and front rotor speed combinations

D [in]	Average back rotor T loss [%]			
	$d = 140$ mm	$d = 160$ mm	$d = 180$ mm	$d = 210$ mm
10 - 10	13.02%	9.87%	6.94%	3.65%
10 - 9	12.06%	8.52%	5.11%	2.84%
10 - 8	9.56%	5.17%	2.64%	1.54%
9 - 9	10.6%	7.51%	4.97%	2.44%
9 - 8	7.47%	3.59%	2.11%	1.26%
8 - 8	5.53%	2.59%	1.11%	0.97%

The all APC 10×6E configuration holds the largest averaged thrust loss gap between the smallest and largest d distance, a difference of 9.37% (much larger than for h separation as shown in subsection 5.1.3). The back rotor thrust is very sensitive to the interaxial distance.

5.1.3 Impact of Interplanar Distance

As mentioned before, the back rotor thrust sensitivity to h separation is low. It is quantitatively evaluated by averaging the results for all of the propeller configurations but distinguishing h separations, in Table 5.4. The gap in average percentage thrust loss between the smallest and largest h separation is under 1.5% for any propeller combination.

Table 5.4: Back rotor percentage thrust loss for several propeller configurations and h separations, averaged for all d, back rotor speed and front rotor speed combinations

D [in]	Average back rotor T loss [%]		
	$h = 90$ mm	$h = 150$ mm	$h = 210$ mm
10 - 10	8.83%	8.49%	7.78%
10 - 9	7.18%	7.08%	6.73%
10 - 8	4.88%	4.19%	4.09%
9 - 9	7.24%	6.23%	6.15%
9 - 8	4.03%	3.36%	2.88%
8 - 8	2.69%	2.53%	2.26%

5.1.4 Impact of the Downstream Rotor Angular Speed

The impact of the downstream rotors rotation velocity is evaluated similarly to those of d and h separations. The measurement results are averaged separately for the propeller combinations, although distinguishing for the parameter to be assessed (back rotor speeds) and also for d distances (since its high impact is acknowledged, thus only averaging for h distances and front rotor speeds). The results are shown in Table 5.5.

Table 5.5: Back rotor percentage thrust loss for several propeller configurations and d separations and back rotor speeds, averaged for all h and front rotor speed combinations

D [in]	B.R. Ω [RPM]	Average back rotor T loss [%]				
		$d = 140$ mm	$d = 160$ mm	$d = 180$ mm	$d = 210$ mm	d AVERAGE
10 - 10	2000	20.82%	15.18%	10.42%	5.02%	12.86%
	3000	11.30%	8.56%	5.95%	3.31%	7.28%
	4000	6.94%	5.87%	4.44%	2.61%	4.97%
10 - 9	2000	19.53%	13.28%	7.22 %	4.22 %	10.99%
	3000	10.67%	7.81%	4.85%	2.54%	6.37%
	4000	5.99%	4.47%	2.82%	1.25%	3.63%
10 - 8	2000	13.87%	6.93 %	2.61%	1.32%	6.15%
	3000	8.64%	4.70%	1.52%	1.12%	3.94%
	4000	6.17%	3.89%	1.46%	1.03%	3.12%
9 - 9	2000	17.30%	11.71%	8.01%	3.99%	10.26%
	3000	9.33%	7.11%	4.55%	2.47%	6.00%
	4000	5.16%	3.70%	2.68%	1.74%	3.32%
9 - 8	2000	10.65%	4.40%	2.24%	1.29%	4.67%
	3000	6.70%	3.38%	1.36%	1.10%	2.97%
	4000	5.07%	3.01%	1.21%	0.96%	2.53%
8 - 8	2000	7.98%	4.01%	1.34%	1.16%	3.96%
	3000	4.91%	1.99%	1.21%	1.04%	2.23%
	4000	3.71%	1.78%	1.03%	0.83%	2.04%

It can be noticed how the d distance effect is blurred to some extend by the total average for each back rotor speed in the last column (for the all APC 10×6E propeller combination with a back rotor speed of 2000 RPM, the highest and lowest thrust averaged loss is 20.82% and 5.02%, with an average of 12.86%). Still it is a good indicator of the degree of sensitivity. The greatest thrust losses occur for lower back rotor speeds (specially when the speed of the front rotor is higher, as can be seen in Figures 5.2, 5.3 and 5.4) since the downstream rotor can experience a greater disturbance due to the upcoming wake with respect to its baseline state (as explained in section 5.1). The back rotor speed should be kept as high as possible in comparison to the front rotor speed, since its impact on the thrust loss is important. The most critical case studied regarding this matter is the all APC 10×6E propeller configuration at h = 90 mm and d = 140 mm, for a front rotor speed of 4000 RPM. As shown in Figure 5.4, the back rotor thrust losses are 31.9% and 16.3% for back rotor speeds of 2000 and 4000 RPM respectively.

5.1.5   Impact of the Upstream Rotor Angular Speed

The upstream or front rotor speed also has a big impact on the back rotor thrust. As indicated in Table 5.6, the downstream rotor thrust is reduced as the front rotor rotation speed increases, due to the higher disturbance introduced by its wake. Attending to the totally averaged thrust losses for the front rotor speeds (right column), the impact of the upstream rotor speed is similar to that of the back rotor speed (since in reality both depend on the relative speed difference between them). The most critical thrust loss with the front rotor speed can be found again for the all APC 10×6E propeller configuration

at h = 90 mm and d = 140, for back rotors speed of 2000 RPM. As exhibited in Figure 5.4, the thrust losses are 31.9% and 12.8% for front rotor speeds of 4000 and 2000 RPM respectively.

Table 5.6: Back rotor percentage thrust loss for several propeller configurations and d separations and front rotor speeds, averaged for all h and back rotor speed combinations

D [in]	F.R. Ω [RPM]	d = 140 mm	d = 160 mm	d = 180 mm	d = 210 mm	d AVERAGE
				Average back rotor T loss [%]		
	2000	8.54%	7.16%	5.68%	3.24%	6.35%
10 - 10	3000	12.00%	9.37%	6.85%	3.66%	7.87%
	4000	18.51%	13.08%	8.29%	4.03%	10.89%
	2000	7.80%	6.38%	4.40%	2.70%	5.32%
10 - 9	3000	11.45%	8.24%	4.84%	3.01%	6.76%
	4000	16.94%	10.94%	5.66%	3.28%	8.91%
	2000	5.37%	3.29%	1.63%	1.28%	2.89%
10 - 8	3000	9.36%	4.93%	1.78%	0.83%	4.23%
	4000	13.94%	7.29%	2.07%	0.86%	6.04%
	2000	6.59%	5.47%	4.48%	2.61%	4.89%
9 - 9	3000	10.44%	7.52%	5.18%	2.89%	6.59%
	4000	14.76%	9.53%	5.67%	3.11%	8.14%
	2000	4.25%	3.08%	1.18%	0.71%	2.72%
9 - 8	3000	7.04%	3.27%	1.42%	0.86%	3.09%
	4000	11.14%	4.43%	2.09%	1.59%	4.89%
	2000	3.33%	2.03%	0.99%	0.57%	1.82%
8 - 8	3000	5.36%	2.31%	1.11%	0.78%	2.18%
	4000	7.90%	3.44%	1.31%	1.21%	3.45%

5.2   CFD Results and Comparison with Experimental Data

With the CFD study, it is intended to assess the accuracy of the computational approach when applied on the tandem rotors interaction problem. In this section, the results obtained with CFD will be presented and compared with the experimental data.

As stated before, the simulations were carried out with two rotors since the computational load was too high for the time limitations of the study. The cases studied with CFD are the following (using APC 9×6E as baseline propeller since the mesh had about a 12% less cells than 10×6E):

- Sensitivity study of h and d distances using two APC 9×6E, both at 4000 RPM.

- Back rotor rotation speed study using two APC 9×6E, the front rotor with a fixed speed of 4000 RPM and for fixed separations h = 90 mm and d = 140 mm.

- Back rotor rotation speed study using an APC 10×6E as front rotor and a 9×6E as back rotor, the front rotor with a fixed speed of 4000 RPM and for fixed separations h = 90 mm and d = 140 mm.

In order to directly compare the obtained CFD results with experimental results, the effect of the missing back rotor should be assessed. The same case is simulated for one back rotor and for two back rotors: all rotors being 9×6E with a 4000 RPM speed, for h = 90 and mm and d = 140 mm (which is presumably the configuration leading to the highest rotor interaction).

Table 5.7: Comparison between front rotor and back rotor thrusts for the cases of two rotors on the back rotor plane (left and right) and a single one (left), for h = 90 and mm and d = 140 mm and 4000 RPM with APC 9×6E

|	B.R. (L) Thrust [N]	B.R. (R) Thrust [N]	F.R. Thrust [N]
2 back rotors	1.529	1.529	1.603
1 back rotor	1.537	–	1.629
% Difference	0.51%	–	1.62%

The thrust developed by the twin back rotors was the same (since as all rotors have the same direction of rotation, the rotation direction of the upper wake on the downstream rotors is opposite to their owns for both of them). As Table 5.7 shows, the thrusts developed by the twin downstream rotors in comparison to the single downstream rotor are very similar (only a 0.51%, the minimum separation is enough so that they do not interfere much with each other in hover), although the upstream rotor experiences a noticeable reduction in thrust of 1.62% (since the thrust of the upstream rotor is reduced by the decrease in the pressure difference on the propeller, which has a greater effect for two downstream rotors as the low pressure region under the upstream rotor increases). The experimental results with 2 back rotors can be compared to CFD results with a single back rotor attending to this difference in the most critical configuration.

5.2.1   Interaxial and Interplanar Separations Sensitivity Study

A sensibility study of h and d separations using two APC 9×6E, both at 4000 RPM is carried out. The CFD simulations show that the effective overlap with the upstream wake is greater than for the undisturbed upstream wake. The wake suction increased mainly with the reduction of the interaxial separation d, as shown in Figure 5.7.

The thrust for the front and back rotors, as well as the percentage thrust loss with respect to the isolated thrust value for the several h and d distances is presented in Figure 5.8.

As for the front rotor, the the thrust loss is lower than for the back rotor since there is no perturbation upstream. The velocity induced by the downstream rotor (with the associated pressure decrease under the front rotor) is a cause for the upstream rotor to reduce. The closest interplanar separation h = 90 mm is the one that affects the most and where the interaxial separation d has more impact, coming to lose up to 1.32% of thrust with respect to the isolated value. As the front rotor thrust loss varies mainly with the interplanar distance, the average thrust losses for each h is presented in Table 5.8.
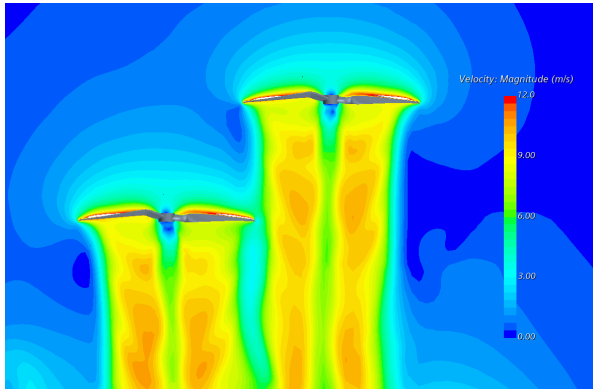
(a) $h = 150\,\mathrm{mm}$ and $d = 210\,\mathrm{mm}$
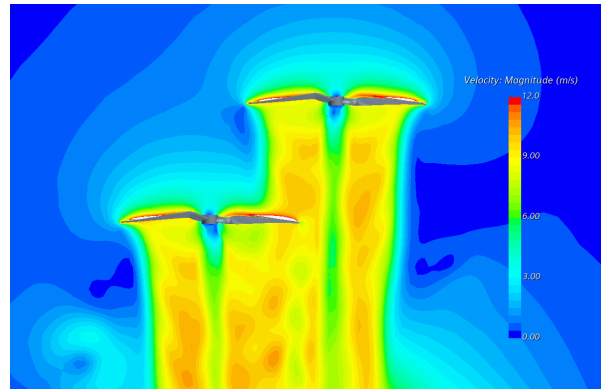
(b) $h = 150\mathrm{mm}$ and $d = 160\,\mathrm{mm}$

Figure 5.7: Wake interaction plot of the absolute velocity field for APC 9×6E on both rotor planes at 4000 RPM for different interaxial distances
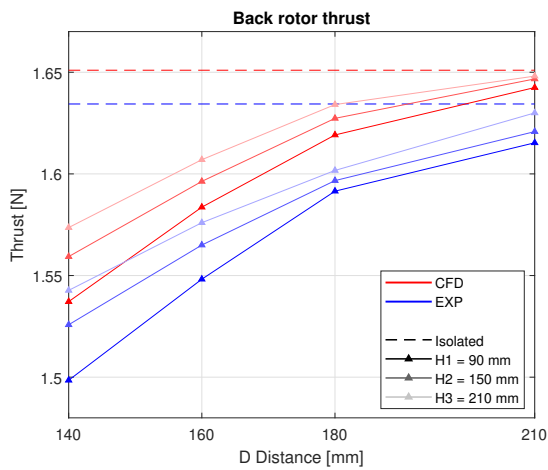
(a) Downstream rotor thrust
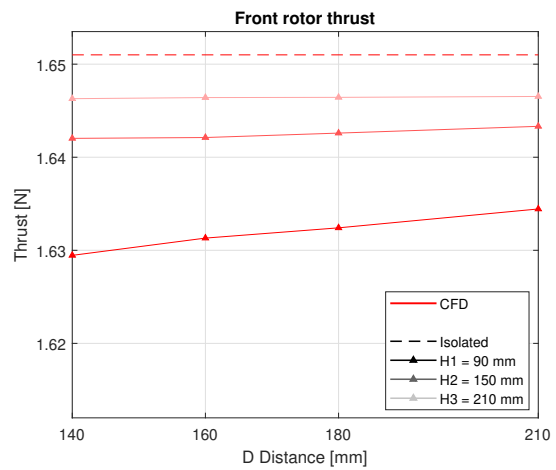
(b) Upstream rotor thrust
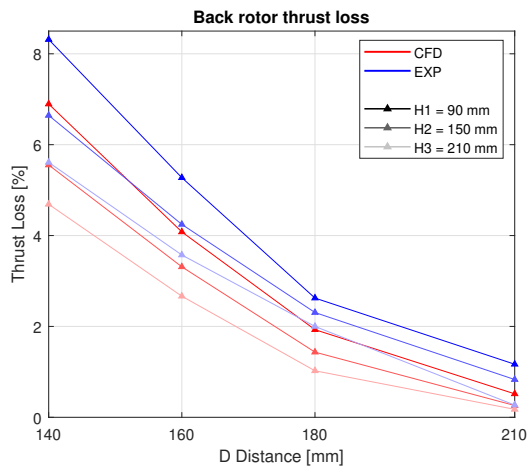
(c) Downstream rotor thrust loss
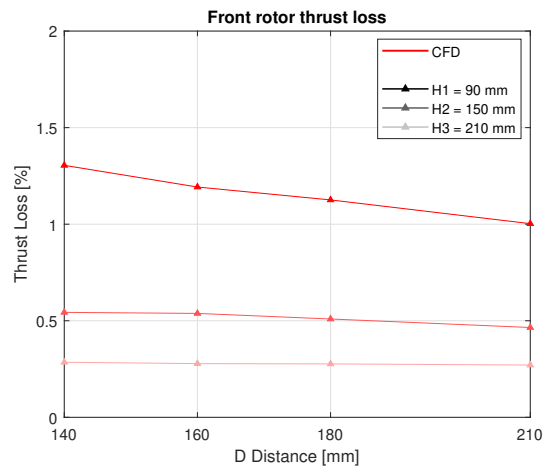
(d) Upstream rotor thrust loss

Figure 5.8: Back and front rotor thrust and percentage thrust loss obtained experimentally and through CFD simulations, for APC 9×6E on both rotor planes at 4000 RPM for the several d and h separations

Table 5.8: Thrust losses averaged for the several d separations for each h separation on the front rotor

	$h = 90$ mm	$h = 150$ mm	$h = 210$ mm
Av. Thrust loss [%]	1.19%	0.51%	0.29%

5.2.2 Downstream Rotor Rotation Speed Sensitivity Study

A sensibility study of the back rotor speed is carried out with CFD, for a fixed front rotor speed of 4000 RPM and fixed position $h = 90$ mm and $d = 140$ mm. The back rotor is always the baseline propeller APC 9×6E, and the study is carried out twice for front rotors APC 9×6E and 10×6E to assess the impact of a bigger upstream propeller in CFD. The results are displayed in Figure 5.9.The CFD values follow the experimental trend: higher thrust loss for lower back rotor speeds with a fixed front rotor speed. CFD thrust values are still above the experimental, with an average difference in thrust loss of 1.32% and 1.58% respectively for the [9×6E - 9×6E] and [10×6E - 9×6E] rotor combinations respectively.

(a) Downstream rotor thrust for double 9×6E

(b) Downstream rotor thrust for 10×6E and 9×6E

(c) Downstream rotor thrust loss for double 9×6E

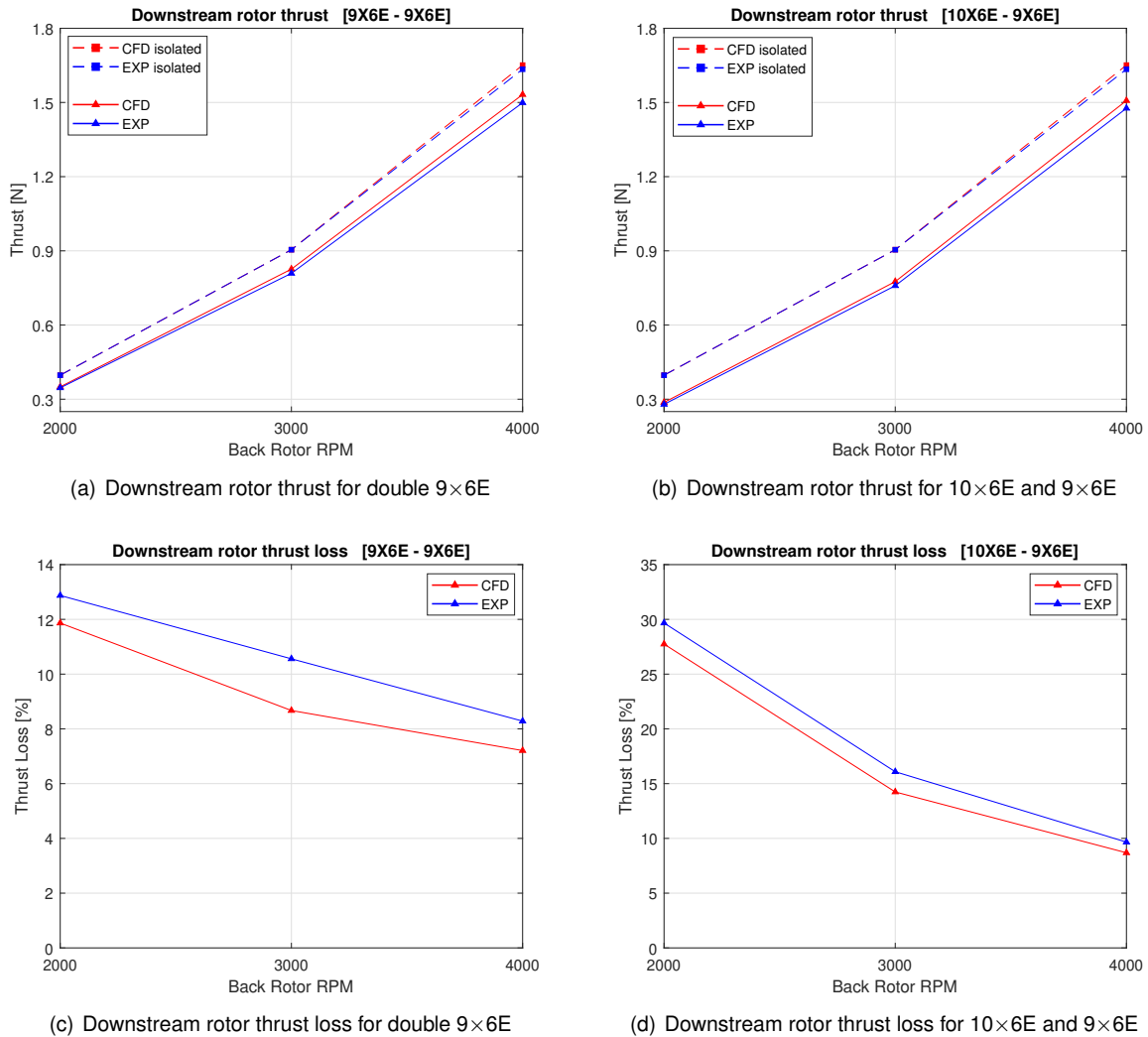(d) Downstream rotor thrust loss for 10×6E and 9×6E

Figure 5.9: Back rotor thrust and percentage thrust loss obtained experimentally and through CFD simulations, for fixed separations $d = 140$ mm and $h = 90$ mm and fixed front rotor speed of 4000 RPM, for several back rotor speeds and front rotor diameters (APC 9×6E on the left and 10×6E on the right)

5.3 Results Summary

Experimental Results

In regard of the study parameters considered in the study, their effects on the back rotor thrust loss with respect to the isolated rotors are:

- The back rotor thrust is reduced as the **interplanar distance** h decreases, and it has a low impact on thrust loss for the studied distances. The thrust loss is maximized for the smaller d distances specially (140 and 160 mm).

- The back rotor thrust is reduced as the **interaxial distance** d decreases, and it has a great impact on the thrust loss (since along with the rotor diameters, it determines the percentage of area overlap on the back rotor).

- The **front and back rotor diameters**, along with the d separation, determine the percentage overlap area of the back rotor affected by the upstream rotor wake. The greatest thrust losses were found where the largest propellers APC 10×6E were involved both in the front and back rotor planes. Another contribution to this is the fact that bigger propellers produce a more disturbing wake than smaller propellers for the same rotation speed due to the increased tip speed. However, it does not mean that configurations with smaller rotors are more efficient since the induced power of the propellers could not be evaluated satisfactorily.

- As the **front rotor rotation speed** Ω_F increases, a greater thrust loss on the downstream rotor is observed due to the augmented disturbance introduced by the upstream rotor wake. It has a great effect on thrust loss, comparable to those of d or Ω_B, specially noticeable for the highest Ω_F = 4000 RPM along with the lowest Ω_B = 2000 RPM.

- As the **back rotor rotation speed** Ω_B increases and more thrust is produced, the thrust loss on the back rotor is reduced as the baseline flow regime is more difficult to disturb. The propellers on the downstream rotor plane should rotate at a higher velocity than those on the upstream rotor plane if possible, since the impact on thrust loss is high, comparable to those of d or Ω_F.

- In general, the thrust loss due to the effects of the h separation, Ω_F and Ω_B increments proved to increase with the back rotor percentage area overlap, resulting in a greater dispersion of the thrust loss for a given area overlap as it is maximized. Smaller back rotor diameters (specially APC 8×6E) experienced less thrust loss dispersion between the maximum and minimum thrust loss for a given area overlap.

- The largest thrust loss was found to be 31.9% for the all rotors APC 10×6E propeller combination, for the front rotor rotating at 4000 RPM and the back rotors at 2000 RPM, for h = 90 mm and d = 140 mm.

CFD Results and Comparison with Experimental Results

Regarding CFD simulations, it is concluded that the thrust loss due to rotor interaction can be predicted with certain reliability with the temporal and spatial resolution allowed by the computational resources, with a maximum 1.19% averaged difference in the back rotor thrust loss for the $h = 90 \mathrm{\ mm}$ distance with respect to experimental data along the interaxial and interplanar distance variation study (carried out at $4000 \mathrm{\ RPM}$ for both rotor planes), and an averaged 1.58% thrust loss difference with respect to experimental data along the back rotor speed variation study. Also, for the interaxial and interplanar separations study, the maximum front rotor thrust loss was found to be 1.3% for $h = 90 \mathrm{\ mm}$ and $d = 140 \mathrm{\ mm}$, although the CFD simulations where carried out with only one back rotor plane since their interaction with each other proved to be negligible for the studied cases and the computational cost was reduced drastically (however, with two back rotors the front rotor would experience a slightly greater thrust loss).

Chapter 6

Conclusions

6.1 Achievements

Fulfilling the objectives raised at the beginning of the study (section 1.3), the present study provides a quantitative insight of some of the parameters that affect the performance of tandem rotor configurations with small sized propellers, as those which would be implemented on UAVs with two rotor planes.

In the present work, the effect on the tandem configuration performance of the front and back rotor planes rotor diameters, the interaxial d and interplanar h distances between rotors and their rotation velocities Ω was assessed quantitatively by means of both experimental and computational approaches, mainly concerning the back rotor thrust loss.

The tandem rotor configuration problem was approached theoretically, through an adaptation by Leishman [5] of the momentum theory model to predict the k_{ov} for tandem rotors with same diameter. A modification of this model was carried out to evaluate the effect of the interplanar distance in addition to the only originally regarded separation, the interaxial distance.

To perform the necessary tests, the experimental test bench designed by Amado [3] to study coaxial configurations (which had already been improved by Santos [4] to allow for tandem configurations as well) was modified to implement a third rotor able to match the rotation speed of the others. The experimental setup allows for good thrust and torque measurements with rotation speed variations for the studied propellers, although when the position of the ITs is changed to study the effect of the interaxial and interplanar distances, the use of the equipment along with the manual manipulation of the test bench does not provide a satisfactory evaluation of the small torque differences regarding the rotor interaction study. However, for the isolated propellers study with different diameters and rotations speeds, both thrust and torque results are satisfactory.

In the computational field, a Matlab code was developed to process and transform the geometric information that APC provides in data sheet format about their propellers. The resulting 3D coordinates of the several airfoils can be exported to CAD softwares to produce very accurate models of the real propellers (as proved by the comparison of isolated rotor thrust and torque values between the experimental and CFD data). With the resulting CADs imported in CFD software, the simulation parameters which yield results comparable to experimental data for isolated rotors, while making them feasible to run properly with the available computational resources were found and applied to simulations with multiple rotors, obtaining good results concerning the thrust loss prediction although to asses the torque increase due to the rotor interaction, higher computational cost is presumably required. It is remarked that both torque and thrust were predicted with accuracy for isolated propeller simulations.

As for the obtained results, the impact on the back rotor thrust loss of the interaxial distance d is highlighted. The greatest thrust losses were found for the smallest d separations, where a more substantial portion of the back rotor area is affected by the upstream rotor wake. As the d distances are fixed, the rotor diameter combination also plays a determinant role in the back rotor area overlap, and consequently in its thrust performance. Rotor combinations with the largest diameters (particularly APC 10×6E in both front and back rotor planes) showed the greatest back rotor thrust losses, meanwhile the smallest thrust losses were found for the reduced dimensions propellers (APC 8×6E). The effect of the front and back rotor speeds Ω_F and Ω_B is also very relevant. The thrust loss on the back rotor increases with increasing Ω_F due to the augmented disturbance of the upstream rotor wake, meanwhile it decreases as Ω_B is enlarged since more thrust is produced and the flow on the back rotor is more resilient to disturbance due to the increased velocity. To finish, the effect of the interplanar distance h was found to have the lowest impact among the studied parameters, making the thrust loss on the back rotor slightly decrease as the h separation between rotor planes is increased, since the wake area of the upstream rotor shrinks as it develops in the streamwise direction.

6.2 Future Work

Although this work represents an advance in the study of rotor interactions in two rotor planes tandem configurations, there is a lot that remains unstudied. The experimental setup was not accurate enough regarding torque measurements when it came to consistently evaluate the differences for several interplanar and interaxial distance increments. Since the torque measures were very sensitive to the change in position of the instrumented tubes (either due to a subtle rearrangement of the wires or to the continuous attachment and detachment of the ITs to the rails), the setup could be either improved or new and less invasive methods to switch between study cases could be found to enable it for the evaluation of trends in torque with these distances (and consequently deriving relevant mechanical power related parameters like the figure of merit FM or κ_{ov}).

As for the CFD approach, the proper torque evaluation due to the wake interaction seems to be very demanding in computational terms. The availability of a powerful computational cluster would allow to explore on the mesh and simulation requirements to attain wake verisimilitude and better frictional forces estimations. Likewise, with a cluster, the pertinent sensibility studies which would entail numerous and even more expensive simulations could be conducted.

As these problems are answered, the study could be expanded in general lines with the inclusion of other relevant parameters. Configurations with two rotors on top and a single back rotor could be tested, both directions of rotation could be subjected to study, the impact of the propeller pitch, the number of blades on the propellers or any other geometry variation could be assessed (since CADs for other APC propellers can easily be obtained with the developed code), and flight conditions other than hover could be contemplated (for example the axial climb and forward flight conditions by bringing the test bench into the already available wind tunnel).

Bibliography

[1] Mostafa Hassanalian and Abdessattar Abdelkefi. Classifications, applications, and design challenges of drones: A review. *Progress in Aerospace Sciences*, 91, 2017.

[2] He Zhu, Hong Nie, Limao Zhang, Xiao Hui Wei, and M. Zhang. Design and assessment of octocopter drones with improved aerodynamic efficiency and performance. *Aerospace Science and Technology*, 106:106206, 2020.

[3] Inês Silva Amado. Experimental comparison of planar and coaxial rotor configurations in multirotors. 2017. MSc Thesis, Instituto Superior Técnico, Lisboa.

[4] Henrique Antunes Portela Santos. Aerodynamic interactions between tandem configuration rotors. 2021. MSc Thesis, Instituto Superior Técnico, Lisboa.

[5] J. Gordon Leishman. *Principles of helicopter aerodynamics*, volume 12 of *Cambridge aerospace series*. Cambridge University Press, 2nd edition, 2006. ISBN:0521660602.

[6] John M Seddon and Simon Newman. *Basic helicopter aerodynamics*. Wiley, 2013.

[7] National Instruments. Labview webpage, 2022. Available online at: `https://www.ni.com/pt-pt/shop/labview.html`, last accessed on 15.09.2022.

[8] Electric Motor Power. EMP webpage, 2022. Available online at: `https://www.emppl.com.au/`, last accessed on 15.09.2022.

[9] Mathworks. Matlab webpage, 2022. Available online at: `https://es.mathworks.com/products/matlab.html`, last accessed on 15.09.2022.

[10] J. C. for Guides in Metrology. Evaluation of measurement data-guide to the expression of uncertainty in measurement. *JCGM*, 100(2008):1–116, 2008.

[11] APC propellers. APC propellers performance data, 2022. Available online at: `https://www.apcprop.com/technical-information/performance-data/`, last accessed on 15.09.2022.

[12] F. Carroll Dougherty, Terry L. Holst, Kaitlyn Grundy, and Scott D. Thomas. Tair: A transonic airfoil analysis computer code. 1994.

[13] APC propellers. APC propellers webpage, 2022. Available online at: `https://www.apcprop.com/`, last accessed on 15.09.2022.

[14] J.D. Anderson Jr., R. Grundmann, G. Degrez, E. Dick, and J. Degroote J. Vierendeels. *Computational Fluid Dynamics An Introduction*. John F. Wendt, 2009.

[15] Siemens. Simcenter STAR-CCM+ webpage, 2022. Available online at: `https://www.plm.automation.siemens.com/global/en/products/simcenter/STAR-CCM.html`, last accessed on 15.09.2022.

[16] Michael Selig. UIUC Airfoil Coordinates Database, 2022. Available online at: `https://m-selig.ae.illinois.edu/ads/coord_database.html`, last accessed on 15.09.2022.

[17] Dassault Systems. Solidworks webpage, 2022. Available online at: `https://www.solidworks.com/`, last accessed on 15.09.2022.

[18] Autodesk. Fusion 360 webpage, 2022. Available online at: `https://www.autodesk.com/products/fusion-360/`, last accessed on 15.09.2022.

[19] Runa Pinto, Asif Afzal, Loyan D'Souza, Zahid Ansari, and Mohammad Samee. Computational fluid dynamics in turbomachinery: A review of state of the art. *Archives of Computational Methods in Engineering*, 24, 2016.

[20] MixIT. MRF versus Sliding Mesh, 2016. Available online at: `https://mixing-solution.com/2012/07/31/mrf-versus-sliding-mesh/`, last accessed on 15.09.2022.

[21] MR CFD. Moving Reference Frame (MRF), 2020. Available online at: `https://www.mr-cfd.com/services/fluent-modules/moving-reference-frame/`, last accessed on 15.09.2022.

[22] Francesco Balduzzi, Alessandro Bianchini, Giovanni Ferrara, and Lorenzo Ferrari. Dimensionless numbers for the assessment of mesh and timestep requirements in cfd simulations of darrieus wind turbines. *Energy*, 97:246–261, 2016.

[23] Omar Lopez Mejia, Oscar Mejia, Karol Escorcia, Fabian Suarez, and Santiago Lain. Comparison of sliding and overset mesh techniques in the simulation of a vertical axis turbine for hydrokinetic applications. *Processes*, 9, 2021.

[24] Yao Zheng and Meng Liou. Three-dimensional dragon grid methodology for computational fluid dynamics. *Computational Fluid Dynamics Journal*, 10:585–591, 2002.

[25] Dendy Satrio, I Ketut Utama, and Mukhtasor Mukhtasor. The influence of time step setting on the cfd simulation result of vertical axis tidal current turbine. *Journal Of Mechanical Engineering And Sciences*, 12:3399–3409, 2018.

[26] Luca Mangani, Wolfgang Sanz, and Marwan Darwish. Comparing the performance and accuracy of a pressure based and a density-based coupled solver. 2015.

[27] F.R. Menter. *Zonal Two Equation k-w Turbulence Models For Aerodynamic Flows*. AIAA paper, 24th Fluid Dynamics Conference, 1993.

[28] Rickard Bensow, Christer Fureby, Mattias Liefvendahl, and T Persson. A Comparative Study of RANS, DES and LES. 2006.

[29] Nor Azwadi Che Sidik, Siti Nurul Akmal Yusof, Yutaka Asako, S. Mohamed, and Arif Aziz. A Short Review on RANS Turbulence Models. *CFD Letters*, 12:83–96, 2020.

[30] Ideal Simulations. Turbulence Models In CFD, 2020. Available online at: `https://www.idealsimulations.com/resources/turbulence-models-in-cfd/`, last accessed on 15.09.2022.

[31] F.R. Menter. Two-equation eddy-viscosity turbulence models for engineering applications. *AIAA Journal*, 32(8):1598–1605, 1994.

[32] Seokkwan Yoon, Henry C. Lee, and Thomas H. Pulliam. Computational study of flow interactions in coaxial rotors. 2016.

[33] Manoochehr Darvish and Stefan Frank. Toward The CFD Simulation Of Sirocco Fans: From Selecting A Turbulence Model To The Role Of Cell Shapes. 2012.

[34] Marko Perić and A. G. Ferguson. The advantage of polyhedral meshes. 2005.

[35] B. Mohammadi and G. Puigt. Wall functions in computational fluid mechanics. *Computers Fluids*, 35(10), 2006.

[36] National Aeronautics and OH. Lewis Research Center. Space Administration, Cleveland. *Exploring in Aeronautics. An Introduction to Aeronautical Sciences*. Distributed by ERIC Clearinghouse, Washington, D.C., 1971.

[37] Fluid Mechanics 101. Fluid Mechanics 101 webpage, 2021. Available online at: `https://www.fluidmechanics101.com/`, last accessed on 15.09.2022.

[38] François Richez, Kurt Kaufmann, Philip Ströer, Caroline Lienard, Normann Krimmelbein, and Anthony Gardner. Assessment of boundary layer transition prediction methods for rotating blades. 2019.

[39] Lars Müller, Dragan Kozulovic, and Jens Friedrichs. Unsteady Flow Simulations of an Over-the-wing Propeller Configuration. 2014.